Exploration of using phase change material for thermal management of Electric Vehicle Battery

Thesis by

Shi Chen

In Partial Fulfilment of the Requirements

for the Degree of

Doctor of Philosophy (PhD)

School of Engineering

Durham University

Date of Submission:

Jan 2023

Abstract

Battery thermal management (BTM) has been considered as one of the most important components in battery management system (BMS), as the thermal performance could heavily influence the safety and the performance of the battery and thus effect on the electric vehicle (EV) or hybrid electric vehicle (HEV). Some widely explored BTM systems includes forced air-cooling, direct/indirect fluid-cooling, and heat pipe (HP) systems. The forced air-cooling suffers from the low heat exchange efficiency between the air and the battery wall, while the direct/indirect fluid-cooling method takes the disadvantage of the extensive overall volume with the requirement of some other accessories such as the pump. Besides, HP systems have the limitation as it needs complex system layouts and thus high system weight.

Phase change material (PCM) BTM system has attracted increasing interest as the latent heat could be normally greater than the sensible heat (cooling) those in traditional cooling systems. Moreover, PCM BTM system could work independely without supportive energy or extra accessories, which enables itselt to be employed flexibly in the EV and HEV. However, PCM cooling method faces the issue of leakage, which limits its application in the EV battery packs. The form-stable PCM (FSPCM) and micro-encapsulated PCM (MPCM) slurry then comes to the solution. The conventional PCM with the potential to leak in the battery pack could be embeded in the supoorting matrix to form the FSPCM, or micro-encapsulated in the shell to form the MPCM. Both methods provides surroundings to hold the phase transition process inside and prohibited liquid-phase PCM from flowing into the outter.

As the research which employed FSPCM or MPCM slurry methodologies in BTM systems was very limited, in this PhD project, FSPCM and MPCM slurry were utilized in BTM systems to evaluate their perofmance in BTM. It was expected to improve the existed BTM technologies, and thus enhance the battery safety and performance for EV, HEV or even further related applications.

The methodologies accessible for BTM used in EV or HEV were reviewed in Chapter. 2. The development histories and the features were introduced towards various measures, with the emphasis on PCM BTM, especially FSPCM and MPCM. The scientific gap was therefore pointed out.

A numerical model of the FSPCM BTM was established in Chapter. 3, using MATLAB. The BTM performance was compared in four scenarios, and the optimal one was demonstrated to be the coupled FSPCM and air-cooling BTM system. With higher EG mass fraction, the increase rate of T_{cor} was observed to be reduced. When the EG mass fraction was 4.6 wt%, T_{cor} at t_C was 317.7 K, 5.2 K lower than 322.9 K (without any EG additives). The thickness of FSPCM should be carefully selected according to the heat generated by the target battery pakage. Comprehensively considering the capital cost of the FSPCM BTM or the size of that system, 0.06 could be the competitive candidate among all.

The experimental investigation of BTM system performance has been conducted in Chapter. 4. Either MPCM slurry or water worked as the coolant to accompanish the BTM system. Their performance were separately discussed towards different working conditions (battery pack charging rates, and C-rates). The optimal working condition for MPCM slurry integrated BTM system was when the charge rate was 2C, as the group using C-rate of 2C spend the longest time of MPCM slurry in the melting range. In thiscondition ΔT_{cor} was 26.87 °C

Modelling work of BTM system has also been done in Chapter. 5 utilizing ANSYS. The experimented BTM system was modelled with the cooling fluid alternatively switched between MPCM slurry and water, while the cooling module basement made by aluminium or FSPCM discussed in Chapter. 3. High MPCM mass ratio has limited effect on BTM system performance using Al-basement, even though it can slightly enhance the battery cooling performance using FSPCM-basement, in the confined simulation conditions. FSPCM-basement was more promising for a lower battery temperature, compared to Al-basement. The heat transfer between the battery and the coolant was enhanced by the application of FSPCM-basement. The T_{cor} reduction by substituting aluminium with FSPCM is 0.94%, 0.25%, and 0.01%, respectively, with C-rate ranging from 10C to 3C.

In a conclusion, the BTM integrated with FSPCM and PCM showed the potential to be a high-performance BTM for battery packages used in EV/HEV.

Acknowledgement

Valuable help was offered to me by many people, during but not only during my thesis writing and PhD study. I would like to give my sincere gratitude to them at this very important moment.

My deepest gratitude firstly goes to my mother and father, who support me to study overseas with consistent encouragement and extraodinary patience. It has been long time since my first leave from homeland, but I always feel loved by my family, and that fufills me with passion and confidence in life and study here.

I am also extremely grateful to my supervisors, Dr. Zhiwei Ma, Dr. Huashan Bao, and Prof. Anthony Paul Roskilly, who greatly helped me with wise suggestions, useful instructions, and personality inspirations. I really learned a lot from them, in respect of professional knowledegement and atitude towards study, work, and life. With their supervision, I now know how to face the challenge in the scientific field, and how to make a plan and manage it in time to solve the problem.

Besides, many other people in the group also deserve my heatfelt gratitude. The techinician in the lab, Mr. Ian Douglass, provided extensive help on my experimental stuffs: establishment of the test rig, device calibration, and practical operation on the test rig. Moreover, my best friend and girlfriend, Ms Chenjue Wang, I could not reach here without the way we passed.

I would like to thank every challenge and every great moment in these years. They complete this valuable experience, by which not only could I consequently accomplish PhD project, but also influenced my whole life by the style how I see and treat the world. The beautiful scenaries in UK and the great people I met here, they all composed a wonderful chapter in my life.

List of publications

[1] Under review: **Shi Chen**, Zhiwei Ma*, Huashan Bao, Anthony Paul Roskilly, Numerical analysis of using Form-stable phase change material for battery passive cooling, *Case Studies in Thermal Engineering*.

List of tables

List of figures

Nomenclatures

Symbols

$\dot{q}_{\mathrm{b}}$	Volumetric heat generated by battery
$\dot{Q}_{\mathrm{b,gen}}$	Heat generated by battery
$\dot{Q}_{\mathrm{conv}}$	Convective heat transfer rate
A	Surface area, m^2
c_p	Specific heat capacity, $\mathrm{J{\cdot}kg^{-1}{\cdot}K^{-1}}$
$c_{\mathrm{p,\,b}}$	Specific heat capacity of the cell
$c_{\mathrm{p,EG}}$	Specific heat capaciy of EG
$c_{\mathrm{p,HDPE}}$	Specific heat capacity of HDPE
$c_{\mathrm{p,MPCM}}$	Specific heat capacity of MPCM particle
$c_{\mathrm{p,MPCMs}}$	Specific heat capacity of MPCM slurry
$c_{\mathrm{p,PCM}}$	Specific heat capacity of PCM
$c_{\mathrm{p,PCM,l}}$	Specific heat capacity of PCM in liquid phase
$c_{\mathrm{p,PCM,s}}$	Specific heat capacity of composite FSPCM
$c_{\mathrm{p,PCM,s}}$	Specific heat capacity of PCM in solid phase
$c_{\mathrm{p,water}}$	Specific heat capacity of water
C_{r}	Rated capacity of the battery
D	Pipe diameter, m
D_{ω}	Cross-diffusion term

f	Fanning flow friction, a calculation indicator of pressure difference
G_k	Production of the turbulence kinetic energy
G_ω	ω generation
H_b	Battery height
I	Current intensity, A
I_C	Current intensity during charging
k	Turbulence kinetic energy
K	Heat transfer coefficient, $\mathrm{W{\cdot}m^{-2}{\cdot}K^{-1}}$
K_air	Convective heat transfer coefficient of the air
l	Characteristic length, m
L	Latent heat, J/kg
L_PCM	Latent heat of PCM
n	Number of battery charge/discharge rate
Nu	Nusselt number
p	Pressurem, kPa
Pr	Prandtl number
q	Volumetric heat generation rate, $\mathrm{W{\cdot}m^{-3}}$
Q	Heat flow quantity, W
R	Resistance (Ω)
r_C	Charging rate (C-rate)

Re	Reynolds number
R_{in}	The internal resistance of the battery
$r_{PCM\text{-}b}$	The thickness ratio between the FSPCM and the battery
S	Strain rate magnitude
$S_{\omega/k}$	User-defined source terms
t	Time, s
T	Temperature, K
T_{amb}	Ambient temperature
t_C	Time in which the battery could be fully charged using r_C.
T_{cor}	Core battery temperature
T_E	Temperatrue at the east of the point
T_{fs}	Temperature at the fluid surface
T_{in}	Inlet coolant temperature
T_l	Temperature of the PCM at stable liquid phase
T_m	Melting temperature
T_{out}	Outlet coolant temperature
T_P	Temperature at the point
T_s	Temperature of the PCM starts to melt
T_{ss}	Temperature at the solid surface
t_{sta}	Time for the temperature file to be stable

T_W	Temperature at the west of the point
u	Air velocity, $m \cdot s^{-1}$
U	Open circuit potential, V
u_∞	Relative air velocity towards the object in the free stream condition
$u_{i/j}$	Velocity components
$u_{i/j}$'	Fluctuation components of velocity
V	Cell potential, V
Vol	Volume, m^3
W_b	Battery weight
x	Distance from the leading edge, m
$x_{i/j}$	Axial coordinates
$Y_{\omega/k}$	Dissipation of ω or k becausde of the turbulence
δ	Thickness, m
δ_b	Thickness of battery
δ_{PCM}	Thickness of PCM
λ	Thermal conductivity, $W \cdot m^{-1} \cdot K^{-1}$
λ_d	Thermal conductivity of the dispersed phase
λ_e	Effective thermal conductivity
λ_{EG}	Thermal conductivity of EG
λ_{EP}	Thermal conductivity in the area confined by T_E and T_P

λ_{HDPE}	Thermal conductivity of HDPE
λ_{WP}	Thermal conductivity in the area confined by T_W and T_P
ω	Mass fraction, %
ω_{EG}	Mass fraction of EG
ω_{HDPE}	Mass fraction of HDPE
ω_k	Dissipation rate of k
ω_{PCM}	Mass fraction of PCM
ω_s	Mass ratio of MPCM particle
ω_{water}	Mass ratio of water
$\Gamma_{\omega/k}$	Effective diffusivity of ω or k
$\alpha*$	A coefficient determined by k, ω, μ, and ρ, when it is in the low-Reynolds number condition; Otherwise, α^* is 1 when it is in the high-Reynolds number condition.
λ_c	Thermal conductivity of the continuous phase
λ_{cell}	Thermal conductivity of the cell
λ_f	Thermal conductivity of the fluid
μ	Dynamic fluid viscosity, $N \cdot s \cdot m^{-2}$
ρ	Density, $kg \cdot m^{-3}$
ρ_{cell}	Density of the cell
ρ_{EG}	Desnity of EG
ρ_{HDPE}	Density of HDPE

$\sigma_{\omega/k}$	Prandtl number for ω or k
ϕ	Volume fraction of the disperse phase

Abbreviations

Al	Aluminium
AF	Aluminium foam
APM	Ammonium polyphosphate (APP), pentaerythritol (PER) and melamine (MA)
APP	Ammonium polyphosphate
BMS	Battery management system
BSL	Baseline
BTM	Battery thermal management
CHI	Chitosan
COP	Coefficient of performance
C-rate	Charging rate
EG	Expanded graphite
EV	Electric vehicle
FCEV	Fuel cell electric vehicle
FM	Fluorescence microscopy
FSPCM	Form stable phase change material

GEL	Gelatine
GHG	Green house gas
HDPE	High-density polyethylene
HDPE-EVA/OMT	polyethylene/poly/organophilic montmorillonite
HEV	Hybrid electric vehicle
HP	Heat pipe
LBG	Locust beam gum
Li-ion	Lithium-ion
MA	Melamine
MC	Methylellulose
MF	Melamine - formaldehyde
MPCM	Micro-encapsulated phase change material
OM	Optical microscopy
PA	Paraffin
PCM	Phase change material
PEC	Pectin
PEMFC	Proton exchange membrane fuel cell
PER	Pentaerythritol
PHP	Pulsating heat pipe
PSC	Porous silica ceramic

PV/T	Photovoltaic thermal
PW	Paraffin wax
SEM	Scanning electron microscopy
SOC	State of charge
SST	Shear-stress Transport
XG	Xanthan gum

Table of contents

Chapter 1. Introduction

1.1 Background

Pure Electric Vehicles (EV), Hybrid Electric Vehicles (HEV) and Fue Cell Electric Vehicles (FCEV) play increasingly significant role at present as they bring the solution towards the coming crisis such as the shortage of the fossil fuel deposit and the global warming issues, compared to conventional vehicles.

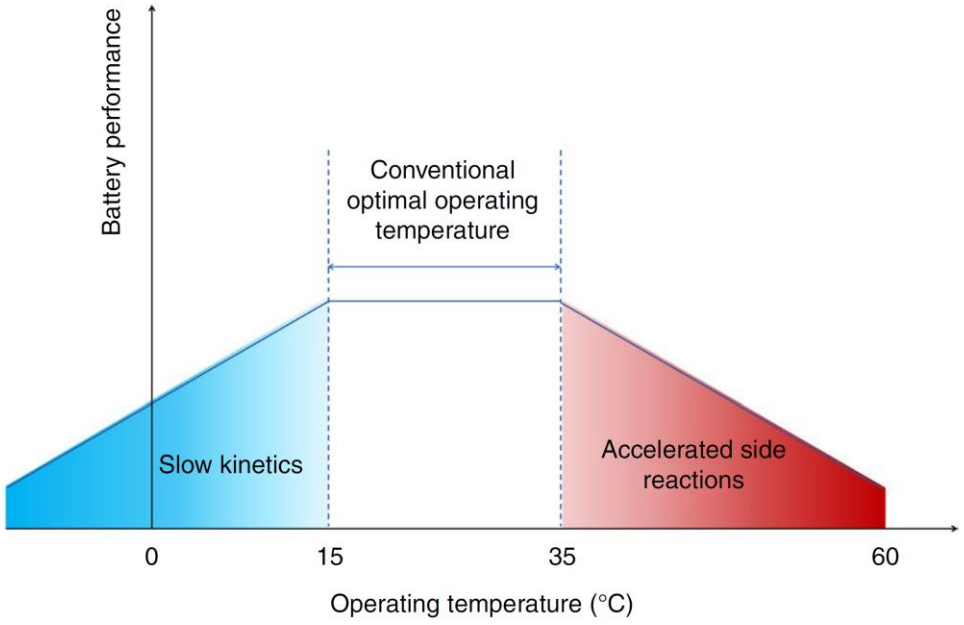

Fig. 1.1 Operational temperature range of Li-ion battery [1].

However, their performance strongly depends on that of the battery pack applied in the technologies. Major concerns are raised from hot, or cold or temperature non-uniformity of battery, which can heavily decrease the vehicle performance, reliability, or life cycle cost. The high working temperature of the battery can result in various problems. Li-ion battery has its optimal performance at the temperature range of 15-35 ℃, as shown in Fig. 1.1 [1]. It is widely accepted that the battery cycling stability will reduce at elevated battery temperature, this is caused by increased reactivitiy of of the electrode materials and consequent side reactions. The Sony 18650 cell was experimently observed to have a fade capacity with the increased working temperatures

[2]. A high battery operation temperature can also result in thermal runaway without effective removement of the accumulated heat [3-5]. As battery temperature decreasing, the reversible battery capacity decrased due to a couple of reasons, like higher electrolyte viscosity, larger polarization and slower interfacial kinetics [1]. Moreover, EV/HEV should work over a wide range of weather condition, which rises the crucialness of their effectiveness as well as the reliability [6].

Improvement of the thermal condition of the batteries can largely enhance the battery performance, mainly by the reduction of the heat generation rate of the battery and increment of the heat dissipation rate (not appropriate at cold weather condition). Therefore, the battery thermal management (BTM) has been regarded as one of the most essential elements for batteries used in EVs, as part of the battery management system (BMS), to sustain the battery operation temperature in the desired temperature range.

Significant research endeavours have been made to seek the suitable technologies for the battery thermal management, and several BTM systems have been investigated for long time, including the forced air-cooling/heating system with a fan, the direct/indirect fuild cooling/heating system with various liquid media (e.g. water, gycol, oil, acetone or even refrigerants), heat pipe (HP) cooling system, and Phase Change Material (PCM) thermal management system. Widely regarded as the most mature and simple thermal management technology, the air cooling/heating mainly benefits from both of simple structure and low cost, but it suffers from low heat exchange efficiency between the battery wall and the air. Besides, this technology is highly sensitive to the environment temperature, and the precision or uniformity of the desired working temperature is hard to be maintained when the operation condition is complex. Liquid BTM system applies liquid fluid with greater heat transfer coefficient than air, however, the overall volume of this system is extensive, with the requirement of extra accessories such as pumps, heat exchangers and other components, which results in the high cost [7]. Although HP BTM system has a high cooling efficiency, it normally requires a complex system structure and a high weight.

Compared with the conventional technologies, PCM BTM works independely without supportive energy input or extra accessories [8], and the latent heat employed during phase change process to manage the thermal environment is commonly much greater

than the sensible heat utilized in sensible type fluid cooling/heating systems. However, this technology is limited as conventional PCM, for example, paraffin wax (high heat capacity but low thermal conductivity), is inadequate for high heat fluxes, due to the limited characteristics in only one material. Moreover, another general issue of leakage could be raised due to the transition from solid phase to liquid phase of PCMs. The form stable phase change material (FSPCM) and the microencapsulated phase change material (MPCM) have been proposed and developed to tackle the leakage issue. The FSPCM used the supporting matrix to embed the conventional PCM, which could prevent the PCM leakage during the phase transition process [9-11]. The microencapsulated PCM employed the polymer shell to wrap the PCM core inside at the scale of nm-μm, which also confined the phase transition within the shell [12-14].

In this PhD project, two types of PCMs, FSPCM and Micro-encapsulated PCM slurry, were explored by being employed in the BTM system for EVs, HEVs, and FCEVs, with the aim of realingzing high performance battery temperature control.

1.2 Aim and objectives

Many research reported the application of PCM in the area of themal energy storage and management. However, the technology of PCM-BTM still has large uncertainty to be fully understood and developed. The disadvantages such as the leakage problem and the limited cooling power and capacity of PCM are still waiting for solution. The primary goal of this PhD research project is to explore the ultilization of PCMs in BTM system, typically, with the expectation to enhance the battery thermal condition and performance. The objectives of this PhD research are to:

- Review existing reports and studies covering battering thermal management, with the emphasis on the PCM-BTM. The background, developing history, features, advantages, disadvantages, and recent progresses are all included. The reports of FSPCM and MPCM were emphasized.
- Establish a mathematical model and simulation to evaluate and compare the cooling effect of using FSPCM and forced air-cooling in four different scenarios.

- Establish and optimize the manufacturing methodology of MPCM slurry for BTM. Experimentally investigate the BTM performance using the manufactured MPCM slurry.
- Conduct the numerical study of using MPCM slurry and FSPCM in the BTM. Evaluate the thermal management effect of such hybrid method by several representing performance indicators.

1.3 Structure of thesis

Corresponding to the aim and objectives listed above, this thesis will present the content in the form and the order of :

- Chapter 2 – A background research was reviewed in detail, the technologies applied in the field of battery thermal management was introduced with emphasizing PCM-BTM, the feartures of this typical methodology was evaluated by reviewing the applications and performance that have been reported on literatures, the gaps and the challenges at present were summarised to explain the motivation of this PhD project.
- Chapter 3 – An innovative FSPCM which included paraffin, expanded graphite (EG) and high-density polyethylene was studied for passive cooling of battery systems in electric vechicles. A numerical model of the passive cooling battery system was established as well as validated to analyse and further compare four different battery cooling scenarios. Besides, sensitivity analysis was conducted to investigated the influence of the FSPCM on the battery cooling performances in respect of parameters such as the thickness, EG mass fraction, and air velocity. MATLAB was used in this chapter.
- Chapter 4 – MPCM slurry was manufactured and tested for battery cooling. A BTM test rig was built. The thermal management performance of using the manufactured MPCM slurry and water were experimentally compared, under various operational conditions.
- Chapter 5 – The battery cooling performance using a hydrid method of MPCM slurry and FSPCM were simulated. The results were compared with that using the FSPCM only in BTM. ANSYS FLUENT was used in this chapter.

- Chapter 6 – Results and discussions were conluded with future suggestions for further improvement.

Chapter 2. Literature review

2.1 Introduction

The improvement of clean vehicles such as the pure electric vehicle (EV) [15-17], the hybrid electric vehicle (HEV) [18-20], and the fuel cell electric vehicle (FCEV) [21-23] requires the batteries with high specific power as well as high specific energy density. The enhancement of battery power performance requires the large-scale battery with high current discharge, which can raise thermal issues as they can generate huge amount of heat rapidly during the charging/discharging, for example, in the period of quick acceleration [24-26].

Chapter 2 reviews the developing history of the battery thermal management system from the aspect of the niche market of clean vehicles. Various types are introduced from the air/liquid thermal management to the focused PCM-BTMs in current PhD project. At the end of this chapter, the challenge in BTM at present is described, and the motivation of this PhD project is explained.

2.1.1 Clean vehicles

The energy supply is one of the greatest challenges in the twenty-first century at both global and local levels [27], and transportation covers approximately 30-35% of the global fuel demands among industrialized countries [28]. In addition, large amounts of various pollutants and greenhouse gases (GHG) are emitted during the fuel consumption. In 2009, 28% of all GHG emissions in the United States is occupied by transportation [29]. In 2017, transportation still took 28% of total GHG emissions in the United Kingdom, even though this value has been reduced 3% since the year of 1990 [30]. In China, the number of automotive has been rapidly increasing since 2000 [31], as shown in Tab. 2.1. Since 2004, in China, the fuel consumption limit standards have been established, and the vehicles applying alternative energy resources are promoted, with the aim to reduce oil consumption [32].

Tab. 2.1 The number of the automobiles in China from 2000 to 2010 [31].

Year	2000	2001	2002	2003	2004	2005	2006	2007	2008	2009	2010
Million	16.08	18.02	20.53	24.3	27.42	31.60	49.85	56.97	64.67	69.62	90.86

The clean vehicle including pure EVs, HEVs, and FCEVs, is regarded as technologies with the best possibility for the utilization of alternative energy sources [15-23]. The first EV was established by Robert Davidson in Britain, in 1873, which was roughly 12 years earlier than the appearance of the first gasoline vehicle [33], consisting of a power source with a converter, an electric motor, and a mechanical transmission system. HEV integrates the electric propulsion system with a conventional internal combustion system [18-20]. FCEV uses the fuel cell as the power system, which enables the vehicle to have high efficiency and little or zero emissions with the exhaust gas, water, and waste heat as the by-products [21, 22]. The electricity required by EV and the hydrogen needed by FCEV can be provided by clean processes driven by renewable sources such as solar energy, in principle. Moreover, EVs and FCEVs are the only potential replacement of the traditional internal combustion engine with zero emission [34]. This explains the reason that they are treated as the long-term solution to the energy shortage and environmental issues.

2.1.2 Power batteries and thermal issues

The main barrier of the wide adoption of EVs, HEVs, and FCEVs, at present, is still the high cost, especially fuel cost, as the assumptions summarized in Tab. 2.2 [31] (adapted from [35]). The assuming results may not be accurate, but the cost difference between the three candidates is assumed to be smaller.

Tab. 2.2 The summarised running fuel costs from 2010 to 2030 [31], adapted from [35].

Fuel cost (GJ^{-1})	2010	2030 Optimistic	2030 Pessimistic	2030 Average
Gasoline	\$12.7	\$19	\$38	\$28.5

Hydrogen	$42	$14	$56	$35
Electric	$36	$27	$45	$36

The power battery is the most cost item by far in the clean vehicles, and it is also the key hinder in spreading the battery-powered electric vehicles [36]. Numerous rechargeable power batteries exist for EVs and HEVs. The lead-acid battery was considered for the utilisation in EVs, at the begin in 1990s, due to its promising cost and specific-power properties [37]. However, this kind of battery has a short cycle-life, some research has been conducted to improve its cycle-life [37-39]. The constrained market acceptance of the lead-acid battery for EVs prompts the higher-specific energy battery, the Ni-MH battery as the new choice [40, 41]. It also exhibits longer cycle life, higher energy and power densities, and therefore this kind of battery has been commercially utilized since the invention in 1991 [42-46].

Battery safety is the key issue in the application of EV and HEV, and the poor cycle performance is mainly caused by the rapid and uneven temperature rise in the installed battery packs [47, 48]. During the charge-discharge cycle, many chemical and electrochemical reactions take place. When higher power is required, a higher current is needed. Operated at high discharge rate, the scaled-up cells raised the major concern of the temperature rise [3]. Much more heat can be generated by the battery in the rapid charge/discharge cycles at the high current, for example, during the vehicle acceleration process [49]. The improvment on the battery-based clean vehicle lies in the application of large-scale battery, however, severe thermal issues are caused by the increased battery size as well as the large pack forming [50, 51]. Overheating, combustion, explosion, and other safety risks increase with the energy amount within the battery [52].

It is important to know the mechanism of the thermal performance of the battery. In the Li-ion battery, heat can be generated by several processes and parts: the electrolyte and anode decomposition [53-55], the reaction of the anode and the adhesive [56, 57], the reaction of the cathode and electrolyte [58, 59], and the solid electrolyte interface film

[58, 60, 61]. During overcharge, Li-ion battery can have an internal temperature of 199 °C, which was even approximately 90 °C higher than that on the surface [62].

The cycle life of battery can be reduced by the excessive local temperature, as well as thermal runaway [63]. Tab. 2.3 presents the characteristics of few commercially manufactured batteries [4]. 1000 or more cycles at 80% discharge ratio are expected to be achieved by the battery for EVs [64]. For lead-acid, Li-ion and Ni-MH batteries, the optimal temperature range balancing the cycle life and performance is from 25 to 40 °C, with the temperature distribution is lower than 5 °C among modules [65]. Heat control is a significant part for Li-ion, Ni-MH and other batteries, as the charging efficiency and the longevity characteristics can be decreased at a temperature higher than 50 °C [66].

As a conclusion, temperature can affect the battery performance in the perspectives of electrochemical system, charge acceptance, round trip efficiency, power and energy capability, cycle life, cost, and reliability [65]. The importance of the safety risk raised by heat accumulation has been realized, and therefore researches on effective battery thermal management (BTM) are essential and urgently needed [67-69].

Tab. 2.3 Properties of several power batteries [4].

	Ni-MH	Lead-acid	Li-ion	Li-ion polymer
Cycle life (to 80% of initial capacity)	300-500	200-300	500-1000	300-500
Overcharge tolerance	Low	High	Very low	Low
Self-discharge/month	30%	5%	10%	~10%
Operating temperature (discharge)	-20 to 60 °C	-20 to 60 °C	-20 to 60 °C	0 to 60 °C

2.2 Battery thermal management

2.2.1 Methodologies

Corresponding to the previous analysis, two main issues are caused by the thermal effect of battery. The first one is that, during charge and discharge, the high temperature can result into the exceeded temperatures over permissible levels, and thus the battery performance is negatively influenced. The other problem is that the unevenness of the temperature distribution in the battery package can lead to the deterioration at local. Therefore, within the cell or between the cells, the accomplishment of the temperature uniformity can maximize the cycle life and the performance of the cell, the module, and the package [70].

To enhance the battery performance, the thermal management system should enable [71-73]:

- Optimal working temperature range for each cell and each battery module, releasing heat to the ambient when hot or absorbing heat from the ambient when cold
- Small variations of the temperature within the cell and the module
- Small variations of the temperature among multiple modules
- Small size and low weight, easily to be packed, cheap, reliable, and easily to get services
- Ventilation when hazardous gases are potentially generated by the battery

The BTM system can be either passive or active, by only using the ambient environment or with a built-in energy source. They can be categorized based on medium [31]:

- Air (Fig. 2.1)
- Liquid (Fig. 2.2)
- Phase change material (PCM) (Fig.2.3)
- Combination of the above

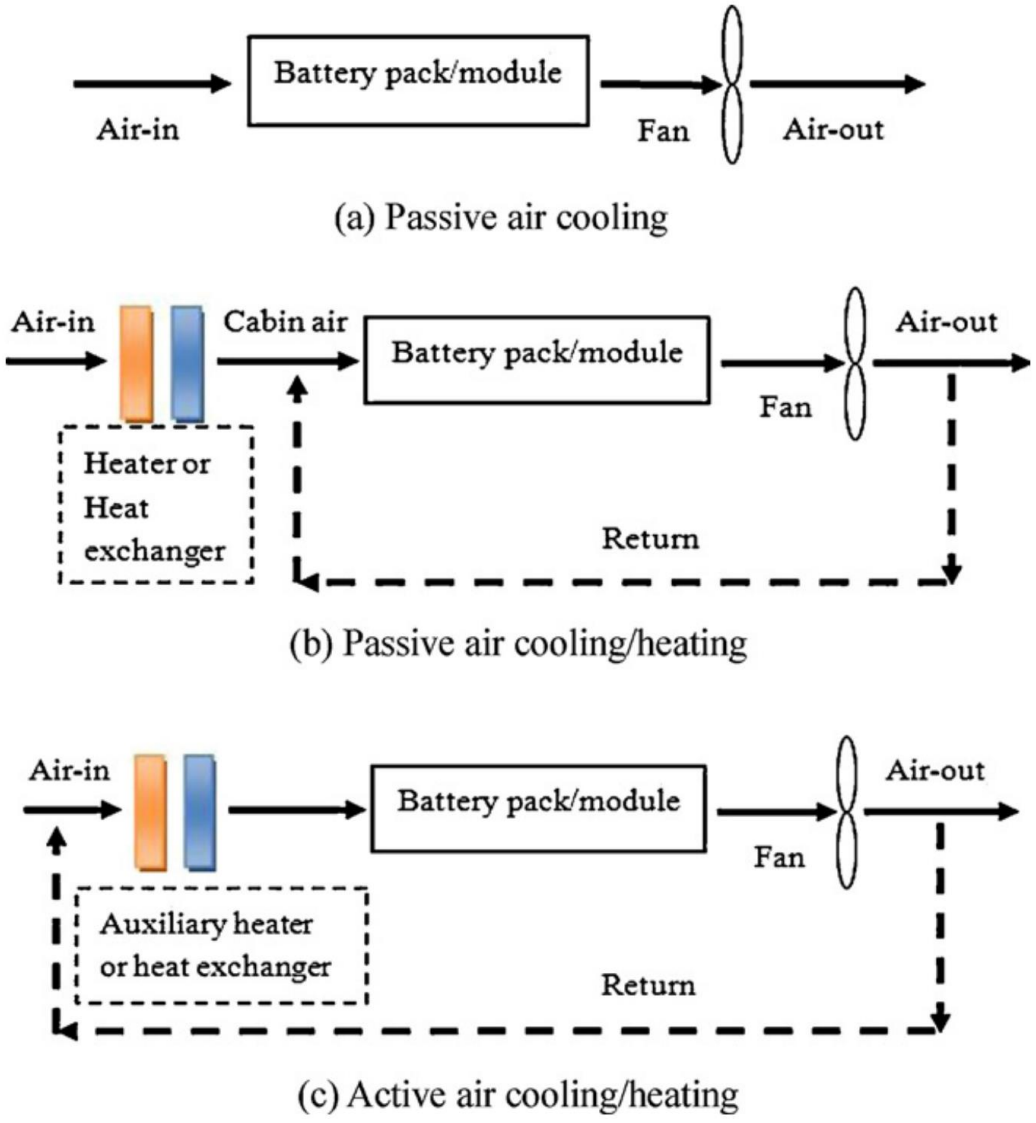

Fig. 2.1 BTM using air [31].

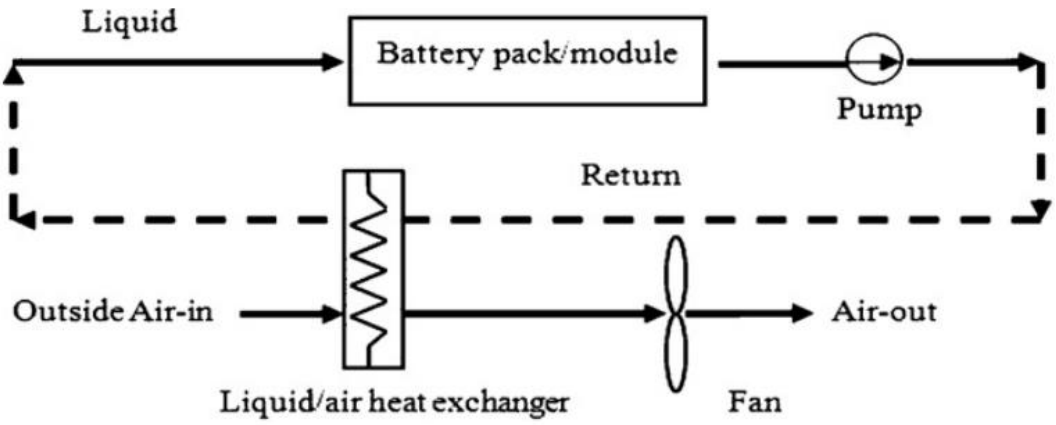

(a) Passive liquid cooling

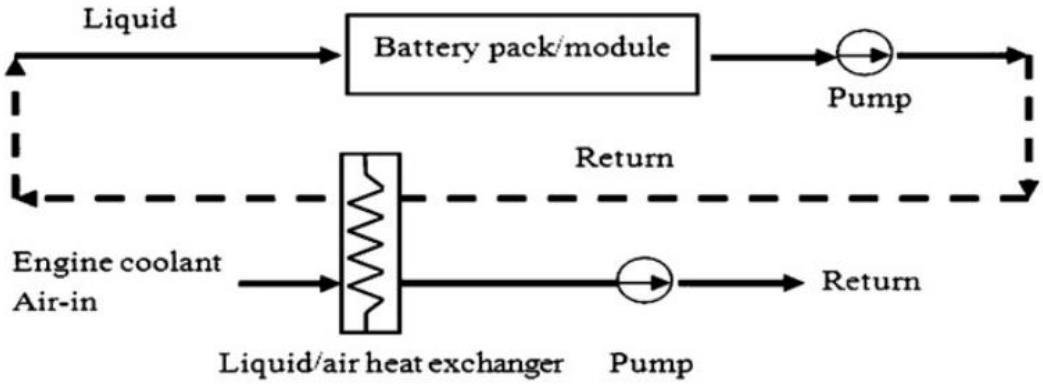

(b) Active moderate cooling/heating

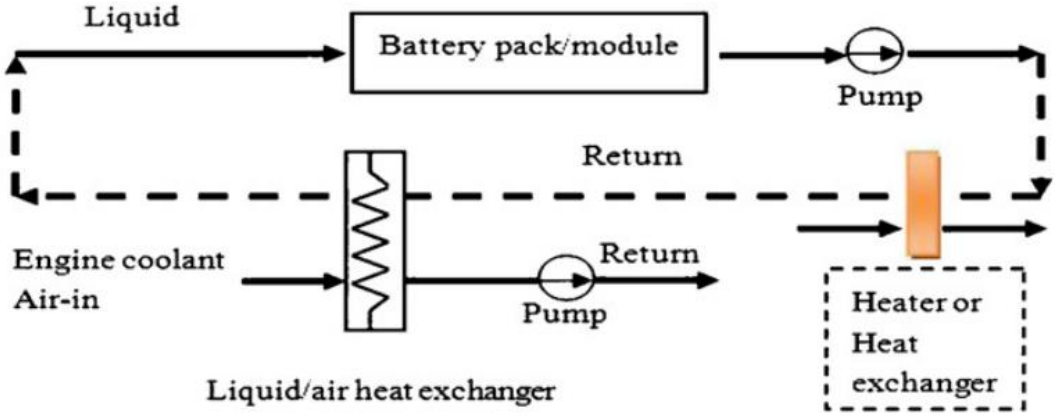

(c) Active cooling (high temperature)/heating (cold temperature)

Fig. 2.2 BTM using liquid [31].

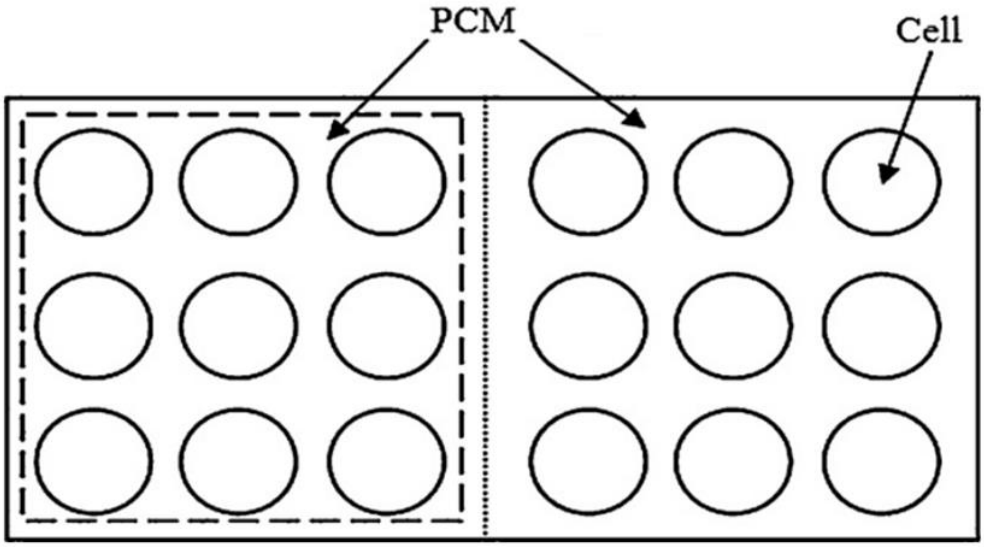

Fig. 2.3 BTM using PCM [31].

2.2.2 Air for thermal management

Fig 2.4 presents the commonly used cell configurations of the battery pack design [74]. This methodology may be the simplest BTM system, and it is used due to the cost and space limitations [75]. As the battery pack shape is regular, two ways are usually adopted for the air flow as shown in Fig. 2.5 [31].

The natural air convection is apparently not enough for the battery heat dissipation, and thus the air is directed or blowed parallel or serial across the battery. The parallel airflow was used in a Toyota HEV [76]. The forced air system has a vent for returning cabin air and another vent to supply air from outside. A cinquefoil battery pack was designed with 5 long modules (total voltage is 36V) to improve the heat transfer in Ni-MH battery, as displayed in Fig. 2.6 [77]. The result demonstrated that the temperature drop meets the expectation, even though the temperature difference is still high. Additionally, the structure used in this battery is quite complex. Large temperature drop was found in the cell near the fan (3a).

Air forced convection cooling can hardly cool the battery to lower than 52 °C when the battery temperature is above 66 °C [78]. What's more, given a stressful condition, air-cooling may not be proper, and the uneven temperature distribution on the battery

surface can be inevitable, especially when the discharge rate is high, or the working or ambient temperature is high [79].

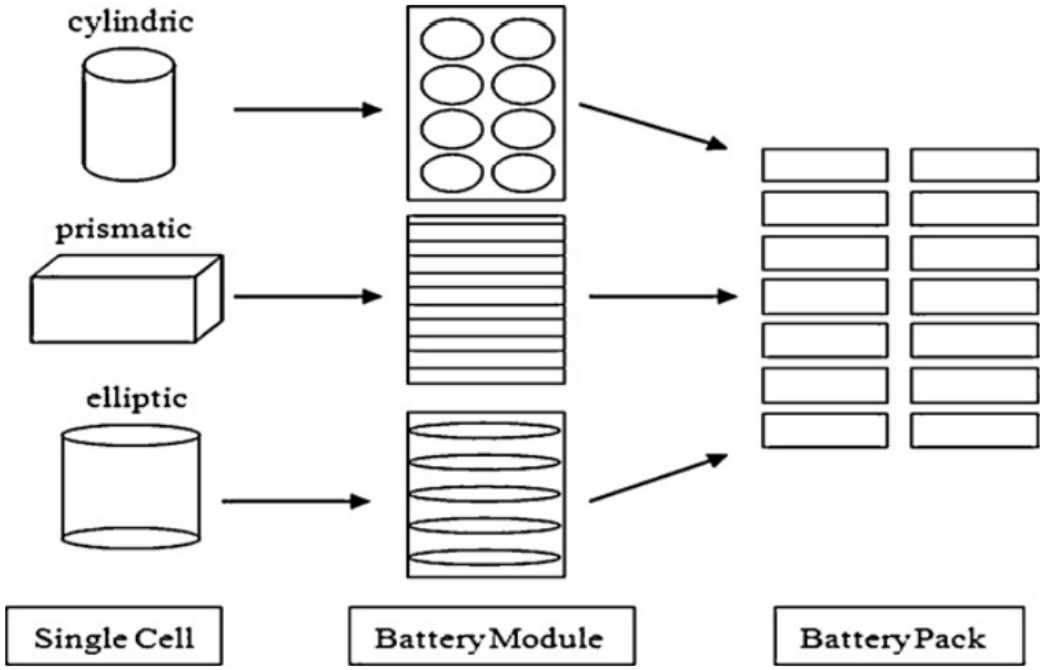

Fig. 2.4 Schematic diagram of various battery pack designs [74].

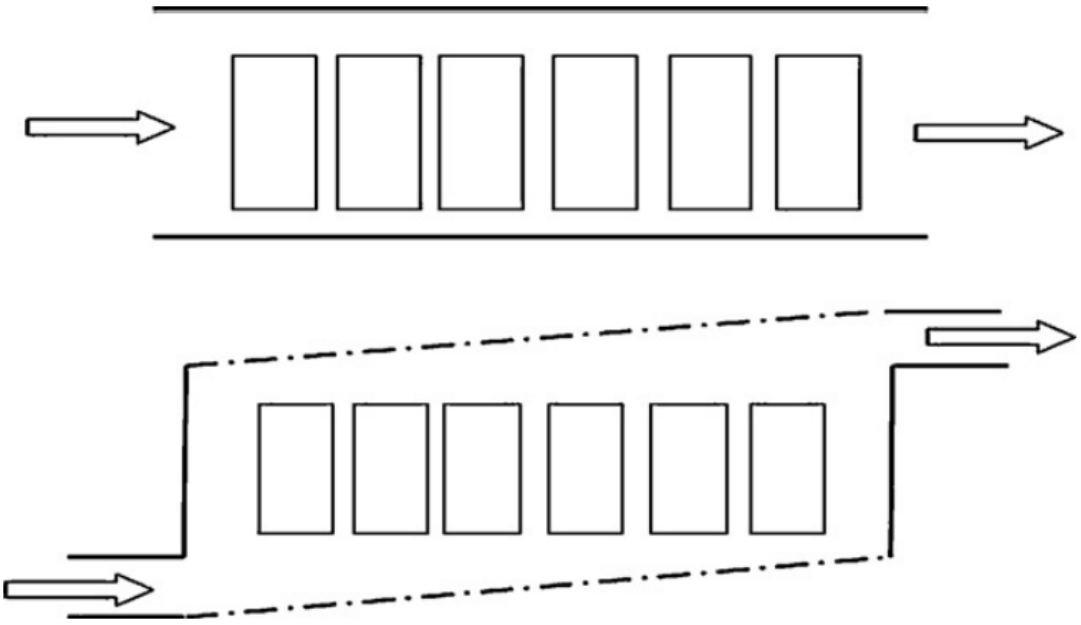

Fig. 2.5 Air flow ways in the battery [31].

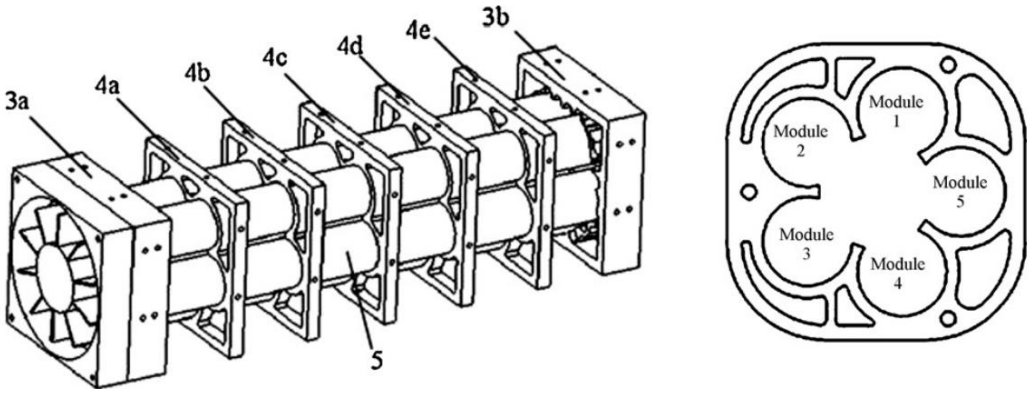

Fig. 2.6 Schematic of the cinquefoil battery [77].

Furthermore, below the temperature −30 °C, the battery power, for instance, Li-ion battery power, is severely limited even it has high power density [80]. Given the condition of cold winter (<−30 °C), the battery requires to be rapidly heated right after a cold start-up. For a delivering power of 25 kW, only 1/5 of this power can be provided by the battery at −30 °C [78]. The battery cannot heat itself with Joule heat rapidly. In this case, actively heating the battery pack must be taken into consideration. Two ways are suggested:

- With electric heaters in the battery pack
- By heating the battery coolant using the wasted heat transferred from the engine coolant

As it is obviously difficult to heat the battery rapidly by using the air, liquid such as water is considered for BTM, as it presents higher heat transfer performance compared with air.

2.2.3 Liquid for thermal management

Neither the natural or forced air convection could significantly alleviate the thermal issue of the packed battery, especially the one with large scale [81], which leads to the application of liquid medium. The BTM applies liquid by either a jacket surrounding the modules, through the discrete tubes in the modules, mounting the modules on a plate with liquid temperature controlling system, or directly submerging the module

into the dielectric fluid [82]. The liquid medium includes various subjects, such as water, oil, glycol, acetone and even some refrigerants.

The performances of liquid and air BTM system were compared in [82]. Generally, even though air BTM was less complicated, compared with liquid BTM, it was also less effective. Air BTM can be adequate to meet the requirement for parallel HEVs, whereas liquid BTM might be desired for EVs and series HEVs. In 2010, the Panasonic (CGR18650E) cells were utilized in a triangular aluminium module and were placed under water [83].

However, the liquid leakage prevents manufacturers to widely adopt this technology. Heat pipe, using phase change heat transfer, has raised increasing attractions as one special liquid BTM to some extent. It is composed by a sealed container with capillary wicking material modified inner surface. This material could provide the driving force to return the condensed liquid directly to the evaporator. Attached to the battery wall, two heat pipe with aluminium fins were employed to mitigate the battery thermal effect [79]. The results demonstrated that the temperature rise was significantly reduced by the heat pipes, especially with the metallic aluminium fins. A loop thermosyphon, similar with the heat pipe, was adopted as high efficiency BTM [84]. It was combined with air cooling. The heating section was distributed over the battery surface, while the fan blew the air over the condenser. The experimental results presented that the working temperature was under 45 °C using acetone or 50 °C using water water as working fluid, respectivley. A lot of works were conducted in a thesis designing a pulsating heat pipe (PHP) for the BTM. The researched battery was Optima Sprirocell lead acid battery (12V, 65Ah). Fig. 2.7 depicts the closed loop PHP, while Fig. 2.8 illustrated the system placing the batteries in the boot of HEV. Consequently, a suitable PHP should be constructed with enough space to employ ammonia as the working fluid. It also exhibited that with well design, PHP was feasible to be applied in BTM.

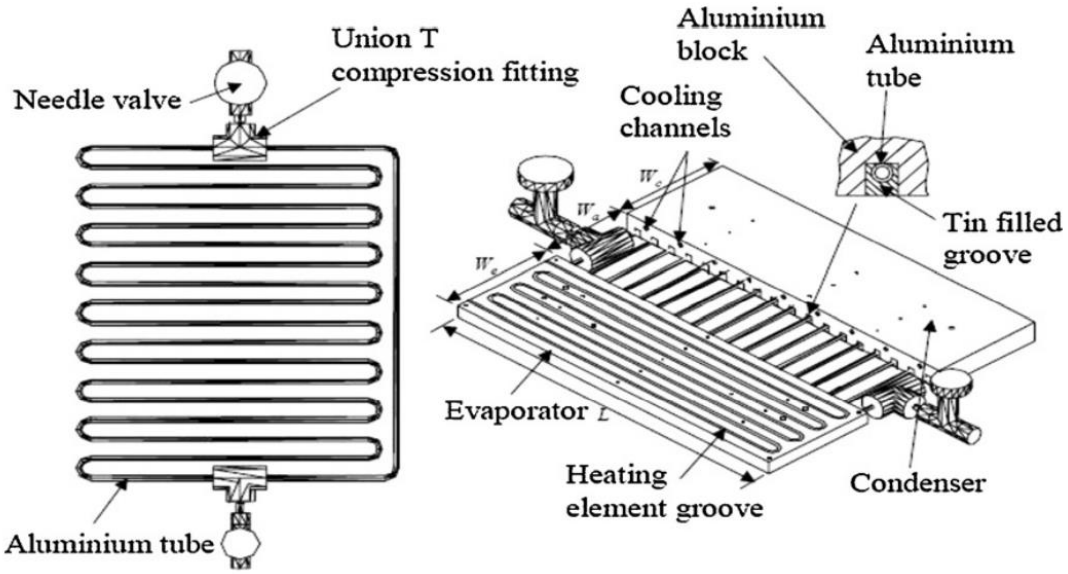

Fig. 2.7 Schematic diagram of the aluminium closed loop PHP [85].

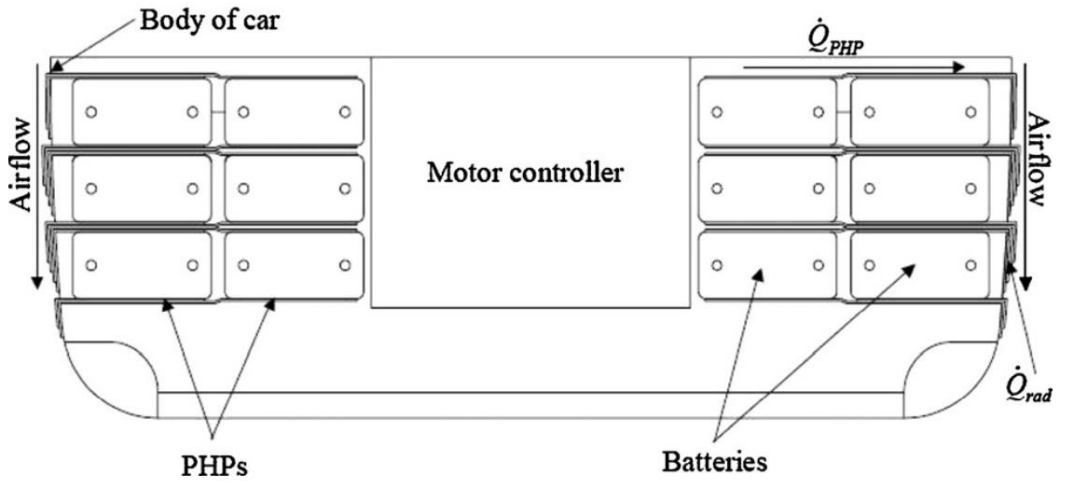

Fig. 2.8 Schematic diagram of the PHP employed in HEV [85].

2.2.4 PCMs for thermal management

BTM systems with air or liquid can be either too bulky, complex, or expensive (need fans, blowers, pipes, pumps, and other accessories) [4], which results in the development of novel solutions utilizing PCMs. PCM BTM system has been demonstrated and patented by Al-Hallaj and Selman with performance better than conventional BTM [86].

A PCM BTM system was designed and simulated using the entropy coefficient method for the laptop [87], whose results demonstrated that this methodology could

significantly improve the system performance by keeping the working temperature of battery lower than 55 °C, even at a high discharge rate. Besides, four distinguished modes of heat dissipation were researched for a Li-ion battery in an electric scooter [88]. The heat dissipation modes included the natural convection cooling, aluminium foam heat transfer matrix, PCM passive cooling, and the combination of the aluminium foam with PCM. The experimental tests presented that the combined heat dissipation mode was the optimal one among all candidates. Moreover, future work was suggested to continue within the conductivity exploration of PCMs.

Even under a stressed condition, regarding of the conduction and absorption of heat, PCM passive cooling offers safety to battery. The validity of applying PCM in high-energy Li-ion BTM was confirmed experimentally under both normal and stressed working conditions [89]. A compact 18650-cell module (4S5P) with PCM BTM was demonstrated, which indicated that the passive thermal management can be used under the normal or stressed condition to maintain the uniform temperature distribution of battery [70]. The effectiveness of BTM using PCM and air forced cooling was investigated numerically and experimentally [63]. In this study, the PCM BTM kept the operation temperature under 55 °C, given a constant discharge rate (6.67C, 10A/cell). PCM could also be integrated with air cooling. In cylindrical Ni-MH (2200 mAh, SC-Ni-MH) and Li-ion rectangle batteries, the composite PCM which has high conductivity was employed for thermal management, at a high discharge current [90]. The result showed that BTM using the PA/EG composite (20 wt%) could control the battery temperature under 40 °C, while within 8 min the blank group temperature could exceed 55 °C.

Typically, for the low working temperature, PCM takes advantage for EVs operated in the astronavigation or cold conditions where the battery temperature can greatly decrease. When the battery temperature drops lower than the melting point of the PCM, the latent heat stored in the material can release heat to the surrounding modules and maintain the working temperature of the battery. For high working temperature, large amount of heat released by battery can be absorbed by PCM around the melting temperautre of PCM, so that to achieve battery cooling and temperture control. At ambient condition, melted PCM will be cooled and solidified, cold energy is then stored.

In 2004, a trade-off analysis of the various BTMs was conducted [91]. According to the

recent research, the analysis was further fulfilled as displayed in Tab. 2.4 [31]. Relatively, two technologies among them were not recommended. One was the thermoelectric cooling, which had low coefficient of performance (COP), while the other was the cold plate, which was directly contacted with the walls of the battery but had a high thermal resistance. The analysis concluded that PCM passive cooling for battery was a promising solution.

Tab. 2.4 The trade-off analysis table of BTM [31].

	Air forced	Liquid	Heat pipe	PCM	Thermoelectric	Cold plate
Ease of use	Easy	Difficult	Moderate	Easy	Moderate	Moderate
Integration	Easy	Difficult	Moderate	Easy	Moderate	Moderate
Efficiency	Low	High	High	High	Low	Medium
Temperature drop	Small	Large	Large	Large	Medium	Medium
Temperature distribution	Uneven	Even	Moderate	Even	Moderate	Moderate
Maintenance	Easy	Difficult	Moderate	Easy	Difficult	Moderate
Life	>=20 years	3-5 years	>=20 years	>=20 years	1-3 years	>=20 years
First cost	Low	High	High	Moderate	High	High
Annual cost	Low	High	Moderate	Low	High	Moderate

2.2.5 Thermal management in PEMFC

The temperature range within which the proton exchange membrane fuel cell (PEMFC) can work well and reliably is moderate, which also requires rational thermal management for high-power applications. The performance of PEMFC is determined by the water vapor amount. It means the uneven temperature which can result in the water condensation or local dehydration can lead to PEMFC performance degradation [92]. The thermal management should maintain the proper working temperature of the fuel cell as well as the even temperature distribution [92]. The challenges and solutions

of the thermal issues related to PEMFCs were reviewed in many reports [93-95]. Both the high temperature and low temperature fuel cells were discussed towards the thermal management issues, and an overview of fuel cell modelling works was provided. A three-dimensional and non-isothermal numerical simulation model of PEMFC was developed to explore the water and heat management [96]. The results exhibited that severe mass transfer limitation might exist determined by the water management or the design. Besides, in the cathode reaction rate, cell temperature plays an important role, and in the dehydration of the polymer membrane. A three-dimensional thermal simulation was established by a nodes network model of two PEMFCs (3 cells/150 W and 20 cells/500W) [97]. The internal temperature of PEMFC was predicted with different functional layouts, and the model was validated with various inlet water temperatures without loads, or with various loads ranging within 0.3 to 0.5 A/cm^2. A methodology was proposed including the influence of non-condensable gases in a one-dimensional, steady-state, and isothermal fuel cell with a pressure drop mode of the simple channel-groove [98]. The results demonstrated that the mode in which the membrane humidification cooperates with the anode recycling got better performance. A thermal management model using phase change, with a non-isobaric and non-isothermal water, was built to simulate the energy and mass transfer towards uneven stack temperatures [99]. The simulation results revealed that the inlet flow temperature increment could overcome the problem of water starvation. Moreover, the decrease of the cooling temperature enhances the PEMFC performance. A non-isothermal and three-dimensional model was developed to include the phase transportation and humidification [100]. The thermal and water management was at high current densities. The simulating results displayed that the water and thermal management could be affected by both through-plane and in-plane permeabilities, especially for that permeability was low. In addition, the isotropic permeability conditions used in the modelling might result in the overprediction of the cell performance or inaccuracy in predicting the thermal and water management.

2.3 Battery thermal management using PCM

BTM using PCMs has better performance for both cooling at high temperature and heating in cold conditions, compared to air or liquid BTM. PEMFC is quite unique but

in this PhD project battery is focused rather than fuel cells, towards the application in EVs, and HEVs.

2.3.1 Classification of PCM

The thermal energy is stored in PCMs as both of latent heat and sensible heat, and the latent heat possesses the major proportion in it due to the material's high latent heat capacity. Latent heat is the heat released or absorbed when PCM changes from one phase to another phase, for example, solid to liquid, or liquid to gas, or a special form of phase change in which, for example, the material is still in solid state but with its structure like the crystal lattice changed. The phase change process normally happens at a relatively constant temperature.

Various PCMs are available in a wide temperature range, and their classification can be referred to Ref [101-103]. PCMs can be generally separated into inorganic, organic and eutectic. In 1940s, the research in PCMs was pioneered without receiving much attention until the late 1970s to early 1980s, when the energy crisis took place. The development of PCMs was reviewed [101, 102], as so did the mathematical simulations based on the first and the second law [104]. Moreover, the enhancement progresses of PCMs in the latent thermal storage systems were reviewed [105]. Particularly, the investigation and development of high-temperature PCMs were reviewed [106]. Most researchers accepted that PCMs could be an effective methodology for thermal energy storage.

2.3.2 Selection of PCMs for BTM

Selection of proper PCM can be a key component for an effective BTM. The primary criteria of PCM selection for BTM are:

- The melting point of the material should be within the desired working temperature range.
- The material should have the characteristics of high specific heat, high latent heat, and high thermal conductivity.
- The material should not have large volume change during the phase transition

process.

- The material should have little or zero subcooling issue in the period of freezing.
- The material should be stable, non-flammable, non-poisonous, and non-explosive.
- The material should be easily accessible with low cost.

Significantly, the PCM selection for BTM requires the appropriate melting temperature range. For instance, the best temperature range is between 25 and 40 °C for Ni-MH, Lead acid, and Li-ion batteries, as commented in Section 2.1.2. Tab. 2.5 summarized the PCMs in the perspective of thermophysical characteristics towards various applications, with the extraction of the temperature range of 25 to 40 °C [101]. Quite specially, paraffin wax has a mostly straight chain, n-alkanes, CH_3-(CH_2)-CH_3. It is stable and chemically inert when the temperature is lower than 500 °C, and it has very limited volume change during melting [102]. Tab. 2.6 presents the thermophysical characteristics of the mentioned paraffin wax, which makes it the competitive candidate for BTM [102].

Tab. 2.5 Thermophysical characteristics of various PCMs [31].

Compound	Melting point (°C)	Laten heat (kJ/kg)	Thermal conductivity (W/mK)
GR25	23.2-24.1	45.3	-
RT25-RT30	26.6	232.0	0.18 (liquid) 0.19 (solid)
n-Octadecane	27.7	243.5	0.148 (liquid) 0.19 (solid)
$CaCl_2 \cdot 6H_2O$	29.9	187	0.53 (liquid) 1.09 (solid)
$Na_2SO_4.10H_2O$	32.39	180	0.15 (liquid) 0.3 (solid)
Paraffin wax	32-32.1	251	0.514 (liquid) 0.224 (solid)
Capric acid	32	152.7	0.153 (liquid)
(PEG900)	34	150.5	0.188 (liquid) 0.188 (solid)
Lauric-palmitic	35.2	166.3	-
Lauric acid	41-43	211.6	1.6
Stearic acid	41-43	211.6	1.60 (solid)
Medicinal paraffin	40-44	146	2.1 (liquid) 0.5 (solid)

Paraffin wax	40-53	-	-
P116-Wax	46.7-50	209	0.277 (liquid) 0.140 (solid)

Tab. 2.6 Thermophysical properties of paraffin [102].

Formula	Molecular weight (g/mol)	Melting point (°C)	Latent heat (kJ/kg)
C15H36	240	21.7	213
C18H38	254	28.0	244
C19H40	268	32.0	222
C20H42	282	36.7	246
C21H44	296	40.2	200
C22H46	310	44.0	249
C23H48	324	47.5	232
C24H50	338	50.6	255
C25H52	352	49.4	238

2.3.3 Enhancement in thermal conductivity

However, paraffin has the disadvantage of the low thermal conductivity, which can result in a poor heat tranfer between PCM and battery and thus low cooling power. Enhancement of the paraffin thermal conductivity is desired for BTM development. Pure paraffin is hard to meet the requirement of high heat fluxes. To alleviate the conflict between the low thermal conductivity and the large heat storage capacity, composite PCM can be used by mixing PCM with high thermal conductivity matrixes. Tab. 2.7 concluded some pure and composite PCMs that has been investigated in BTM [31]. The symbol K is the heat transfer coefficient, and L is the latent heat. The term c_p is the specific heat capacity. T_m is the melting temperature.

Tab. 2.7 The desired PCMs for BTM [31].

Ref	Method	PCMs	K ($W \cdot m^{-2} \cdot K^{-1}$)	L (kJ/kg)	T_m (°C)	c_p (kJ/kg·K)
[4]	Simulation	PW	0.21/0.29	195	40-44	1.77
[88]	Experiment	PCM/AF	-	-	-	-

	Simulation					
[107]	Experiment	PW	0.12/0.21	173.4	46-48	289
	Simulation					
[70]	Simulation	PW/graphite	16.6	123	42-45	1.98
[63]	Simulation	PCM/graphite	16.6	181	52-55	1.98
[89]	Simulation	PCM/graphite	16.6	185	42-45	1.98
[87]	Simulation	PCM/EG	16.6	127		1.98
[108]	Experiment	PCM/EG	4-26	-	~55	-
[109]	Experiment	PCM/EG	14.5 (2h)	-	-	-

EG: expanded graphite; AF: aluminium foam; PW: paraffin wax.

Many materials having high thermal conductivity have been used as additives to manufacture composite PCMs, for the enhancement of the PCMs thermal characteristics, especially for paraffin, as summarized in Tab. 2.8 [31]. From the table, it is obviously that the thermal conductivity is improved by the methodology of adding high thermal conductivity material to composite PCM.

Tab. 2.8 Thermal characteristics of the composite PCMs of paraffin base [31].

Ref	PCMs	K ($W \cdot m^{-2} \cdot K^{-1}$)	L (kJ/kg)	T_m (°C)
[110]	Paraffin/HDPE-EVA/OMT	-		
	(1)75%/25%/0		(1) 111.52	(1) 57.65
	(2)75%/2.5%/22.5%		(2) 99.78	(2) 57.92
	(3)75%/5%/20%		(3) 97.21	(3) 57.13
	(4)75%/10%/15%		(4) 91.66	(4) 57.33
[111]	Paraffin75%/PSC25%	(1) 0.387	(1) 165.16	(1) 56.3
[112]	Paraffin/Al2O3			
	(1) 95%/5%	-	(1) 225.6	(1) 26.0
	(2) 90%/10%		(2) 212.3	(2) 26.3
[113]	Paraffin/Aluminium	4.09	266	53.5
[114]	Paraffin/HDPE/APM/EG			
	(1)60%/40%/0/0	(1) 0.28	(1) 68.3	(1) 51.59
	(2)60%/20%/20%/0	(2) 0.29	(2) 74.7	(2) 50.58

	(3)60%/15%/25%/0	(3) 0.34	(3) 81.5	(3) 51.70
	(4)60%/20%/15%/5%	(4) 0.51	(4) 68.8	(4) 51.10
	(5)60%/15%/20%/5%	(5) 0.85	(5) 73.5	(5) 50.58
[115]	Paraffin/HDPE/EG/APP			
	(1) 60%/15%/2%/23%	-	(1) 91.23	(1) 56.01
	(2) 60%/15%/4%/21%		(2) 90.89	(2) 56.31

HDPE-EVA/OMT: polyethylene/poly/organophilic montmorillonite; PSC: porous silica ceramic; HDPE: high-density polyethylene; APM: ammonium polyphosphate (APP), pentaerythritol (PER) and melamine (MA); APP: ammonium polyphosphate.

2.3.4 Behaviour in thermal-mechanical aspect

Compared to the discussion of thermal conductivity, very limited research was conducted to explore the mechanical characteristics of PCM, which is obviously significant in the practical application. It is essential for the material to withstand the negative thermo-mechanical issues while in use [109]. A systematic experimental exploration was performed to evaluate the effects of the thermal-mechanical characteristics, such as thermal conductivity, bursting and tensile compression of the prepared material of composite PCMs (paraffin wax/expanded graphite), for Li-ion batteries. The behaviours of the composite PCM with various impregnation times were listed in Tab. 2.9 [109]. The results demonstrated that the increment of the paraffin wax percentage in the composite material resulted in the increment of both compressive and tensile strengths at room temperature, or the decrease of both strengths at a relatively higher temperature. In the future, more relative works should be conducted to explore the thermal-mechanical properties of the PCMs.

Tab. 2.9 Thermo-mechanical properties of PCMs impregnated with different times [109].

Property	Specification				
	12h	9h	6h	3h	1h
Thermal conductivity (W/(m·K))	14.5	14.3	14.1	13.6	13.0
Bulk density of composite (kg/m^3)	789	775.4	766.3	660.4	622.5
Bulk density of graphite (kg/m^3)	210	210	210	210	210

Tensile strength (22 °C) (kPa)	1040	1060	1072	1100	892
Tensile strength (45 °C) (kPa)	196	186	194	260	264
Compressive strength (22 °C) (kPa)	2571	2546	2394	2317	2292
Compressive strength (45 °C) (kPa)	292	280	280	267	241
Bursting strength (22 °C) (MPa)	650	630	600	560	530
Bursting strength (45 °C) (MPa)	110	130	140	140	160

2.4 FSPCM

Among the extensive research towards PCMs, paraffin (PA) wax, mostly composed by a mixture of straight chain *n*-alkanes CH_3-(CH_2)-CH_3, has been demonstrated its popularity in the BTM applications [116]. However, the leakage issue during the application of PA needs to be addressed.

Many strategies have been developed to prevent PA from leakage, for an instance, the form stable PCM (FSPCM) [117]. [117]. Blended with porous carbon materials or polymers, liquid PA could be retained in the matrix and the composite material can be categorized as FSPCM, which prevents liquid from volatilization or leakage [118]. Various raw materials with porous structures could be applied as supporting matrix for PA, such as polypropylene [119], expanded perlite [120], diatomite [121], high-density polyethylene (HDPE) [122]. HDPE could have very limited effect on the melting point of the source PA, which enables it to be a promising candidate for manufacturing FSPCM [116, 122].

Form-stable PA potentially, however, has the disadvantages of the low thermal conductivity, due to the low average thermal conductivity of the source PA, only 0.2 W/(m·K) [123]. Expanded graphite (EG), with a layered structure, is commonly used as the additive to improve the thermal conductivity of the FSPCM [124]. By adding 4.3 wt% EG, the thermal conductivity of the form-stable PA/HDPE composite was enhanced to 1.36 W/(m·K), four times higher than that of without adding EG [125].

Much research focused on investigating the characteristics of the FSPCM, but studies of using FSPCM, especially PA/HDPE with EG-additive, into BTM are limited.

2.5 MPCM

Except from the FSPCM, encapsulation of PCM, which puts PCM into a sealed box, bag, ball, or capsule, by either chemical or physical approaches, could also prevent PA from leakage [126]. The encapsulated PCM was found with the ability to isolate the PCM from the surroundings, therefore, it could prevent the leakage, corrosion, or reduce the reaction with the outsides. Moreover, the thermos-mechanical property was improved, which also enhance the flexibility of using the frequent or conventional PCMs [127]. According to the size, the encapsulation of PCM could be categorized into micro-encapsulation (<1 mm) and macro-encapsulation (>1 mm).

2.5.1 Macro-encapsulated PCM

Macro-encapsulated PCM was widely applied in the photovoltaic thermal (PV/T) systems, with the aim of thermal management, as well as heat storage.

Modjinou et al. [128] adopted panels of aluminium (Al)-coated PCM to elevate PV/T system performance, as shown in Fig. 2.9. The results demonstrated that by the application of Al-coated PCM panels, the freezing issue of the regular PV/T systems was prevented to some extent.

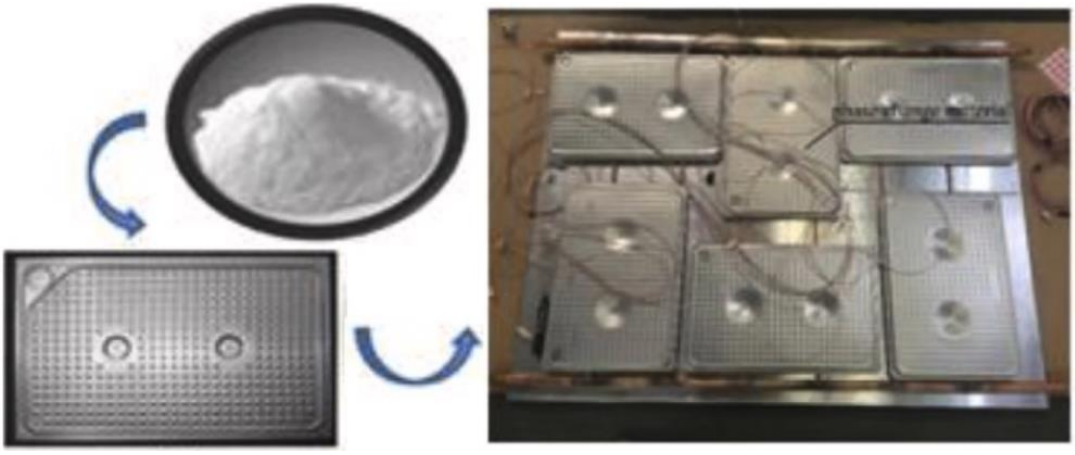

Fig. 2.9 Macro-encapsulation of PCM example: using Al-coated PCM panels [128].

Similarly, Fayaz et al. [129] applied the PCM bags in PV/T systems, as presented in Fig. 2.10, which improved the electrical efficiency of the system by approximately 7 %. The addition of PCM bags could have dual benefits of both heat storage and cooling

effects, in this case.

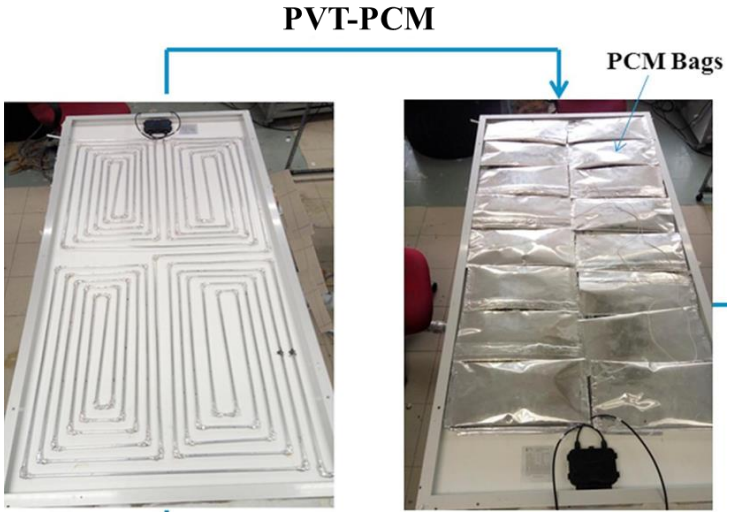

Fig. 2.10 Macro-encapsulation of PCM example: using PCM bags.

PCM was encapsulated into spheres to avoid the burning of PV/T modules [130]. Fig. 2.11 exhibited the product of the PCM-encapsulated spheres and the small-scale concentrating PV/T module [130]. The result showed that the thermal, electrical, and overall efficiencies with PCM-encapsulated spheres were higher than 5%, 10%, and 15%, respectively, compared with the water-cooling system.

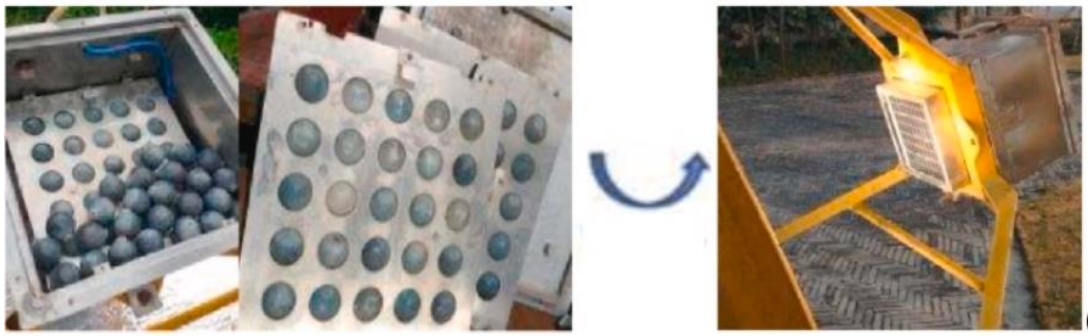

Fig. 2.11 Macro-encapsulation of PCM example: using PCM-encapsulated spheres [130].

2.5.2 Micro-encapsulated PCM

PCMs could also be micro-encapsulated to form a shell-core structure to avoid the issues of leakage or corrosion and to improve the thermal performance of the system.

Many manufacturing methodologies have been established to synthesize the micro-encapsulated PCM (MPCM), for example, interfacial and emulsion polymerization, in-situ suspension, and so on [131].

Yan Zhang et al. [132] researched on the hydrocolloids assisting encapsulation PCMs to prevent the volatilization, for the application in cryogenic energy transport and storage. Fig. 2.12 (a) presented the selected hydrocolloids for capsule synthesis, while Fig. 2.12 (b) was the OM (optical microscopy), FM (fluorescence microscopy), and SEM (scanning electron microscopy) image of MPCM in various high-payload capsules [132]. GEL, CHI, MC, LBG, PEC, and XG respectively stand for gelatine, chitosan, methylcellulose, locust bean gum, pectin, and xanthan gum. These findings provided fundamental information of achieving high quality MPCMs with far-reaching impacts beyond the application in cryogenic energy transport and storage.

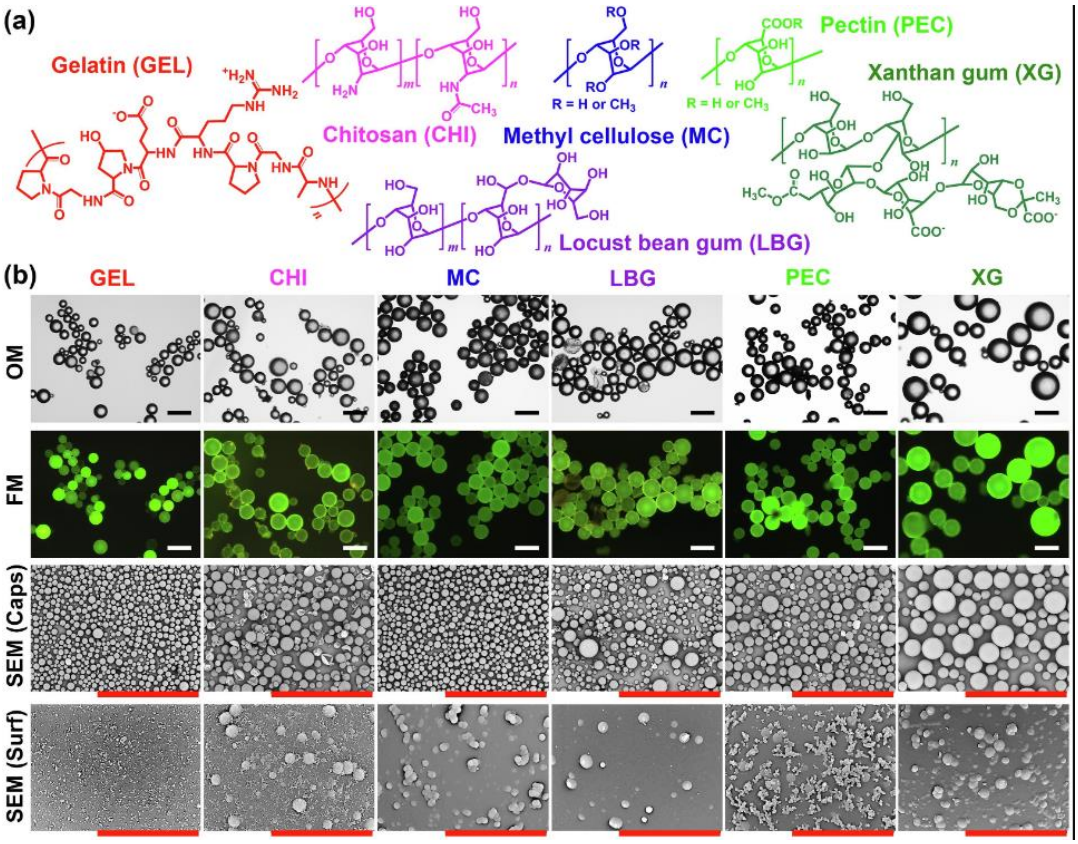

Fig. 2.12 The principle chemical structure of the selected substances and the morphology characterizations [132].

MPCM could suffer from the cracking or buckling issue which affects the material

effectiveness and stability. A thermo-mechanical coupled model was developed to decide the critical conditions, which could help to avoid the buckling or cracking in terms of material selection and shell thickness [133, 134]. Fig. 2.13 illustrated the geometry of the spherical MPCM particle [133]. The boundary conditions were also pointed out in the figure. The result demonstrated that the reduction of capsule shell thickness could enhance the energy storage capacity as well as the energy charging rate. However, the mechanical stability could be decreased at the same time.

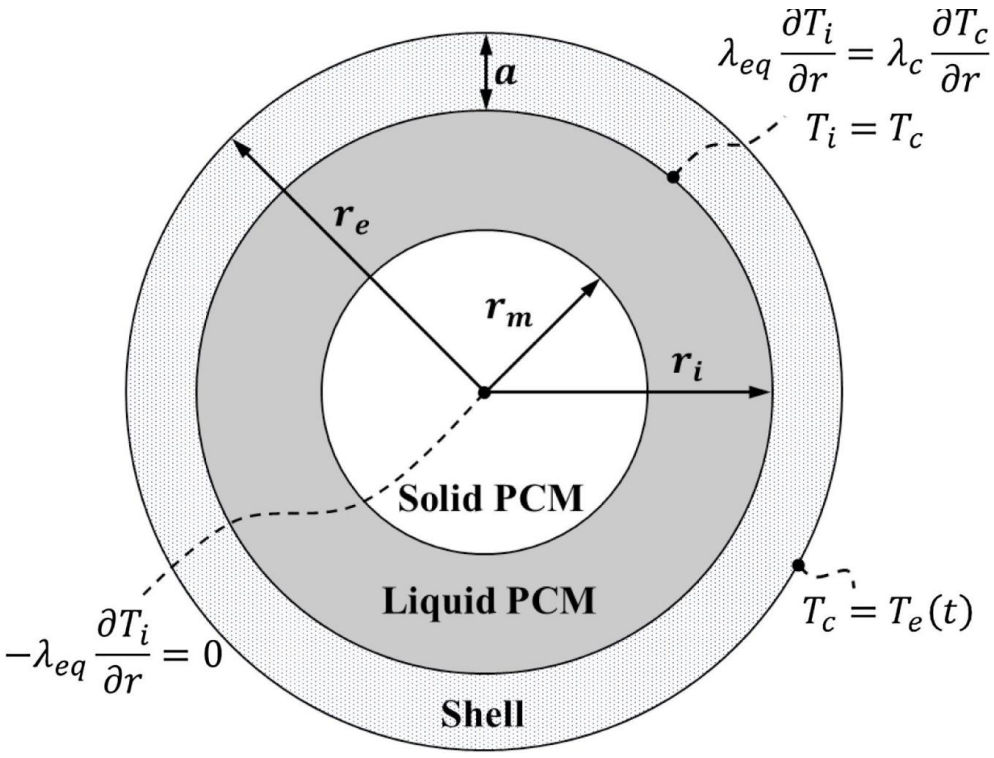

Fig. 2.13 The geometry and boundary conditions in a spherical MPCM particle [133].

Dispersing MPCM particles uniformly into the carrying fluid medium, such as water, can form MPCM slurry, if the size of the MPCM particle is small enough to enable the suspension in the carrier fluid, generally with a diameter less than 100 μm, as illustrated in Fig. 2.14 [135]. Phase change could take place inside the shell with a solid to liquid core for heat absorption and a liquid to solid core for heat release [136].

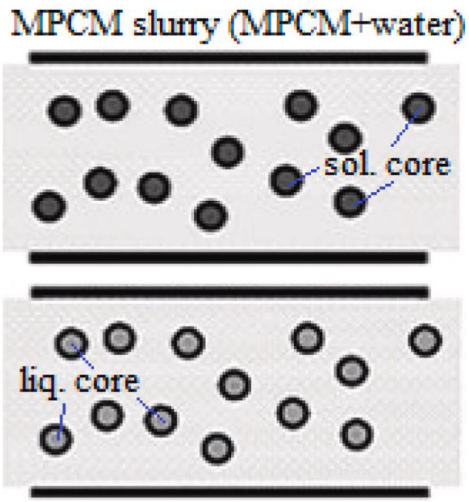

Fig. 2.14 The schematic diagram of the MPCM slurry with phase change (solid/liquid cores)[135].

Therefore, the MPCM slurry possesses a large apparent specific heat, which includes the latent heat of the PCM core, near the PCM melting temperature. Moreover, this kind of PCM still has good fluidity, which enables itself to be transported through pipes by pumps. The convection caused by the motion of MPCM at the micro-level, the adopted metal case, and the particle-fluid/particle/wall interactions, could potentially enhance the heat transfer in MPCM slurry applications [135]. Thus, the MPCM slurry could be employed as the heat transfer fluid or the heat storage medium [137, 138]. Much research has been conducted on the thermos-mechanical characteristics of the MPCM slurry and its applications, however, the application on BTM using MPCM slurry was few.

2.6 Conclusion

EVs, HEVs, and FCEVs are regarded as an effective methodology to constrain the carbon footprint and reduce the environmental contamination. They require high power batteries, such as Li-ion, lead acid, and Ni-MH batteries. For those batteries to achieve high power, thermal management is an inevitable component to be improved for maintenance of both high efficiency cooling (or heating) and even temperature distribution. Four BTM systems have been introduced including air, liquid, PCM, and PEMFC BTMs. Their features, advantages and disadvantages are discussed.

In this PhD project, the PCM BTM for EVs and HEVs is focused. The advantage of this methodology is that PCMs have huge heat storage capacity, however with the drawback of low thermal conductivity. With the addition of high thermal conductivity materials, the composite PCMs can be created to have both high latent heat capacity and high thermal conductivity.

However, the traditional PCM application in BTM faces the challenges such as the leakage of melting PCM, the volume change during phace transition, and the low thermal conductivity of PCM.

To summarize, this PhD project mainly focuses on two type PCM for BTM in EVs and HEVs. One is the FSPCM, while the other is the MPCM slurry. These two special types of PCM could prevent the issue of PCM leakage, which is a normal problem during the phase transition. The FSPCM confined the phase transition of PCM within the porous matrix, while the MPCM slurry using a solid shell to cover the core PCM phase change. Moreover, the application of the porous matrix in FSPCM and the solid metal shell are expected to not only increase the stability of the PCM but also the thermal conductivity to enhance the heat transfer process. However, FSPCM and MPCM slurry were barely utilized in the BTM system at the current research stage. The experimental investigation combining FSPCM with conventional BTM system was conducted. The data was further used in the following model validation. The performance of them was predicted by the simulation in MATLAB (FSPCM), or by ANSYS (MPCM slurry).

Chapter 3. Numerical analysis of FSPCM BTM

3.1 Introduction

One of the most concerned parts for the widespread electric vehicles (EVs) is the thermal safety issue of the power batteries. Phase change materials (PCMs) has been extensively investigated in battery thermal management (BTM) systems. PCM will change its phase from solid to liquid when absorbing heat, thus the material muste be enclosed when is used in between the battery modules for cooling purpose. A promising methodology to stop or reduce the leakage is stabilizing the form of this energy storage material, the material is the so-called form stable PCM (FSPCM). In this chapter, a novel concept of using FSPCM for passive cooling battery system is proposed. The material is a composite combining paraffin (PA, as the PCM source), the high-density polyethylene (HDPE, as the composite matrix to avoid liquid leakage), and the expanded graphite (EG, as the composite matrix with relatively higher thermal conductivity). A numerical model of such BTM system using the proposed FSPCM and assisted by air cooling was built in the software of MATLAB. Four battery cooling scenarios were analyzed and compared, which includes the sensitivity analysis concerning the effects of FSPCM on the battery cooling performance. The parameters such as the thickness of FSPCM, the mass fraction of EG, and the velocity of the air were altered to discuss their different influences.

3.2 Methodology

3.2.1 FSPCM material

A commerical paraffin (PA) material, RT35HC, provided by Rubitherm®, was selected as PCM. This paraffin material has a proper melting point, which enables that the PCM could easily complete the phase transition processes from liquid to solid at the room temperature. Moreover, this paraffin material has a high heat storage capacity, which can absorb huge thermal energy during the battery working time. The main properties of this PCM are provided by the company as shown in Tab. 3.1.

Tab. 3.1 Main parameters of PCM (RT35HC) [139].

Parameters	Value
Melting temperature	34-36 °C
Heat storage capacity	240 $kJ \cdot kg^{-1}$
Specific heat capacity, $c_{p,\,PCM}$	2.0 $kJ \cdot kg^{-1} \cdot K^{-1}$
Density solid, $\rho_{PCM,\,S}$	0.88 $kg \cdot L^{-1}$
Density liquid, $\rho_{PCM,\,L}$	0.77 $kg \cdot L^{-1}$
Heat conductivity (both phase), λ_{PCM}	0.2 $W \cdot m^{-1} \cdot K^{-1}$
Volume expansion	12%
Flash point	177 °C

One matrix material, HDPE, was employed in this FSPCM as it has good compatibility with PA. Another matrix material, EG, was selected as the thermal conductivity enhancer. According to the experimental investigation in reference [30], it was found that the heat conductivity of such FSPCM can be enhanced by approximately 24%, given a mass fraction of EG to be 3%. The maximum weight percentage of the dispersed PA in the FSPCM could be as high as 77% to avoid the seepage of PCM [30], which indicated that the mass fraction of HDPE in the FSPCM should be larger than 23% otherwise the material leakage could take place [30]. Thus, the recommended mass fractions of three component for FSPCM, paraffin (PA), high density polyethylene (HDPE), and expanded graphite (EG) were 74.7% , 22.3% and 3%, respectively. The bulk density of the final production, composite FSPCM, was calculated by the experimentally measured weights and volumes in average, which is close to 1000 kg/m^3. Tab. 3.2 listed the essential properties used in the simulation study.

Tab. 3.2 Properties of the selected HDPE and EG.

Parameters	HDPE	EG
Thermal conductivity, λ_{HDPE}, λ_{EG}	0.45-0.52 $W \cdot m^{-1} \cdot K^{-1}$	3 $W \cdot m^{-1} \cdot K^{-1}$ [122]

Density, ρ_{HDPE}, ρ_{EG}	0.93-0.97 kg·L^{-1}	0.0035 kg·L^{-1} [122]
Specific heat capacity (kJ·kg^{-1}·K^{-1}), $c_{p,HDPE}$, $c_{p,EG}$	1.900	0.61

In a stable state (means no phase transition takes place), the specific heat capacity of the composite FSPCM could be calculated by the weight percentage, ω, of each component (separately denoted by the different subscripts) and their corresponding specific heat capacities, as expressed in Equation 3.1.

$$c_{p,com}=\omega_{HDPE}c_{p,HDPE}+\omega_{PCM}c_{p,PCM}+\omega_{EG}c_{p,EG} \quad 3.1$$

During phase change, for example, from the solid phase to the liquid phase, the effective specific heat capacity of this composite FSPCM could be calculated by a triangle model [140], as illustrated in Fig. 3.1. This is used to simplofy the simulation process by replacing the latent heat with effective specific heat capacity.

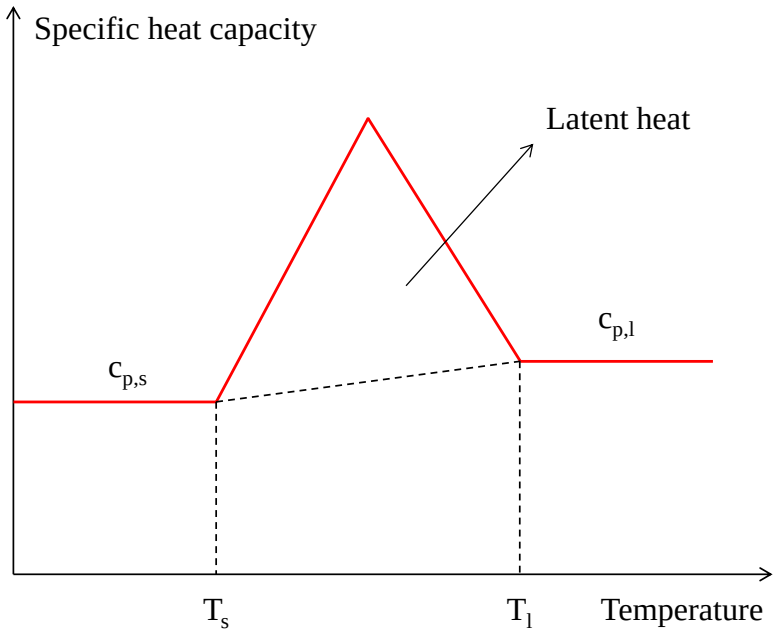

Fig. 3.1 The triangle model of calculating the effective specific capacity of the novel composite FSPCM [140].

The latent heat of PCM to undertake its phase change could be calculated as a triangle area shaped by the effective specific heat capacity (red lines) and the abscissa (black dashed line) within a pre-defined temperature range from T_s to T_l. T_s is the temperature that PCM starts its phase change from the solid to liquid state, while T_l is the temperature that PCM finishes its phase transition process and stay stable. Ma et al. [140] calculated $c_{p,PCM}$ by a triangle model as shown in Equation 3.2 and 3.3, where L_{PCM} represents the latent heat of PCM to change its state between solid and liquid. $c_{p,PCM,l}$ and $c_{p,PCM,s}$ are respectively the specific heat capacities of the composite PCM in the liquid and solid state.

$$c_{p,PCM}=(T-T_s)\left[\frac{c_{p,PCM,l}-c_{p,PCM,s}}{T_l-T_s}+\frac{4L_{PCM}}{(T_l-T_s)^2}\right]+c_{p,PCM,s} \qquad T_s\leq T\leq(T_s+T_l)/2 \qquad 3.2$$

$$c_{p,PCM}=(T_l-T)\left[\frac{4L_{PCM}}{(T_l-T_s)^2}-\frac{c_{p,PCM,l}-c_{p,PCM,s}}{T_l-T_s}\right]+c_{p,PCM,l} \qquad (T_s+T_l)/2\leq T\leq T_l \qquad 3.3$$

Equation 3.4 estimated the thermal conductivity of the composite FSPCM using the classic Maxwell-Eucken model [141, 142], where the subscripts e, c and d respectively represents the effective, the continuous phase (HDPE), and the dispersed phase (PA-EG). The heat conductivity of PA-EG was also calculated using this equation regarding EG as the continuous phase. ϕ denotes for the volume fraction of the dispersed phase.

$$\lambda_e=\lambda_c\left[\frac{\lambda_d+2\lambda_c+2\phi(\lambda_d-\lambda_c)}{\lambda_d+2\lambda_c-\phi(\lambda_d-\lambda_c)}\right] \qquad 3.4$$

By the calculation listed from Equation 3.1 to Equation 3.4, the essential characteristics of the novel composite FSPCM were obtained, as summarized in Tab. 3.3. These properties were treated as temperature independent as narrow temperature range was used in this study.

Tab. 3.3 Essential information of composite FSPCM.

Parameters	Bulk density	Specific heat	Thermal conductivity

Value	1000 kg·m^{-3}	Solid: 1614 J·kg^{-1}·K^{-1} Liquid: 1936 J·kg^{-1}·K^{-1}	0.26 W·m^{-1}·K^{-1}

3.2.2 Battery thermal management system

- **Battery information**

A commercialized prismatic $LiFeO_4$ cell was selected in this study as depicted in Fig. 3.2.a, with a height of 90 mm (y-axis), a thickness of 27 mm (x-axis), and a width of 70 mm (z-axis) [143]. Several cells in a same batch could be connected in series to compose the battery module, as the instance given in Fig. 3.2.b (the reference scenario).

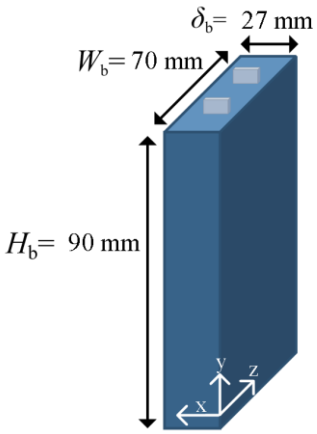

a. the selected prismatic cell

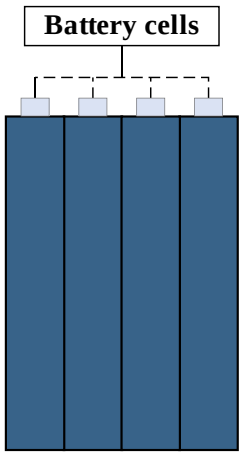

b. the formed battery module

Fig. 3.2 The selected prismatic cell and the formed battery module.

Essential information of a single prismatic $LiFeO_4$ cell used in the numerical model was listed in Tab.3.4.

Tab. 3.4 Parameters of a single prismatic $LiFeO_4$ cell.

Parameter	Value [a]
Specific heat capacity of cell, $c_{p,\,b}$	950 $J \cdot kg^{-1} \cdot K^{-1}$
Thermal conductivity of cell, λ_{cell}	2.6 $W \cdot m^{-1} \cdot K^{-1}$
Density of cell, ρ_{cell}	2335 $kg \cdot m^{-3}$
Rated capacity, C_r	12 Ah
Weight of one battery cell	0.4 kg
Temperature coefficient of voltage, dU/dT	0.00022 $V \cdot K^{-1}$

[a] The values were collected from the reference [143].

The internal resistance of the battery, R_{in}, is a function of the operational charging rate (also called C-rate, referred to the symbol of r_C). According to the reference [143], the battery internal resistance R_{in} used in this simulation was fitted by the experimental data as calculated in Equation. 3.5.

$$R_{in}(r_C) = 0.00705 - 0.01853 \times r_C + 0.05894 \times r_C^{\,2} - 0.009151 \times r_C^{\,3} + 0.06579 \times r_C^{\,4} - 0.01707 \times r_C^{\,5} \quad 3.5$$

C-rate could specify the operational condition using a relationship between the charging time, in which the battery could be theoretically fully charged (note that it is very hard to fully charge the battery in practical) and the rated battery capacity. The value of C-rate can be calculated by Equation. 3.6. For example, the rated capacity, C_r, of the selected Li-ion battery was 12 Ah, meaning that the battery could be fully charged under the operational current intensity of 12 A for an hour. In this circumstance, the C-rate is noted as 1C if the operational current intensity was given as 12 A, (the current density

during charging was I_C) and 2C means that the operational current was as high as doubled but running for a half hour. For an C-rate=nC, the battery will work with 12n A current intensity for 1/n hour. The rated capacity could support the battery to run to the end time t_C, as calculated in Equation 3.7.

$$r_C = I_C \cdot 1\ \text{h} / C_r \quad (3.6)$$

$$t_C = 1\ \text{h} / r_C \quad (3.7)$$

- **Scenarios setting**

In this chapter, four different scenarios of battery cooling conditions were considered, as illustrated in Fig. 3.3.

Case 1 - A battery system without cooling as a reference group. The batteries were packed in series rather than with any thermal management method, as illustrated in Fig. 3.3.a. Their yz-surfaces were stacked one by one.

Case 2 - A battery system with composite FSPCM (PA mixed with HDPE and EG). The battery stack was similar to Case 1 excluding that composite FSPCM was filled in between the battery cells yz-surfaces to provide the cooling effect to the battery package, as depicted in Fig. 3.3.b. The initial thickness ratio between the FSPCM and the battery cell, $r_{PCM\text{-}b}$, was 0.2. Later in this chapter, $r_{PCM\text{-}b}$ would be discussed from 0 to 1 to demonstrate its influence on the BTM performance.

Case 3 - A battery system with traditional forced air cooling. The packed battery module was cooled traditional forced air cooling rather than with the FSPCM as Case 2 did. The cooling air was forced to enter the battery module between the cells on the yz-plane, the same surface where PCM was placed in Case 2, to transfer the excess heat produced in the battery to the outside, as shown in Fig. 3.3.c. The initial ratio between the battery cell thickness (x-axis) and the air cooling gap (x-axis) was set to the same as in Case 2.

Case 4 - A battery system with both FSPCM and air cooling BTM. The space between battery cells yz-surfaces was filled with the FSPCM materials, similar to Case 2.

However, in the middle of FSPCM there was a path with the same thickness of the PCM for air cooling to take place, as displayed in Fig. 3.3.d.

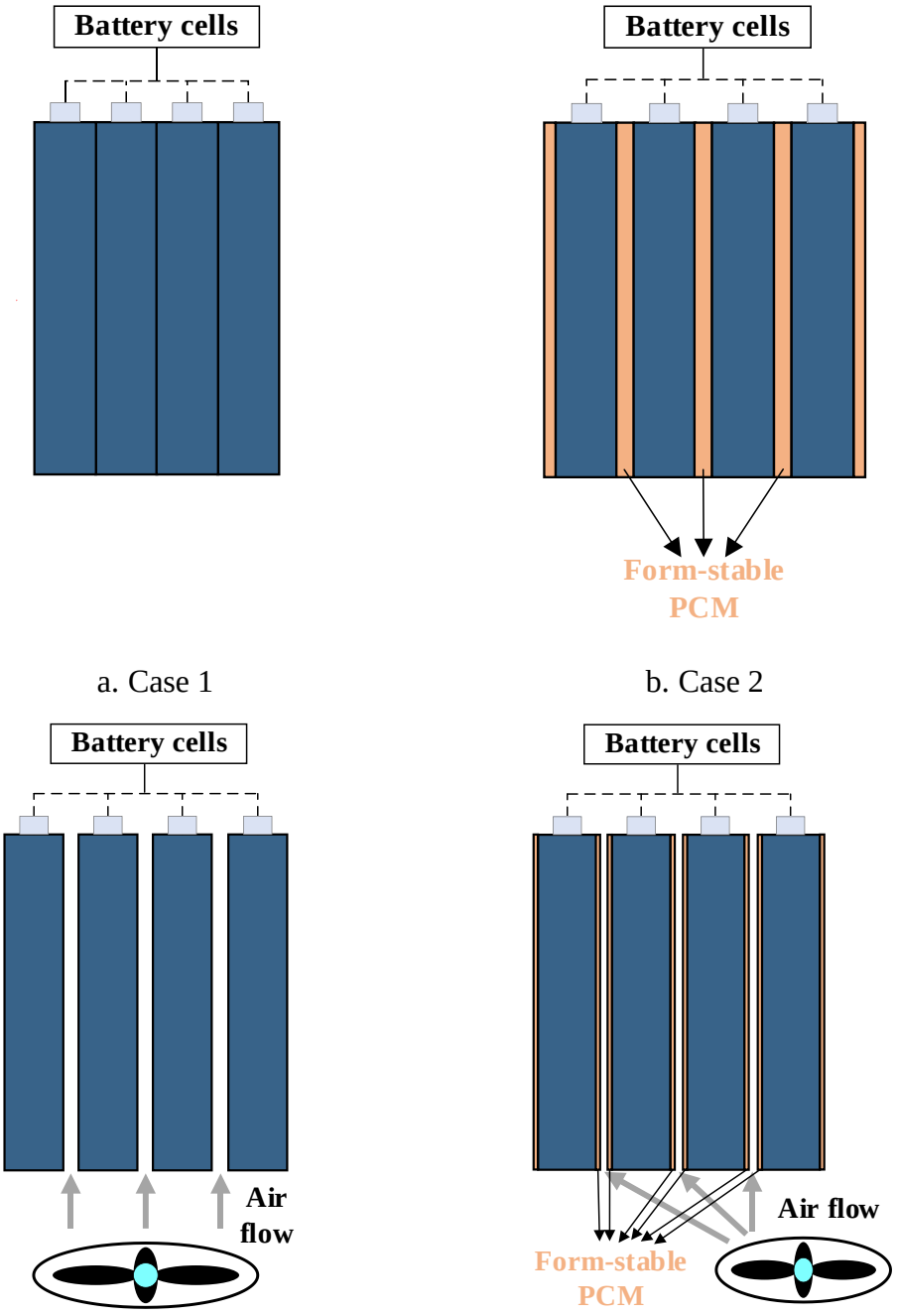

a. Case 1 b. Case 2

c. Case 3 d. Case 4

Fig. 3.3 Four different simulated scenarios.

3.2.3 Air convection

For the BTM with forced air cooling, the air convection could be calculated by Newton's law of cooling as Equation 3.8 [144], where the term $\dot{Q}_{conv}$ represents the convective heat transfer rate, and K_{air} denotes the convective heat transfer coefficient of the air. A is the surface area where the air passes through and exchange heat with the object. T_{ss} and T_{fs} are respectively the temperatures of the solid surface and the fluid surface.

$$\dot{Q}_{conv}=K_{air}A(T_{ss}-T_{fs}) \quad 3.8$$

The actual heat transfer coefficient could be influenced by the flow condition, laminar or turbulent, which can be decided by Reynolds number, *Re*, as expressed by Equation 3.9 [145], where u_∞ stands for the relative air velocity towards the object in the free stream condition and x is the distance of the flow position to the inlet air boundary (as signed in Fig. 3.4). μ means the dynamic viscosity of the air. A representative value, 5×10^5, decides the beginning of turbulence [ref], which means a higher *Re* represents that the turbulence takes place. It is assumed that the flow velocity of the air is zero at the surface of the object and that the highest velocity was found in the middle of the air path between the two battery panels, as displayed in Fig. 3.4. Therefore, the average air velocity could be calculated. When the air temperature is 300 K and the air flow velocity is 20 $m\cdot s^{-1}$ relative to the yz-plane of the cell, the critical location for the fluid condition transition from laminar to turbulence is 0.4 m, which is far longer than the length of cell (0.09 m). Thus, the convective heat transfer coefficient of the air in this study could be determined by the equation valid for the laminar condition.

$$Re=\frac{\rho u_\infty x}{\mu} \quad 3.9$$

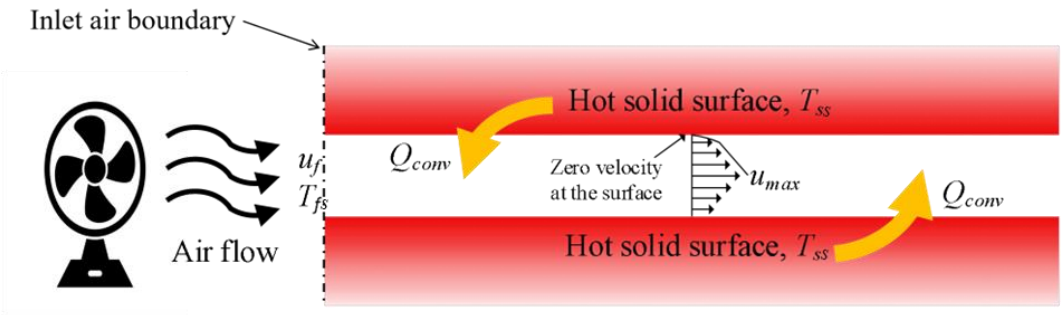

Fig. 3.4 Schematic diagram of the forced air convection, adapted from [146].

Nusselt number, *Nu*, describes the ratio of the convective heat transfer to the conductive heat transfer within the fluid, as expressed in Equation 3.10 [145], where l is the characteristic length (the height of the battery, H_b, in this case). K represents the convective heat transfer coefficient, while λ_f is the thermal conductivity of the fluid.

$$Nu = \frac{Kl}{\lambda_f} \tag{3.10}$$

The average *Nu* for the laminar flow over the entire object surface could be calculated as an universal function of *Re* and Prandtl number, *Pr*, [146], shown in Equation 3.11, where *Pr* is 0.707 for 300 K air. Pr is defined as the ratio of momentum diffusivity to the thermal diffusivity. When the air temperature is 300 K and it is at the atmospheric pressure, ρ, μ, and λ of the air are 1.1614 kg·m^{-3}, 184.6×10^{-7} N·s·m^{-2}, and 26.3×10^{-3} W·m^{-1}·K^{-1}, respectively [145].

$$Nu = 0.664 Re_l^{1/2} Pr^{1/3} \quad Pr \geq 0.6 \tag{3.11}$$

As a summary, the convective heat transfer coefficient of the air could be simplified as shown in Equation 3.12.

$$K_{\text{air}} = 13u^{1/2} \tag{3.12}$$

In this study, the inlet air flow velocity was varied from 1 to 20 $m \cdot s^{-1}$, in which range the flow condition can be kept in the laminar state. The convective heat transfer coefficient of the air could therefore be calculated based on Equation 3.12. This convective heat transfer coefficient could be further used for estimating the impact of the air flow velocity on the battery cooling performance.

3.2.4 Modelling

- **Governing equations**

A heat transfer model was developed based on the aforementioned equations and reference[13]. The MATLAB was used for the coding process. The heat conduction between the FSPCM and battery was treated as a one-dimensional heat condution (in x-axis), as displayed in Fig. 3.5, considering the symmetric shape of the BTM system.

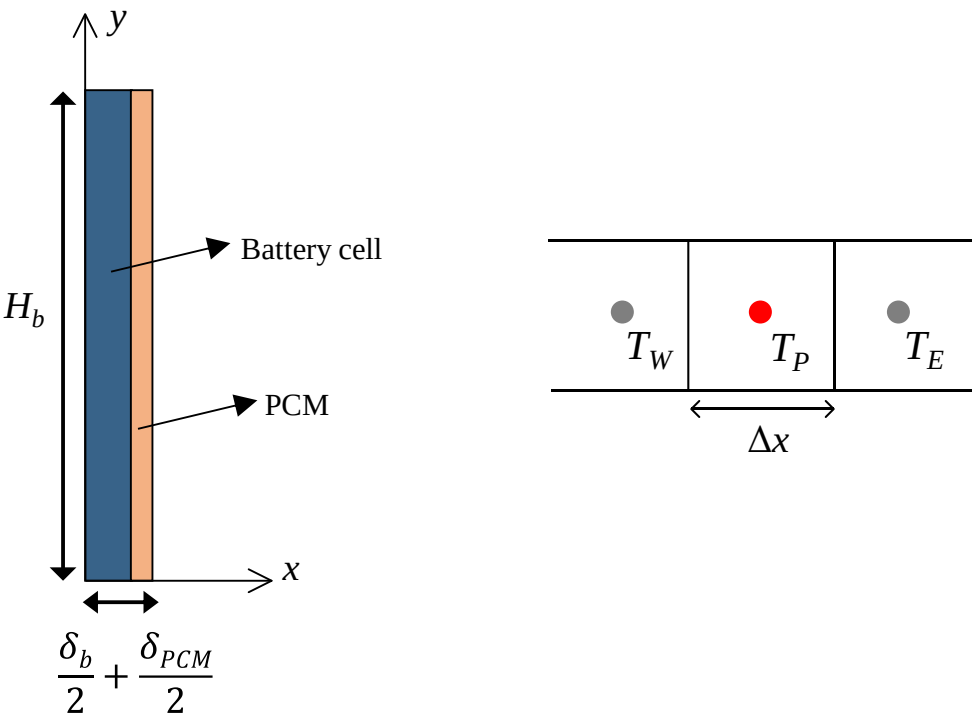

a. symmetric one-dimensional model b. temperature distribution around the calculated point

Fig. 3.5 Physical model of the BTM system with the composite FSPCM.

The composite FSPCM covers on the battery surface, and therefore they have a same surface area (H_b x W_b) in yz-plane. The thickness of PCM is δ_{PCM}. Equation 3.13 stands for this heat transfer process, where $\dot{q}_b$ is the generated heat by the battery with the unit of $W \cdot m^{-3}$. The latent heat of the composite FSPCM was not considered in Equation 3.13, as it would be treated as the effective specific heat capacity.

$$\rho c_p \frac{\partial T}{\partial t} = \frac{\partial}{\partial x}\left(\lambda \frac{\partial T}{\partial x}\right) + \dot{q}_b \qquad 3.13$$

The initial condition ($t = 0$) of this heat conduction process could be expressed as shown in Equation 3.14, where T_{amb} represents the ambient temperature.

$$T|_{t=0} = T_{amb} \qquad 3.14$$

Regarding of the symmetry of these two near cells, Equation 3.15 expressed the boundary condition of a single battery cell in four cases, and it also stands for the boundary condition of the composite FSPCM in Case 2.

$$\left.\frac{\partial T}{\partial x}\right|_{x=0, x=\frac{\delta_b}{2}+\frac{\delta_{PCM}}{2}} = 0 \qquad 3.15$$

The boundary condition with forced air cooling in Case 3 and Case 4 was formulated in Equation 3.16.

$$-\lambda \left.\frac{\partial T}{\partial x}\right|_{x=\frac{\delta_b}{2}, x=\frac{\delta_b}{2}+\frac{\delta_{PCM}}{2}} = K_{air}(T - T_{amb}) \qquad 3.16$$

The control volume method was employed to convert above differential equations into the algebraic form, which was then solved by the implicit method as resulted in

Equation 3.17, where λ_{EP} and λ_{WP} are the corresponding thermal conductivity in the area confined by the temperatures of T_E to T_P and T_W to T_P, respectively, as drawn in Fig. 3.5.b. The subscript E, P, and W relatively stands for the position at the east of the calculated point, the calculated point, and the west of the calculated point.

$$\Delta x \rho c_p \frac{T_P - T_{P,0}}{\Delta t} = \lambda_{EP} \frac{T_E - T_P}{\Delta x} + \lambda_{WP} \frac{T_W - T_P}{\Delta x} + \Delta x \dot{q} \qquad 3.17$$

- **Heat generation with validation**

The heat generated by the Li-ion battery cells is assumed to be spatially uniform for the simplicity of simulation. Equation 3.18 expressed the heat generation by the battery, excluding the mixing and phase change enthalpies [147], where I is the battery operational current. U and V are respectively the open circuit voltage and the actual voltage of the cell. The first term on the left $I(U-V)$ stands for the heat generated by the inner resistance, while the second term $IT\frac{dU}{dt}$ represents the heat influenced by the temperature dependent battery voltage (in the electrochemical aspect). This equation does not considered the complex reaction in the cell.

$$\dot{Q}_{b,\,gen} = I(U-V) + IT\frac{dU}{dt} \qquad 3.18$$

Equation 3.19 is a variant of Equation 3.18 [143], where the term I^2R_{in} represents the Joule heat generated by the battery internal resistance.

$$\dot{Q}_{b,\,gen} = I^2 R_{in} + IT\frac{dU}{dt} \qquad 3.19$$

The volumetric heat generation rate of the packed battery can be calculated by Equation 3.20, where $V_{ol,b}$ is the battery volume. As listed in Tab 3.4, $\frac{dU}{dt}$ is 0.00022 $V \cdot K^{-1}$.

$$\dot{q}_{\mathrm{b}}=\frac{I^2R_{\mathrm{in}}+IT\dfrac{\mathrm{d}U}{\mathrm{d}t}}{V_{\mathrm{ol,b}}} \tag{3.20}$$

The heat generation model was validated by the experimental results retrieved from reference [143], where the used parameters were listed in Tab 3.4 and the validated results were displayed in Fig. 3.6. The ambient temperature, T_{amb}, was set to 298.15 K. In this validation, C-rate was set to 5C.

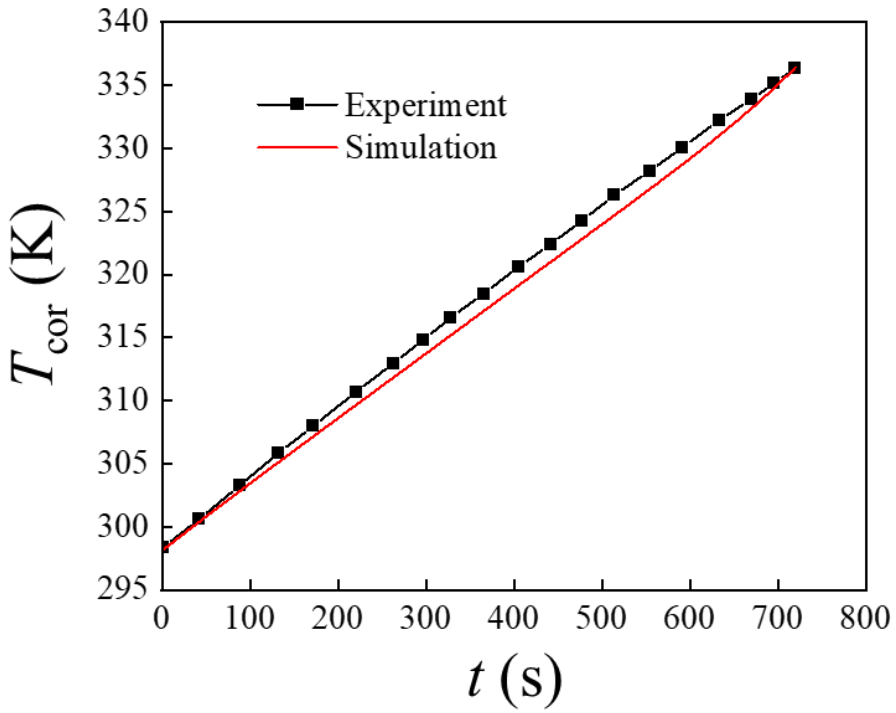

Fig. 3.6 The validation of battery heat generation model with experimental data.

The results showed that the simulated results in this study were in satisfied agreement with the experimental data retrieved from the reference. Only minor deviations were found between the two curves, probably attributing to the one-dimensional model which ignores the heat transfer in other directions. It was demonstrated that this battery heat generation model can predict the thermal performance of the battery well, and it would be reliable to be used in the subsequent BTM investigations. The value of the errors between the experiment and simulation is displayed in Appendix. D for reference.

3.2.5 Investigation procedures

The investigation procedures of this chapter were stated as following:

- Comparing the cooling performance of different scenarios

Four different scenarios were designed for the investigation, as stated in Section 3.2.2

- Comparing the cooling performance of the EG mass fraction

The thermal conductivity of the composite FSPCM is also a critical characteristic that needs to be discussed to improve the BTM performance. The composite FSPCM in this study was prepared by adding expanded graphite (EG) into the mixture of paraffin (PA) and high density polyethylene (HDPE) to enhance the thermal conductivity of the HDPE-PA mixture. Fig. 3.7 reported that the thermal conductivity of the composite FSPCM [125] with the increase of EG percentage from 0.0 wt% to 4.6 wt% increased from 0.31 $W \cdot m^{-1} \cdot K^{-1}$ to 1.36 $W \cdot m^{-1} \cdot K^{-1}$. These values were subsequently used by the one-dimensional model to discuss the cooling performance influenced by the EG mass fraction. In this analysis, $r_{PCM\text{-}b}$ was set to be 0.2.

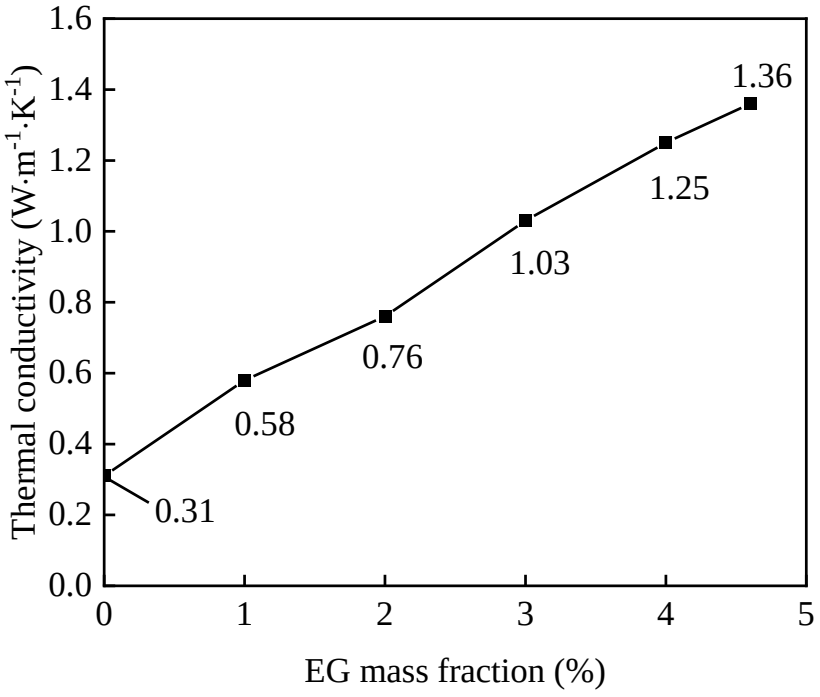

Fig. 3.7 Thermal conductivity of the composite FSPCM with increased EG mass fraction (data adopted from [125]).

- Comparing the cooling performance of the PCM thickness

The ratio between the PCM thickness and battery thickness, $r_{PCM\text{-}b}$, was altered within 0-0.8 to study the influence of PCM thickness using the scenario of Case 2.

- Comparing the cooling performance of the air flow velocity

The air flow velocity from 1 $m \cdot s^{-1}$ to 20 $m \cdot s^{-1}$ was tested in the simulation (Case 3) to investigate its impact on the cooling performance.

3.3 Results and discussion

3.3.1 Different scenarios

The influence of the employing different BTM configurations on the battery cooling performance was discussed in this section from Fig. 3.8 to Fig. 3.10, setting the C-rate to 5C, 3C, and 1C. The maximum temperature in the battery pakage, T_{cor}, also called as the cell core temperature, were used as the performance indicator for the comparison. The end time, t_C, was determined by the simulated C-rate as shown in Equation 3.7, which means that the end time, t_C, was 1/5 h = 12 min = 720 s when C-rate was 5C, as given in the definition. The end time, t_C, was 1/3 h = 20 min = 1200 s or 1/1 h = 60 min = 3600 s if C-rate was 3C or 1C. In Case 3 and 4, the convective heat transfer coefficient of the air convection was 41.1 $W \cdot m^{-2} \cdot K^{-1}$ with the air velocity of 10 $m \cdot s^{-1}$. It is obvious that a higher C-rate could lead to a higher core temperature of the battery (T_{cor}). Without any cooling, as in Case 1, the highest T_{cor} appearred at every end of the black curves. They were 339.6 K (66.45 °C), 326.1 K (52.95 °C), 312.5 K (39.35 °C) for 5C, 3C, 1C, respectively.

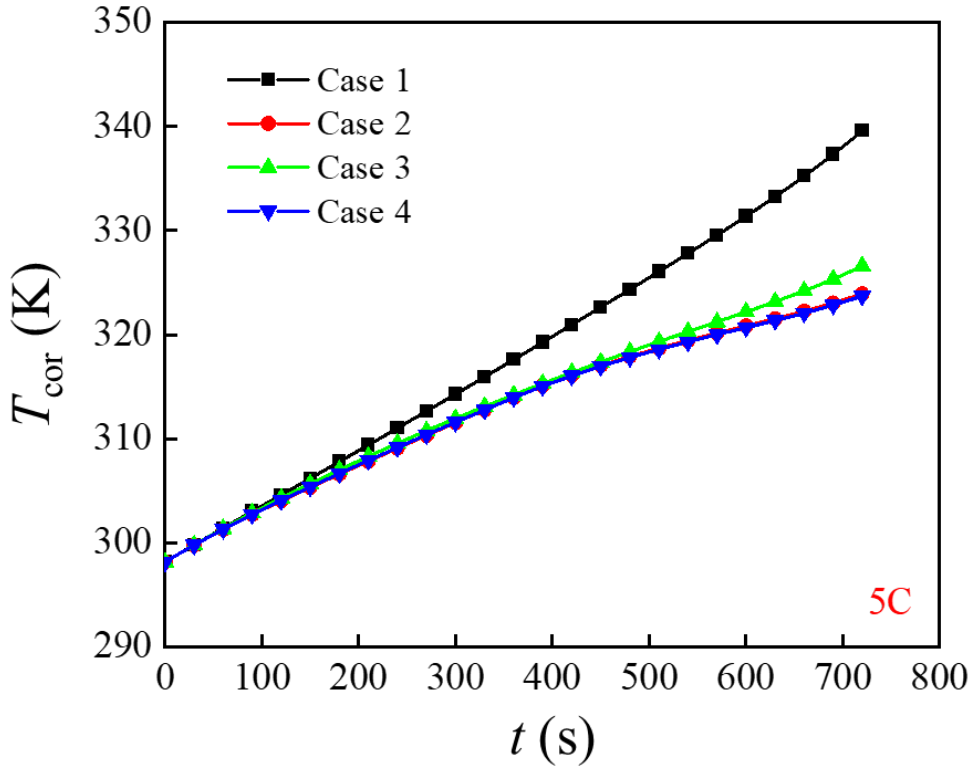

Fig. 3.8 Core battery temperature profile of Case 1-4 using C-rate of 5C.

Fig. 3.8 was the result of Case 1-4 when C-rate was set to 5C. The T_{cor} of Case 2-4 were 323.9 K, 326.5 K, and 323.7 K at the end of the simulation (720 s), separately. Between the time of 400 s to 500 s, a plateau was found in the curve for Case 2 and 4, which indicated that the PCM reached its melting temperature and started its phase change process absorbing relative more heat from the battery. In compassion with the simulation where no cooling was employed (Case 1), the corresponding temperature drops were 15.7 K, 13.1 K, 15.9 K, respectively for Case 2, 3 and 4. It indicated that, in Case 4, the coupled air-PCM cooling method achieved the maximum temperature drop and proved itself to be the optimal BTM among the candidates, while Case 2 has very close cooling performance at such high battery charge / discharge rate.

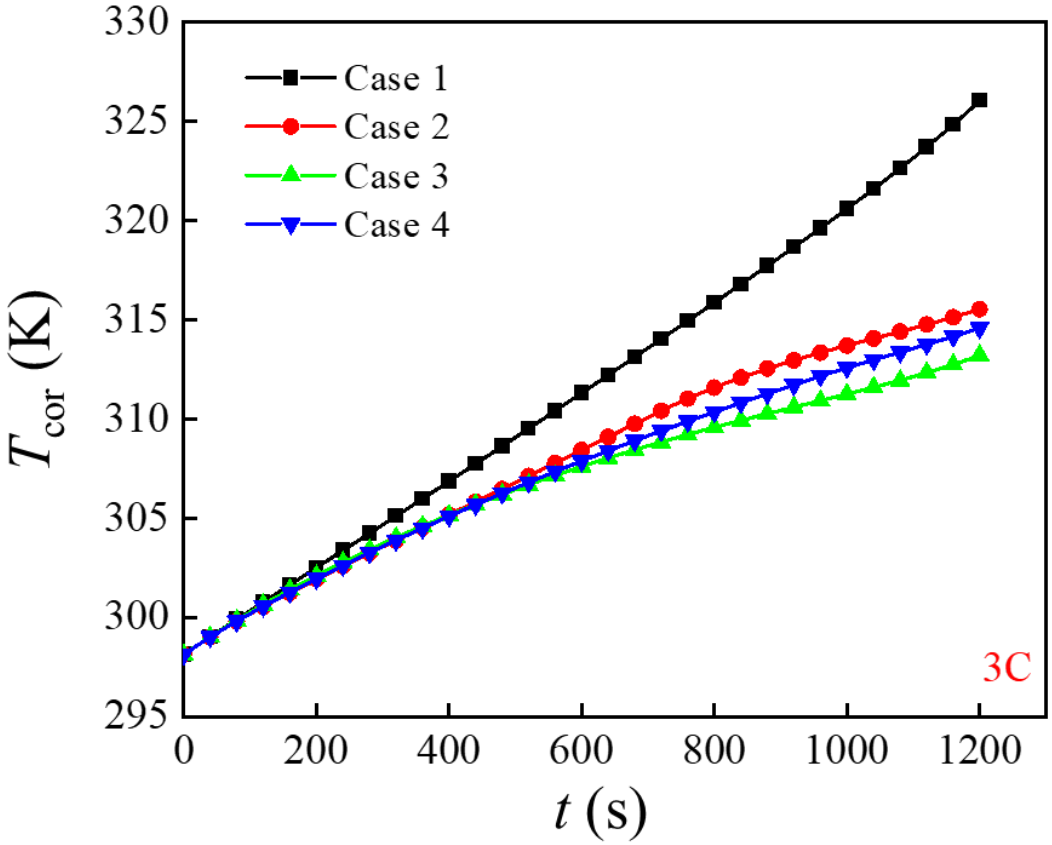

Fig. 3.9 Core battery temperature profile of Case 1-4 using C-rate of 3C.

Fig. 3.9 displayed the result of Case 1-4 when C-rate was set to 3C. At this smaller C-rate, it was found that the forced air cooling BTM considerably reduced the core battery temperature. T_{cor} at the t_C (1200 s) were 315.5 K, 313.2 K, and 314.6 K for Case 2, 3, and 4, respectively. Interestingly, the best cooling performance (lowest T_{cor}) was found to be in Case 3, its difference with Case 1 was 12.8 K, larger than that in Case 2, 10.51 K and Case 4, 12.4 K. It was because that in the 3C cycle, the temperature of the battery did not achieve the high enough temperature to efficiently melt the composite FSPCM.

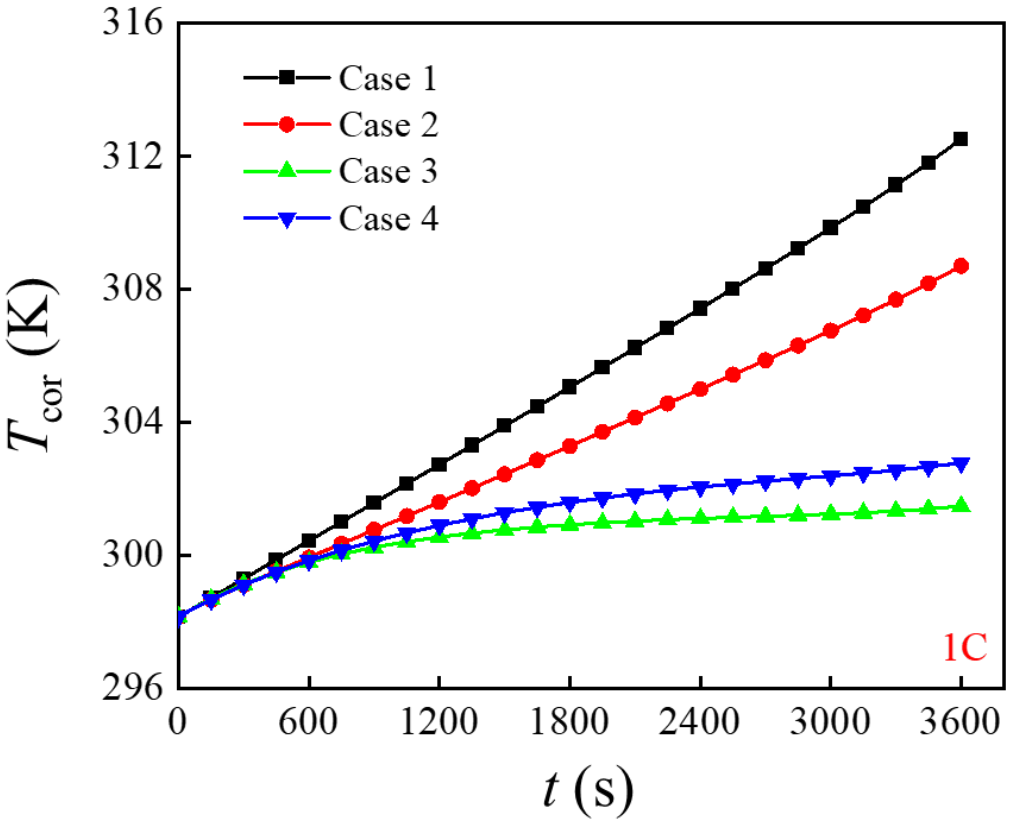

Fig. 3.10 Core battery temperature profile of Case 1-4 using C-rate of 3C.

Fig. 3.10 exhibited the simulated T_{cor} results when C-rate was 1C. Similarly, air cooling BTM (Case 3) at this low C-rate (1C) proved itself to be the best among the studied cases followed by the combined methodology (Case 4) of air cooling and passive FSPCM BTM. At t_C, 3600 s, T_{cor} of Case 3 (green curve) obtained the maximum temperature difference, 11.0 K, with the one without any BTM (Case 1). Although in Case 2, the FSPCM BTM showed the large gap between the cooling effect of itself and other two cases, the essential performance indicator, T_{cor}, was still controlled within a satisfied temperature range, here T_{cor} at the end of charge / discharge process is only 308.7 K (35.5 °C). At t_C, the melting of PCM was not yet occurred as no obvious reduced T_{cor} increment rate was found during this period.

As a summary, due to the fixed melting temperature of PCM, the passive cooling of FSPCM is highly dependent on the battery charge / discharge rate and performs better at higher battery charge / discharge rate since more melting heat is used. Although forced air cooling and hybrid air-FSPCM cooling BTM generally have better cooling

effect than the FSPCM BTM in the case with a lower C-rate (3C and 1C), considering the system simplicity and for a higher C-rate, FSPCM BTM could be a better choice.

3.3.2 Effects of the EG mass fraction

Case 2 and Case 4 were respectively studied in this section as shown in Fig. 3.11 and Fig. 3.12, where the PCM was integrated without (Case 2) and with air cooling (Case 4). In this section, effects of EG mass fraction of the composite FSPCM are analysed.

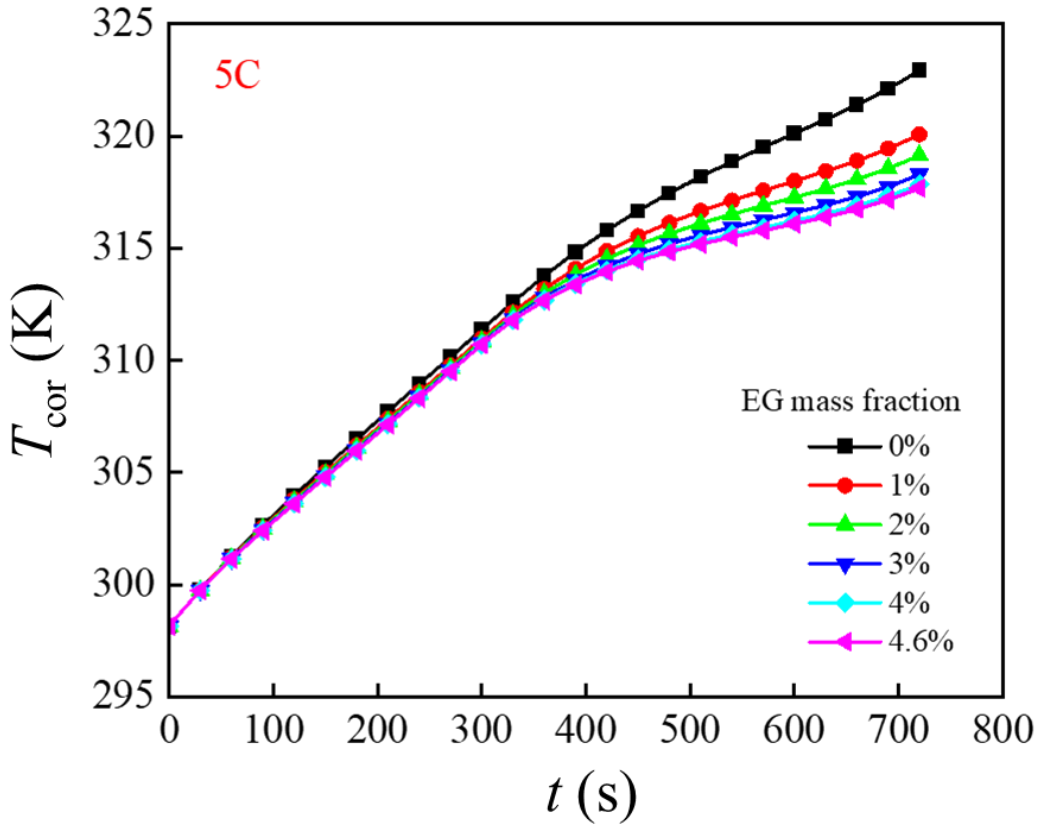

Fig. 3.11 T_{cor} of Case 2 versus time with various EG mass fractions (0.0 wt% to 4.6 wt%).

As shown in Fig. 3.11, T_{cor} of cases with different EG mass fractions exhibited similarly before the time around 300 s, and the linear increment indicated that the composite FSPCM was at the initial state - the solid phase. After that time, the non-linear temperature increment indicated the battery cooling come into the next stage - phase transition from the solid to liquid phase. From then, the divergence between these temperature curves using different EG mass fractions was noticed. With higher EG

mass fraction, the increase rate of T_{cor} was observed to be reduced, as the more EG percentage in the FSPCM could lead to a higher thermal conductivity of the final composite material used in the BTM, therefore better heat transfer and cooling energy can be released for battery cooling more quickly. With the EG mass fraction to be 4.6 wt%, T_{cor} at t_C was 317.7 K, 5.2 K lower than 322.9 K (without any EG additives).

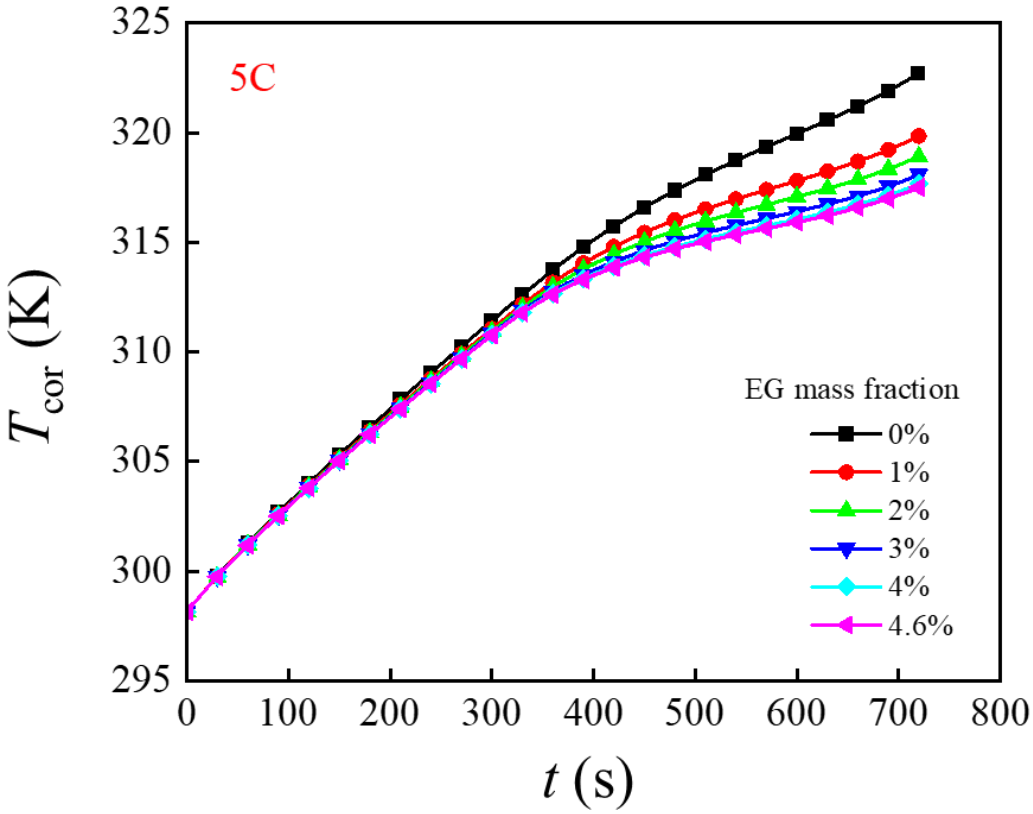

Fig. 3.12 T_{cor} of Case 4 versus time with various EG mass fractions (0.0 wt% to 4.6 wt%).

Fig. 3.12 displayed the simulated results of Case 4 using various EG mass fractions from 0.0 wt% to 4.6 wt% when C-rate was 5C. The results showed a similar shape with the results in Fig. 3.11. With the increasing EG mass fraction, the increase rate of T_{cor} was observed to be reduced. With the EG mass fraction to be 4.6 wt%, T_{cor} at t_C was 317.6 K, 5.3 K lower than 322.9 K (without any EG additives).

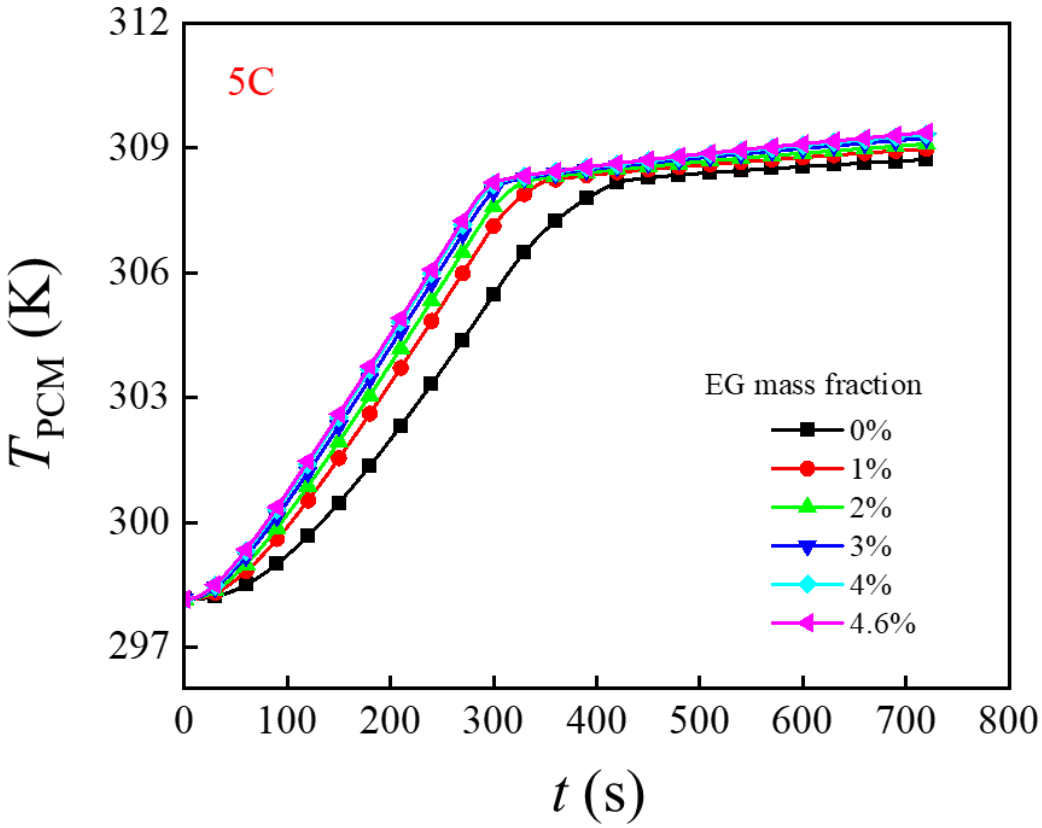

Fig. 3.13 T_{PCM} of Case 2 versus time with various EG mass fractions (0.0 wt% to 4.6 wt%).

Fig. 3.13 presented the PCM temperature, T_{PCM}, of Case 2 introducing different proportions of EG when C-rate was 5C. As the geomtry of the FSPCM was designed to be symmetric, the temperature at the centre point of the FSPCM represents T_{PCM}. It was observed that lower EG mass fraction decelerated the temperature increment of the composite FSPCM, and thus the phase transition plateau was found to come later. Higher EG mass fraction leads to larger thermal conductivity and better heat conduction, then higher cooling power can be obtained which is preferred by BTM system.

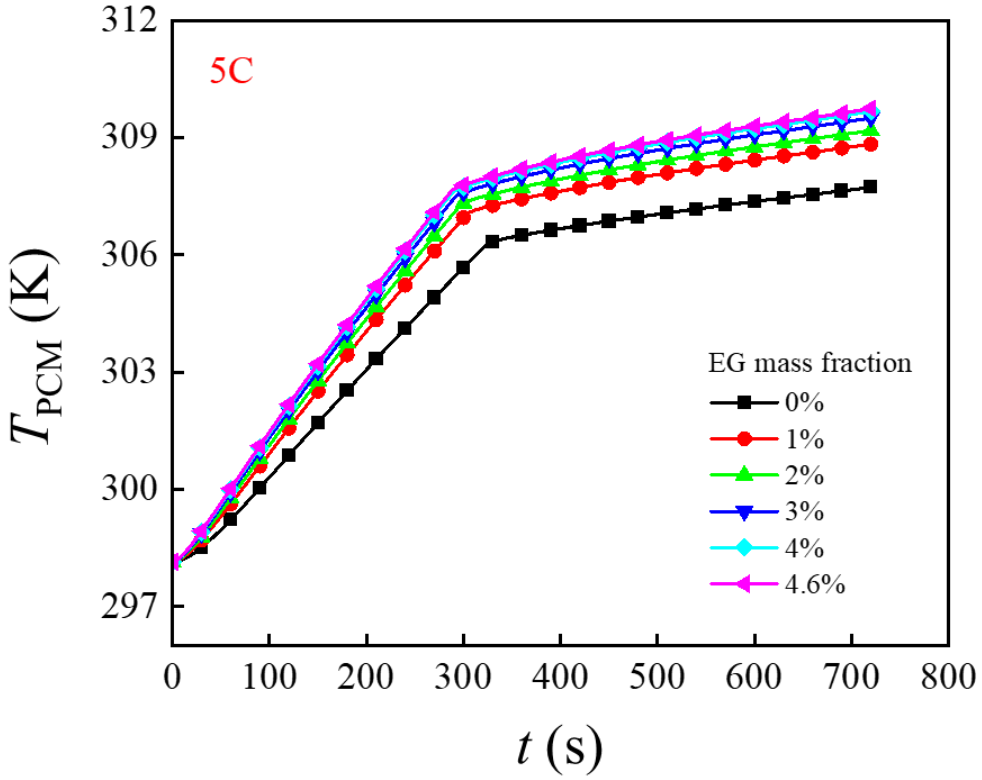

Fig. 3.14 T_{PCM} of Case 4 versus time with various EG mass fractions (0.0 wt% to 4.6 wt%).

Fig. 3.14 presented the PCM temperature of Case 4, where the mass fractions of EG varied from 0.0 wt% to 4.6 wt%, given C-rate was 5C. Similar shape was found in the figure, compared to Fig. 3.13, however Fig. 3.14 presented even larger gap between each curve at the plateau stage. With the assistance of forced air cooling, T_{PCM} at t_C reached up to 309.8 K, given an EG mass fraction of 4.6 wt%, which was 0.4 K higher than that in Case 2 (without forced air cooling).

3.3.3 Influence of the PCM thickness

In Section 3.3.1, it was demonstrated that the FSPCM BTM had impressive cooling performance under various operational conditions. In this section, the PCM thickness was further investigated aiming to enhance the cooling performance of the FSPCM BTM. Here Case 2 was studied.

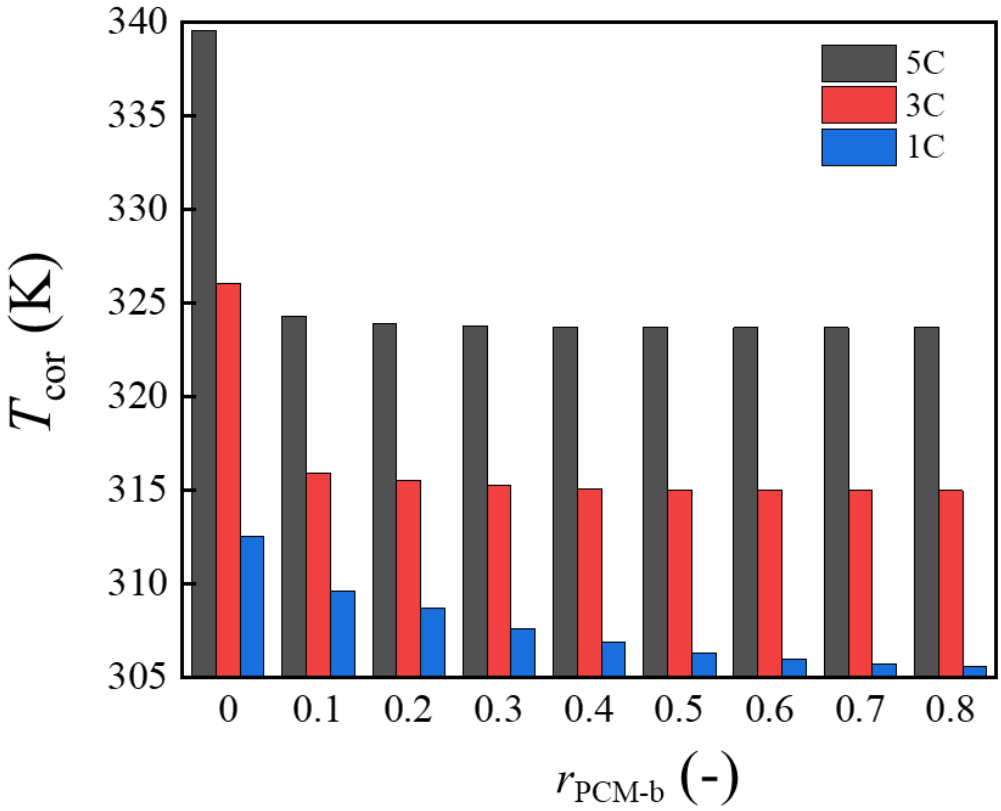

Fig. 3.15 T_{cor} at t_C of Case 2 versus r_{PCM-b} of 0-0.8 (r_C=1,3,5C).

Fig. 3.15 exhibited the variation of the core battery temperature, T_{cor}, at the r_C-dependent end time, t_C, versus the alteration of the FSPCM thickness. The thickness ratio between the FSPCM and the battery cell, r_{PCM-b}, ranged from 0 to 0.8. It was demonstrated that an obvious drop of T_{cor} was found between the condition when r_{PCM-b} was 0 and 0.1. Moreover, higher thickness ratio (means that the thicker FSPCM) had very limited improved battery cooling performance, due to the fixed melting temperature range of the selected PCM. The simulated battery packs could be cooled down (compared to Case 1) with a temperature drop limited to approximately 16 K, 11 K, and 7 K by PCM, when C-rate was 5C, 3C, and 1C, respectively, as the melting temperature range of the FSPCM was 307-309 K. For 1C condition, the battery heat power was not high enough to rise the FSPCM temperature to the melting temperature range, so that there was no phase change and no latent heat was involved in battery cooling, which explains the decreasing T_{cor} as increasing FSPCM thickness at 1C condition.

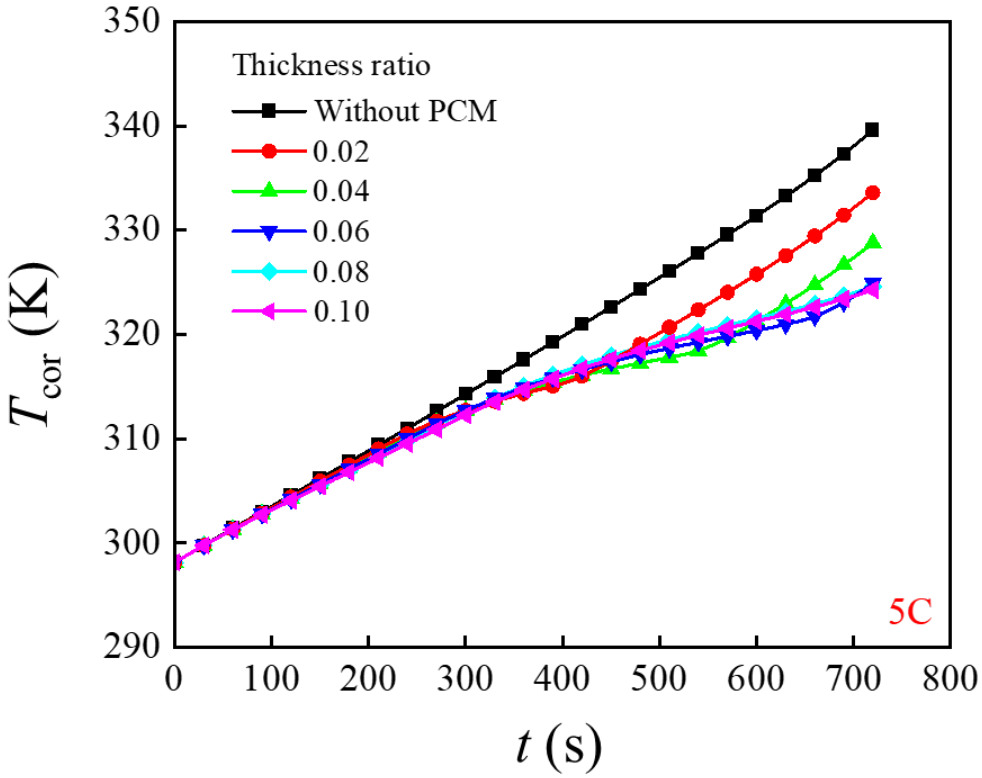

Fig. 3.16 T_{cor} of Case 2 versus $r_{PCM\text{-}b}$=0-0.1 (r_C=5C).

Fig. 3.16 displayed the simulated results of T_{cor} evolution of Case 2 with time when $r_{PCM\text{-}b}$ was altered from 0 to 0.1 and C-rate was set to 5C. An obvious plateau was found in each curve except the black one ($r_{PCM\text{-}b}$=0). During this plateau period, the phase change process of the FSPCM was under progress, while after the plateau, the quicker increment of T_{cor} indicated that the melting process was completed. The length of the plateau reflected the time for the battery heat to heat the FSPCM until the material was fully melted without any piece remaining in solid state. It meant that the thinner PCM it was, the less battery-generated heat can be absorbed by the FSPCM, and thus the relatively poorer cooling performance it could result in. Comparably, even though the thickest FSPCM literally reached the lowest T_{cor} at t_C, FSPCM BTM with $r_{PCM\text{-}b}$ ranging from 0.06 to 0.10 had very similar T_{cor} at t_C in this circumstance. Comprehensively considering the capital cost of the FSPCM BTM or the size of that system, 0.06 could be the competitive candidate among all.

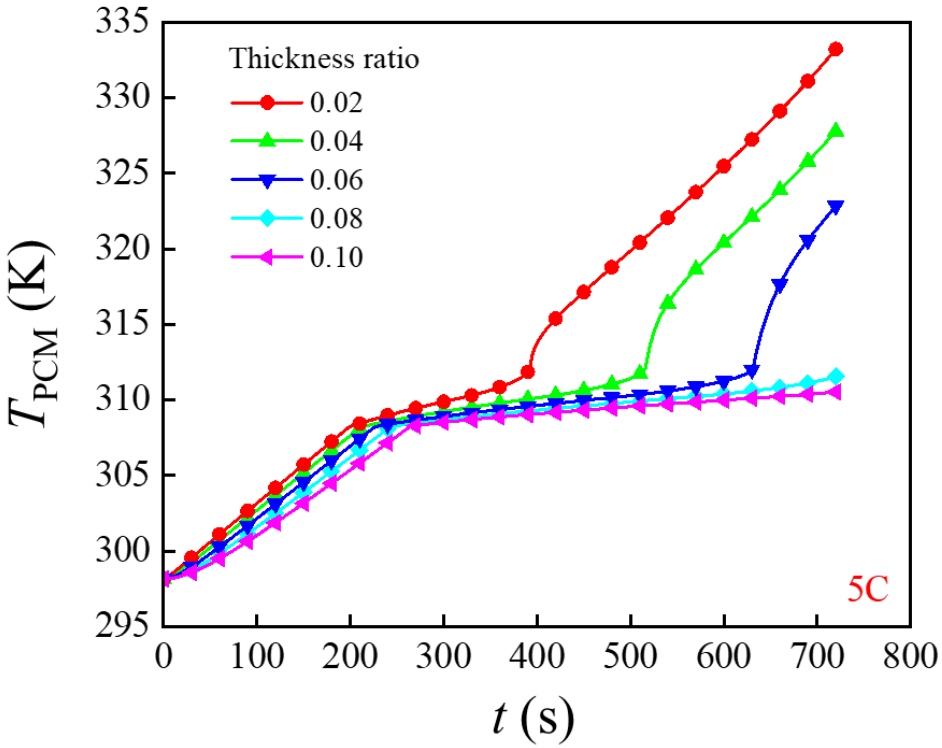

Fig. 3.17 T_{PCM} of Case 2 versus $r_{PCM\text{-}b}$=0.02-0.1 (r_C=5C).

Fig. 3.17 displayed the temperature of PCM, T_{PCM}, developing with time when $r_{PCM\text{-}b}$ was altered from 0 to 0.1 and C-rate was set to 5C. A more obvious plateau was found in each curve, as it represented the melting process of the FSPCM. With the from-stable PCM to be thicker, the time length of the plateau increased, indicating more battery-generated heat was absorbed by the FSPCM. The swift increment like a tail at the end of the curves standing for $r_{PCM\text{-}b}$=0.02, 0.04 and 0.06 demonstrated that the battery-generated heat had fully melt the FSPCM, while $r_{PCM\text{-}b}$=0.08 could be enough for the cooling mission of this selected battery pack. The phase change plateau was completed at 388 s, 510 s, and 630 s corresponding to $r_{PCM\text{-}b}$=0.02, 0.04 and 0.06, respectively. With $r_{PCM\text{-}b}$=0.08 and 0.10, T_{cor} was maintained within the melting temperature range. Again, comprehensively considering the capital cost, the size, and the safety of the FSPCM BTM, $r_{PCM\text{-}b}$=0.08 could be the optimal selection compared with $r_{PCM\text{-}b}$=0.06 determined by battery temperature (not enough heat capacity to hold the battery-generated heat).

3.3.4 Influence of the air flow velocity

The influence of the varied air flow velocities (1 $m \cdot s^{-1}$ to 20 $m \cdot s^{-1}$) on the BTM performance of Case 3 was studied in this section as illustrated in Fig. 3.18. The corresponding heat transfer coefficient of the air ranged from 13.0 $W \cdot m^{-2} \cdot K^{-1}$ to 58 $W \cdot m^{-2} \cdot K^{-1}$ according to Equation 3.12. The increasing rate of T_{cor} was reduced by increased air flow velocity when the BTM was with forced air cooling only. At t_C, T_{cor} reached 334.4 K when air flow velocity was 1 $m \cdot s^{-1}$, and it could be declined by 11.1 K using the air flow velocity of 20 $m \cdot s^{-1}$. In comparison with the result of Case 2, only the BTM with the air flow velocity of 20 $m \cdot s^{-1}$ could achieve the better cooling performance than the BTM with the composite FSPCM.

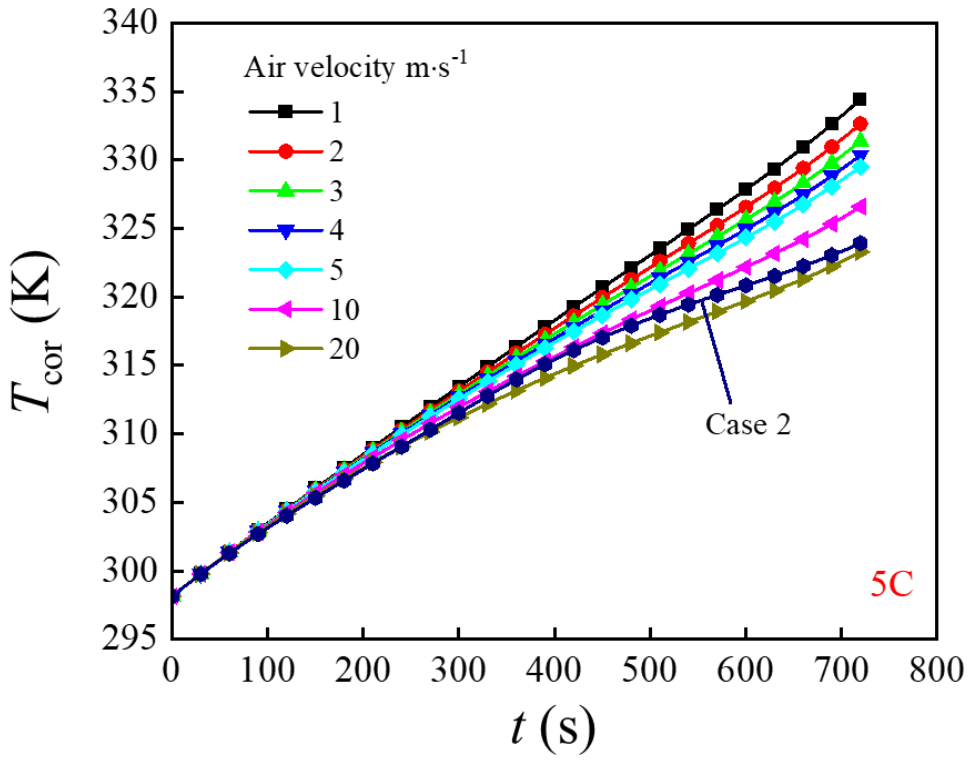

Fig. 3.18 T_{cor} of Case 4 versus time with various air flow velocities (1-20 $m \cdot s^{-1}$).

As a conclusion, at high and medium C-rate, the composite FSPCM could be more suitable for BTM, as high air flow velocity could not visibly enhance the battery cooling performance and it required more space, energy, cost, and higher construction strength for the system.

3.4 Conclusion

A composite FSPCM composed by paraffin (PA), expanded graphite (EG), and high density polyethylene (HDPE) was employed in this chapter to evaluate its effects on BTM performance. A one-dimensional numerical model was developed to comprehensively analyse and compare different BTMs and different operational conditions. Conclusions are summarized as follows:

- Coupled PCM and air cooling had the optimal BTM performance at r_C=5C, resulting 15.9 K temperature drop of T_{cor} at t_C (comparing to case 1), followed by 15.7 K reduction with the help of FSPCM only. Forced air cooling achieves better thermal management performance than PCM when battery discharges at 3C and 1C.
- EG added into PCM can improve the thermal conductivity of the composite material. When mass fraction of EG increases from 0% to 4.6%, the maximum temperature of battery is reduced from 322.9 K to 317.7 K at 5C discharge rate.
- FSPCM has superior battery cooling performance, however, thicker PCM has not visible improvement for battery cooling. Moreover, PCM with thickness ratio less than 0.08 occurs complete melting before absorbing all the heat generated from battery since thinner PCM has not enough heat carrier capacity. Acceptable thermal management performance has been found for the PCM with thickness ratio larger than 0.08.
- Based on four BTM configurations and sensitive analyses, suitable BTM choices for the EV/HEV should depend on the actual discharge rate, PCM thickness, EG mass fraction, and air velocity, thereby reducing dissipation of PCM and complex structure.

The results showed that FSPCM presents promising potential for battery thermal management. Configuration of integrating FSPCM with forced air convection can maximally prevent heat accumulation of battery, achieving 15.9 K temperature reduction. FSPCMs with thickness ratio of 0.08 and 4.6 wt% EG was considered to have the optimal thermal management performance. Faster air velocity has more obvious effect on battery cooling when battery discharges at lower rate.

Chapter 4. Experimental study on MPCM BTM

4.1 Introduction

In Chapter. 3, the simulation of FSPCM BTM showed that it was feasible to employ FSPCM along with other cooling technologies (such as forced air-cooling) in the BTM system. Besides of using FSPCM for passive cooling, MPCM, another kind of enhanced PCM technology, can be used for fluid BTM system, taking the advantage of large cold energy carrier capacity of MPCM slurry comparing to water or air, as the MPCM slurry could be produced by mixing water with the source MPCM particle. In this chapter, the BTM performance was experimentally investigated by either circulating the MPCM slurry or water through the lab-designed battery cooling module.

4.2 Methodology

4.2.1 MPCM slurry

MPCM32D was the MPCM source material used in the battery cooling experiment, which was commercially provided by CAVU Group. The MPCM slurry was made by dispersing raw MPCM powders into water. The MPCM particle consisted of a polymeric melamine - formaldehyde (MF) resin shell wrapping the core of paraffin (melting point within 30 °C to 32 °C). According to the certificate of analysis provided by CAVU Group, the corresponding thermal-physical characteristics were listed in Tab. 4.1. Claimed by the provider, this MPCM has a solid content of approximately 97%, and it was characterized to be highly stable in the designed testing battery temperature range of 15 °C – 80 °C. Additionally, the polymeric MF resin capsule had a good mechanical strength which could resist general damages to prove the safety of the material and system.

Tab. 4.1 Properties of MPCM32D [148].

Characteristic [Unit]	Test value	Specification

Melting area [°C]	31	30-34
Heat of fusion [kJ/kg]	164	Report only
Free wax [%]	0.5	<=2.5
Mean particle size [μm]	20.7	15.0-30.0
Solids content [%]	97.4	97.0-100.0
Free formaldehyde	Pass	0-500

The MPCM slurry were prepared with the mass ratios of 10%, ω_s, in the distilled and deionized water. The mixture were mechanically mixed by a stir machine for several hours. Fig. 4.1 illustrated the specific heat capacity of the manufactured 10 wt% MPCM slurry, $c_{p,MPCMs}$, which was calculated based on the specific heat capacity of the MPCM source, $c_{p,MPCM}$, as shown in Equation 4.1, where ω_{water} and $c_{p,water}$ respectively represented the mass ratio and the specific heat of the distilled water. The specific heat capacity of source MPCM particle was measured in the lab.

$$c_{p,MPCMs}=\omega_s c_{p,MPCM}+\omega_{water} c_{p,water} \quad 4.1$$

In Fig. 4.1, each curve had one peak at approximately 37 °C, indicating that at around this temperature the selected MPCM could had its phase change and maximum heat storage capacity. It meant that the huges amount of heat is needed to increase the MPCM temperature and thus the optimal performance for the cooling capacity. At the right root of the peak, it represented the end of the melting process in the MPCM at around 40 °C. Thus, as a summary, from the aspect of the specific heat, the suitable working temperature for the cooling effect should be within about 25 °C to 40 °C.

The thermal conductivity of the prepared MPCM slurry could be retrieved by the classic Maxwell-Eucken model, as denoted in Equation 3.4, where then the subscript c, d, and

e separately represented the continuous phase (water), the dispersed phase (MPCM particle), and the prepared MPCM slurry.

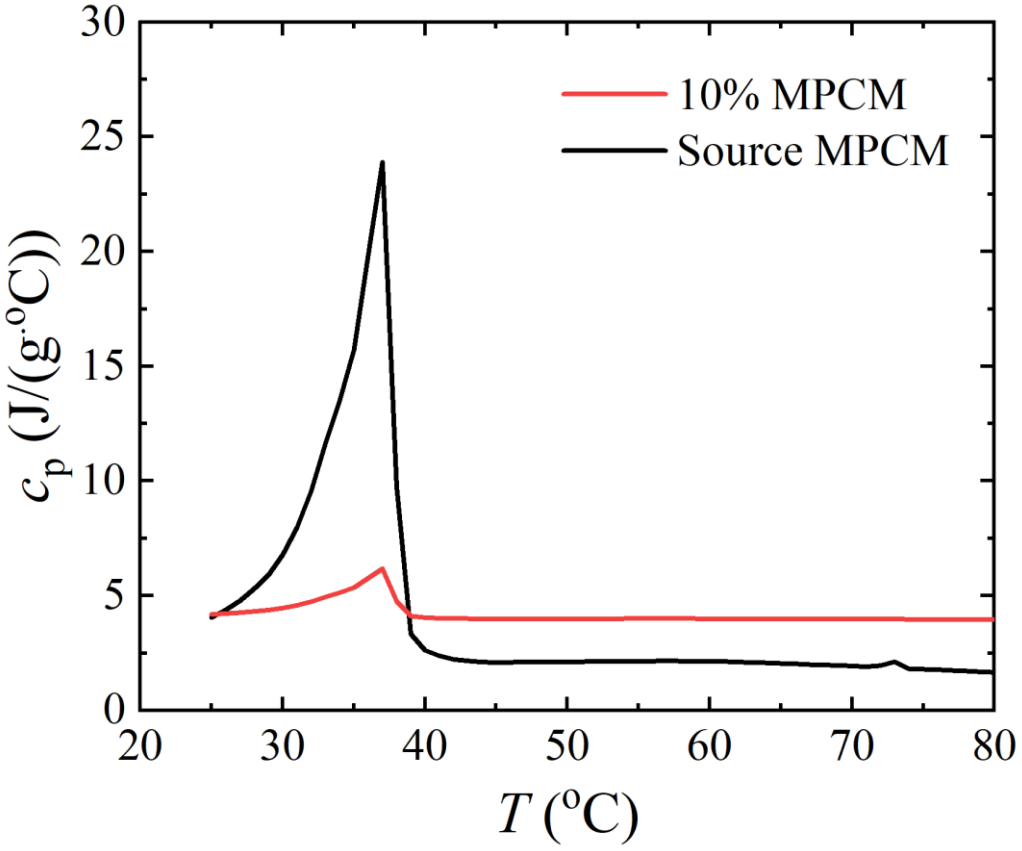

Fig. 4.1 Specific heat capacity of the original MPCM source and the prepared 10 wt% MPCM slurry.

The manufactured MPCM slurry is still able to flow in pipes but was thicker than water. It thus flowed slower than water given the same pump power. Nevertheless, the cold carry capacity of MPCM slurry is higher than water at the same pumping power, as clearly shown in Fig. 4.2. As shown in the figure, the gross cooling effect produced by water (in purple) was at the lowest position in the figure, which demonstrating the minimum cooling production compared to other candidates made of MPCM. The increment in pump power (per meter) referred to the enlarged flow rate, which could lead to the increase of the cooling power produced by either the MPCM slurry or the water. Given a pump power, P, smaller than 0.02 kW, the maximum cooling effect was produced by the MPCM slurry made with a ω_s of 12%, while the pump supplied a power higher than 0.02 kW, the maximum cold power was provided by the MPCM

slurry with a ω_s of 15%. When the slurry mass fraction is higher then 12%, the enlarged slurry viscosity leads to much higher pumping power, indicating that using higher slurry concentration is not economic though its cooling carring capacity is higher.

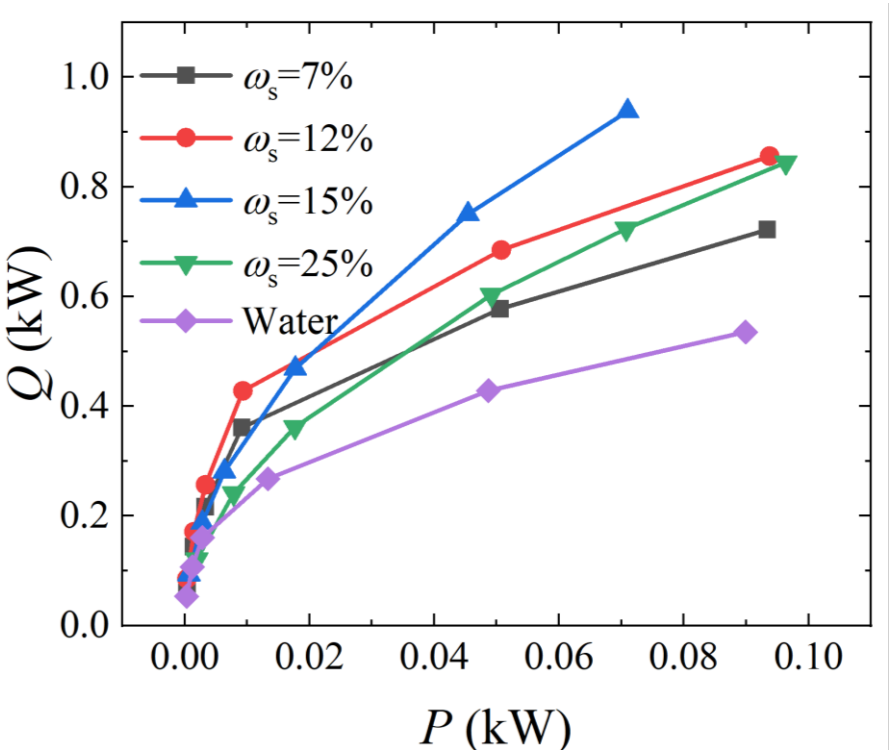

Fig. 4.2 Pumping power vs. cooling power, with a flow distance of 1 m.

Equation 4.2 was used to determine the pumping power of MPCM slurry and water [149, 150], where D is the diameter of the pipe. Δp and Δx represent the differential pressure (between coolant inlet and outlet) and the pipe length, respectively. ρ is the density of the coolant. $\bar{u}$ stands for the average viscosity of the cooling medium.

$$f = \left(\frac{D\Delta p}{\Delta x}\right)/(2\rho\bar{u}^2) \qquad 4.2$$

f is Fanning flow friction, an Δp calculation indicator, which could be calculated by Equation 4.3 [149, 150]. Re is the Renolds number, the used equation and slurry properties are from Ref [150]

$$\begin{cases} f = \dfrac{16}{Re}, Re < 2300 \\ f = \dfrac{0.0791}{Re^{0.25}}, Re \geq 2300 \end{cases} \quad 4.3$$

4.2.2 Experimental set-up

The experimental test rig was designed and established to simulate the process of battery cooling, as the configuration of the BTM was illustrated in Fig. 4.3.

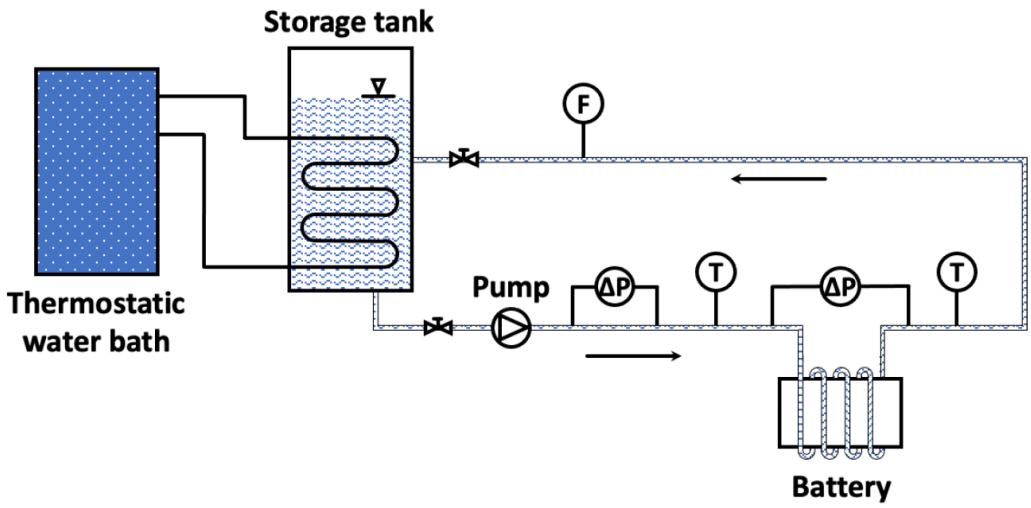

Fig. 4.3 Schematic diagram of the BTM system configuration

At the left of Fig. 4.3, the thermostatic water bath takes control of the storage tank temperature, which hold the cooling media for the battery (either the manufactured 10 wt% MPCM slurry or water). The cooling media (either the manufactured 10 wt%

MPCM slurry or water) is pumped through the battery cooling plate in the copper pipes. During the charging or discharging of the battery, heat is generated by the battery package and conducted to the attached cooling plate. When the cooling media flowing through the battery cooling plate, the heat conducted to the cooling basement (aluminum component) is transferred to the employed coolant. The thermal energy generated by the battery pack is therefore partly removed by the coolant. The inlet and outlet temperature of the cooling media through the battery cooling plate is monitored to analyse the thermal management performance of using typical coolants. The outlet cooling media with an increased temperature then flows back into the storage tank to fullfill the circulating BTM system. The cooling media is cooled in the storage tank under the temperature control of the connected water bath.

Fig. 4.4 was the photo of the practical experimental test rig. The components of the electricity source, thermostatic water bath, storage tank, pump, battery heat source, battery cooling module and various sensors were connected as displayed. It should be noted that the flow meter was mounted under the table so it was only pointed to show the position rather than to show the practical device.

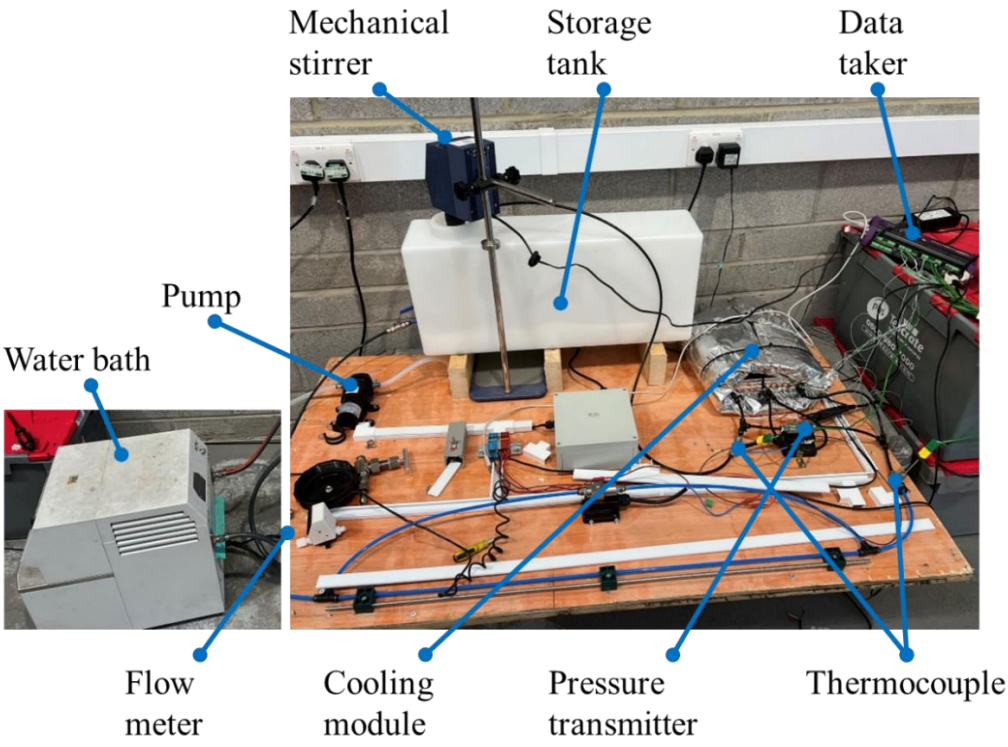

Fig. 4.4 Photo of the BTM system.

Fig. 4.5 displayed the photo of the simulated EV battery heat source. Due to the health and safety regulation, as well as the more cost-effective way to conduct the experiment, the EV battery was substituted by a plate heat source. It was not a real battery but an electric heater in a metal shell, with the gaps between cells filled by silicon pastes. The simulated battery heat source was designed to have the same size with a Nissan Leaf battery, as the information of the battery was given in Tab. 4.2. The electricity source used in this project was the directly provied electricy charger on the lab wall, which was 240 V alternating current. A transformer (Model No. TDGC-2KVA) was used to alternate the electricity voltage on the electric heater.

Tab. 4.2 Information table of a Nissan Leaf battery [151].

Characteristics	Specification
Number of cells	4
Construction	2 parallel 2 series
Battery length	303 mm
Battery width	223 mm
Battery thickness	35 mm
Battery weight	3.8 kg
Cell type	Laminate type
Cathode material	LiMn2O4 with LiNiO2
Anode material	Graphite
Rated capacity (0.3C)	33.1 Ah
Average voltage	3.8 V
Cell length	290 mm
Cell width	216 mm
Cell thickness	7.1 mm
Cell weight	799 g

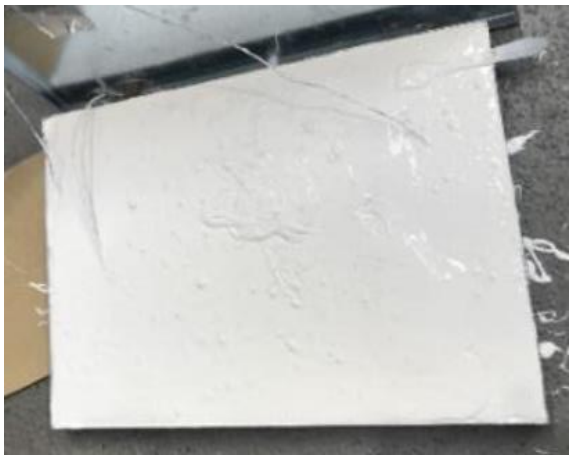

Fig. 4.5 Photo of the battery heat source covered by the silicon paste.

Fig. 4.6 showed a photo of the main battery cooling module in the BTM experiment. The cooling plate was composed by the copper pipe (orange) and the solid aluminum (silver). The cooling module employed two cooling plates, also called as cooling basement, in total. They lies in parallel to form a cooling module. In next chapter, this aluminum part will be substituted by the FSPCM basement (researched in Chapter 3), to further investigate the battery cooling performance integrating FSPCM with MPCM slurry technologies. The copper pipe had an inner diameter of 8 mm and outer diameter of 10 mm. The main body of the cooling module (two parallel Al-basements) excluding the bended and inlet/outlet parts of the cooper pipe out of the aluminum cube had a same size with the battery heat source plate.

Fig. 4.6 Photo of the battery cooling module.

Fig. 4.7 showed the wrapped battery heat source with the adhered cooling module. The cooling module was packed with the simulated battery heat source in the way of vertical stack. Between them, silicon paste was used as thermal-conductive glue. The outside of the battery with the cooling module was the insulation material, which was employed to avoid heat dissipation to the ambient. The two cooling plates were connected in series using the soft black pipe. The thermocouple and the pressure transmitter were pointed out in the photo. The pressure difference between the inlet and outlet cooling fluid was recorded, as well as the temperature. Besides, several thermocouples were placed inside the wrapped body to monitor the battery heat source and the cooling module temperature. It should be noted that a thermocouple located in the layer between the battery and cooling module (at the centre in this layer) provided the core battery temperature. Even though it was not directly detected temperature in the physical centre of the battery, it still reflected the useful thermal information of the core battery as that the inner heat source could not be destroyed.

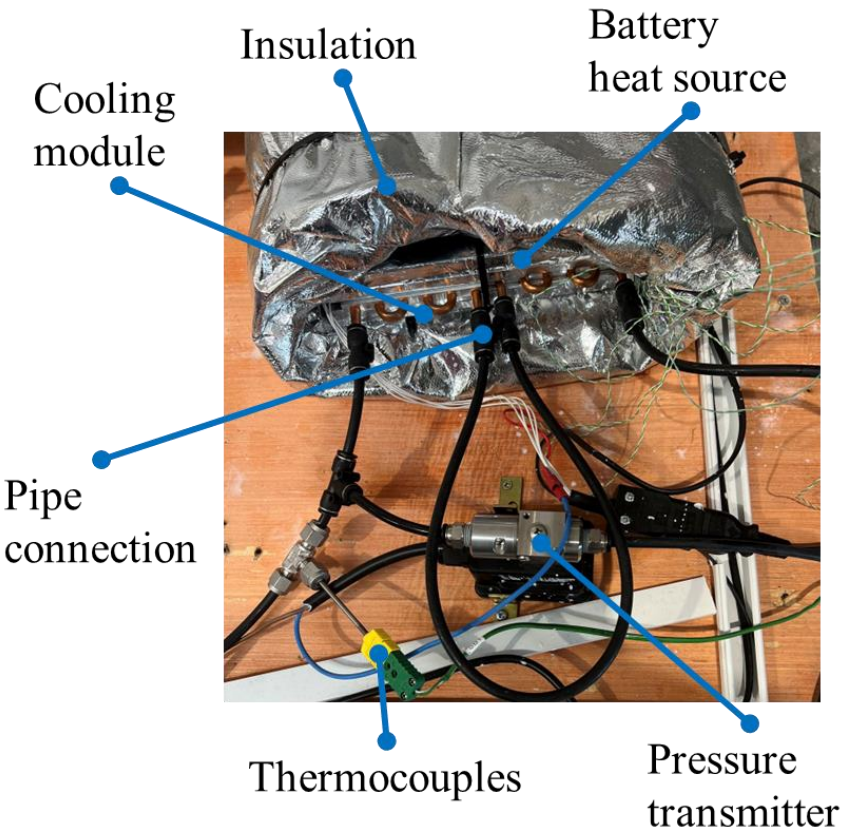

Fig. 4.7 The wrapped battery heat source with the battery cooling module.

Several sensors were utilized to retrieve the data and monitor the cooling progress, including the differential pressure sensor, thermocouple, and flow meter. The measured data of the pressure difference, temperature and the flow rate of the circulating fluid were analyzed for the flow-heat correlations.

Tab. 4.3 Information of the flow meter [152].

Characteristic	Specification
Device name	RS PRO flow meter, 0.05 – 10 L/min

Device photo	
Device size	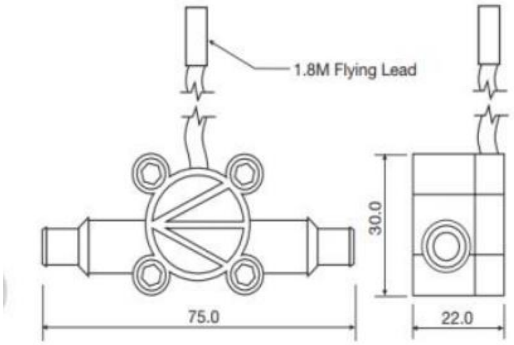
Flow rate	0.05 L/min – 10 L/min
Material	Body and cap – PVDF, ‘O’ Ring seal - Viton®, Magnets - Over-moulded, Bearings – Sapphire
Repeatability	0.1%
Display	Electronic display
For use with	Oil & water
Supply voltage	4.5 V to 24 V dc
Current rating	8 mA
Output	Stream of NPN/PNP pulses
Electrical connection	cable
Pipe diameter range	8 mm
Minimum operating temperature	-25 °C
Maximum operating temperature	125 °C

Tab 4.3 displayed the information of the flow meter [152]. The flow meter was provided by the company of RS COMPONENTS LTD. The mini turbine flowmeter was claimed to have high performance as the totally non-metallic wetted components enables itself to meter aggressive chemicals including ultra-pure water. The bearings were made of sapphire, which could support the device for a long duty life and high reliability.

Tab. 4.4 Information of the water pump [153].

Characteristic	Specification
Device name	RS PRO, 12 V 380 mbar Direct Coupling Centrifugal Water Pump, 1150ml/min
Device photo	
Device size	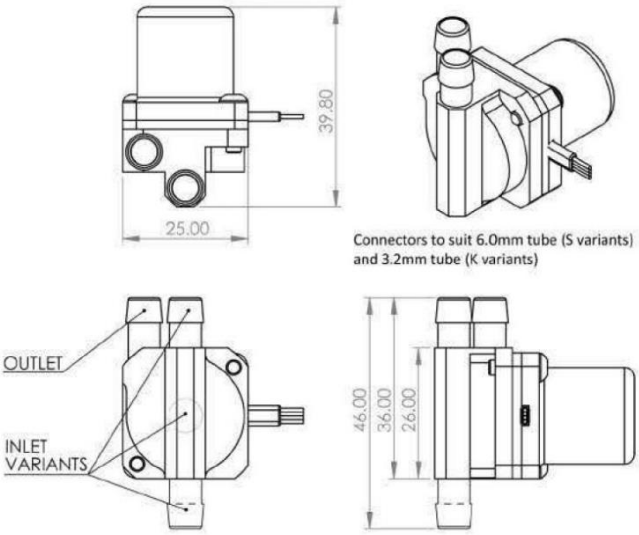
Weight	24g - 32g
Flow rate	Up to 2600 mL/min
Operating temperature	-20 °C – 100 °C
Power supply	Solar supply, PSU or batteries
Noise level	<3 dB
Other features	Brushless drive motor and integral controller CNC aluminium alloy construction Wide range of chemical resistance

Tab 4.4 presented the information of the pump utilized in the experimental investigation [153]. The M400 pump was driven by a brushless drive motor and had a built-in electronic controller. It was constructed from precision CNC machined aluminum alloy with stainless steel tubing connectors. It was fitted with Viton seals as standard. For the resistance of other chemicals and solvents, alternative seal materials and wetted part coatings were also available. The pump included a feedback wire, which can be used optionally to measure pump output.

Tab. 4.5 Information of the pressure transmitter [154]

Characteristic	Specification
Device name	Omega pressure transmitter PX2300-2DI
Device photo	
Device dimensions: mm(inch)	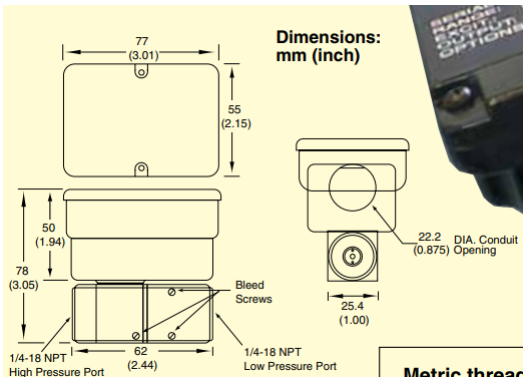
Pressure range	0 psi – 2 psi
Excitation	24 Vdc nominal
Accuracy Value	0.25
Input Resistance	0 to 1000 Ω
Operating temperature range	-18 to 80°C (0 to 176°F)
Compensation temperature range	-1 to 65°C (30 to 149°F)
Maximum line pressure	250 psig

Maximum overpressure	High Side: 1 to 5 psi = 20 x FS, 10 to 25 psi = 10 x FS, 50 psi = 5 x FS, 100 psi = 2.5 x FS Low Side: 2.5 x FS (shift recoverable)
Accuracy	±0.25% RSS FS at constant temperature (includes linearity, repeatability, and hysteresis)
Repeatability	±0.05% FS
Wetted Materials	Air and fluids compatible with 17-4 and 300 stainless steel, FKM, and silicone O-rings
Response time	50 ms (water)
Weight	410g (14.4 oz)
Output signal	Current
Electrical output	4 mA – 20 mA

Tab 4.5 listed the information of the OMEGA's PX2300 differential pressure transducers, which were compatible with a large range of media, from dry air to corrosive liquids [154]. All wetted parts of the pressure transmitter were either stainless steel or elastomer seals. It could work in harsh industrial environments due to a high working pressure and high overpressure ratings.

These carefully selected experimental devices could consequently enable the compatible test rig required by the different cooling fluids of water (relatively lower viscosity) and MPCM slurry (relatively higher viscosity).

4.2.3 Test procedures and conditions

The MPCM slurry flowed out from the storage tank at the temperature controlled by the thermostatic water bath. It should be noted that the thermostatic water bath was firstly heated to a slightly higher temperature than that in the ambient, so that the warmer MPCM slurry could smoothly flow. The extra heating process could improve the liquidity of the prepared MPCM slurry. Otherwise, under the low ambient temperature in UK, especially in winter, the experimental investigation could be

stopped as the MPCM slurry could be obstructed in the pipe and the container. It was then pumped through the cooling plate to exchange heat with the EV battery heat source.

The electric heater core in the EV battery heat source maintained the constant rate of the increased battery temperature (in a way just like how it should be in the real battery with the given rated capacity), and thus the MPCM slurry flowed through could absorb the heat from the battery simulator and remove some of the accumulated heat that could have negative impact on the battery safety and performance. For the accurate measurement, the corresponding data (temperature, pressure drop, and flow rate) in interest was monitored every 5s.

The test procedures include:

- Preparation: Before power on the simulated battery heat source, ensure all sensors such as the thermocouple, flow meter, and so on, could properly work as they were supposed to do. Before the first set of experiment, all devices should be calibrated to ensure the experimental acccuracy. If any abnormal data is found in the last test, the corresponding sensors should be re-calibrated in this preparation stage.
- Flowing: Start the flow circulating at the given volume flow rate, v_0, and monitor the flow meter until the readable data became stable for a period of 5 min.
- Heating: Once the flow circulating was stable, switch on the simulated battery heat source with the given C-rate working condition as proposed in the experimental plan. The simulated EV battery was a Nissan Leaf battery, with the information listed in Tab. 4.2. According to the heat generation rate of the EV battery (Equation 3.19), the simulated battery heat source could reach the C-rate of 1C, 2C, 3C, 4C, and 5C when the heat source voltage was set to 74 V, 105 V, 127 V, 147 V, and 164 V. The corresponding t_C could be calculated by Equation 3.7.
- Flow rate altering: Once the monitored temperatures, for example, battery core temperature, T_{cor}, and flow outlet temperature, T_{out}, were stable (within 1.5% fluctuation during 10 min), alter the flow rate, v_0, from 0.35 L/min to 0.6 L/min. Monitor the temperatures until they were almost unchanged (within the

tolerance given above).

- End: At the end of one C-rate experimental group, the battery heat source was shut down and cooled to the ambient temperature. Other components were powered off as well. If the experiments were supposed to continue after an C-rate experimental group, then water cooling will be used to cool the battery core temperature to the ambient temperature, after the core-heater was shut down. The sensors could be remained power on and wait for next procedures from flowing.

Tab 4.6 listed the test groups designed for the BTM experiment.

Tab. 4.6 Summary of the test groups.

No.	Coolant	v_0	r_C
1	water	0.35 – 0.6 L/min	1C
2	water	0.35 – 0.6 L/min	2C
3	water	0.35 – 0.6 L/min	3C
4	water	0.35 – 0.6 L/min	4C
5	water	0.35 – 0.6 L/min	5C
6	MPCM slurry	0.35 L/min	1C
7	MPCM slurry	0.35 L/min	2C
8	MPCM slurry	0.35 L/min	3C
9	MPCM slurry	0.35 L/min	4C
10	MPCM slurry	0.35 L/min	5C

4.3 Results and discussion

4.3.1 Water cooling

The influence of operating different C-rates from 1C to 5C on the BTM performance was discussed in this section from Fig. 4.8 to Fig. 4.18. T_{cor} represented the core battery temperature, while T_{out} represented the outlet temperature of the circulating fluid in the cooper pipe. The practical water volume flow rates recorded by the flow meter were listed in Tab 4.7.

Tab. 4.7 List of the water volume flow rate.

r_C	v_0 (set)	v_0 (monitored)
1C	v_1 (0.35 mL/min)	0.37 mL/min
2C	v_1 (0.35 mL/min)	0.31 mL/min
3C	v_1 (0.35 mL/min)	0.38 mL/min
4C	v_1 (0.35 mL/min)	0.36 mL/min
5C	v_1 (0.35 mL/min)	0.35 mL/min
1C	v_2 (0.50 mL/min)	0.52 mL/min
2C	v_2 (0.50 mL/min)	0.45 mL/min
3C	v_2 (0.50 mL/min)	0.46 mL/min
4C	v_2 (0.50 mL/min)	0.49 mL/min
5C	v_2 (0.50 mL/min)	0.53 mL/min
1C	v_3 (0.60 mL/min)	0.61 mL/min
2C	v_3 (0.60 mL/min)	0.60 mL/min
3C	v_3 (0.60 mL/min)	0.60 mL/min
4C	v_3 (0.60 mL/min)	0.61 mL/min
5C	v_3 (0.60 mL/min)	0.63 mL/min

Fig. 4.8 illustrates the BTM temperature profiles of the core battery temperature and outlet coolant temperature, T_{cor} and T_{out} respectively, when C-rate was set to 1C, but the volume flow rate of the coolant (water), v_0, was altered from v_1 to v_3. It was obvious with the water volume flow rate increasing, T_{cor} and T_{out} at equilibrium were reduced. When they were stable, increment of water volume flow rate from v_1 to v_2 can reduce T_{cor} from 17.24 °C to 16.95 °C, and T_{out} from 15.48 °C to 15.13 °C. Increment of water volume flow rate from v_2 to v_3 can respectively reduce T_{cor} and T_{out} to 16.69 °C and 14.89 °C. The maximum T_{cor} and T_{out} reached in condition 1C were 17.71 °C and 16.00 °C, respectively. The reason that the equilibrium T_{cor} or T_{out} was further controlled to a lower lecel could be that more thermal energy generated by the battery was absorbed and removed by the water with a higher volume flow rate circulating through the cooling module.

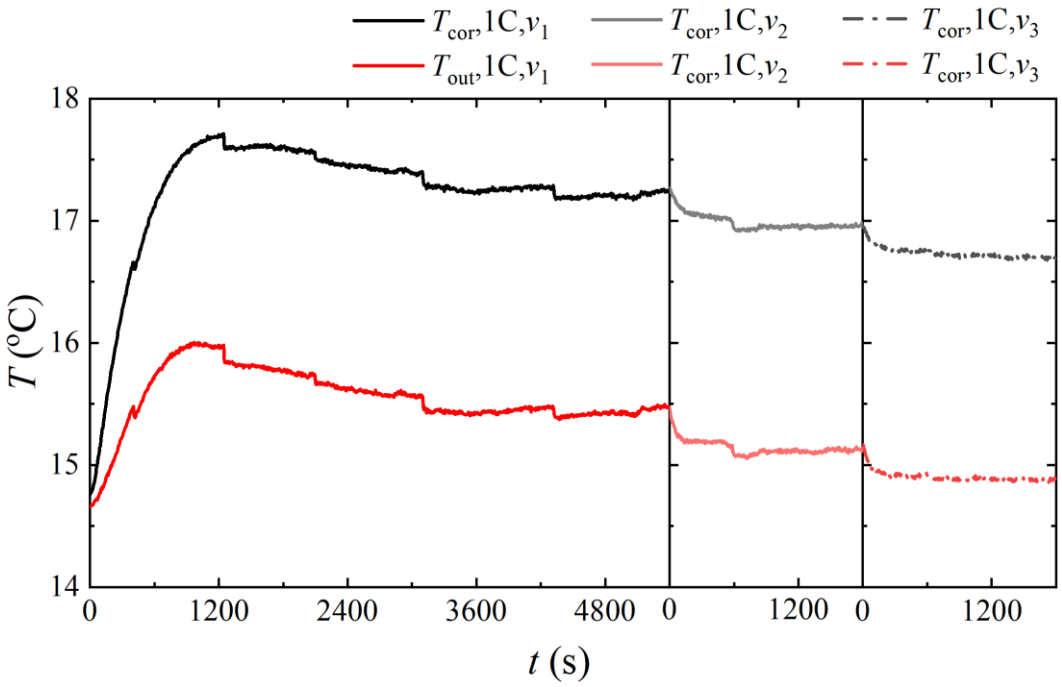

Fig. 4.8 T_{out} and T_{cor} vs. t and v_0, r_C =1C, using water as coolant.

Fig. 4.9 presents the temperature changes, ΔT, of T_{cor} and T_{out} in condition with C-rate of 1C, when water volume flow rate was altered from v_1 to v_3. The maximum temperature increment of T_{cor} and T_{out} were separately 2.95 °C and 1.34 °C. The temperature drops for T_{cor} from the maximum to the equilibrium value were 0.47 °C, 0.76 °C, and 1.93 for v_1, v_2 and v_3. Fig. 4.9 still presented a same shape with Fig. 4.8 but it moved the curves down to show the temperature difference between the absolute temperature to the initial temperature. Thus, other absolute temperature profiles were provided in Appendix. A (water cooling BTM) and Appendix. B (MPCM BTM) rather than presented in the thesis main body.

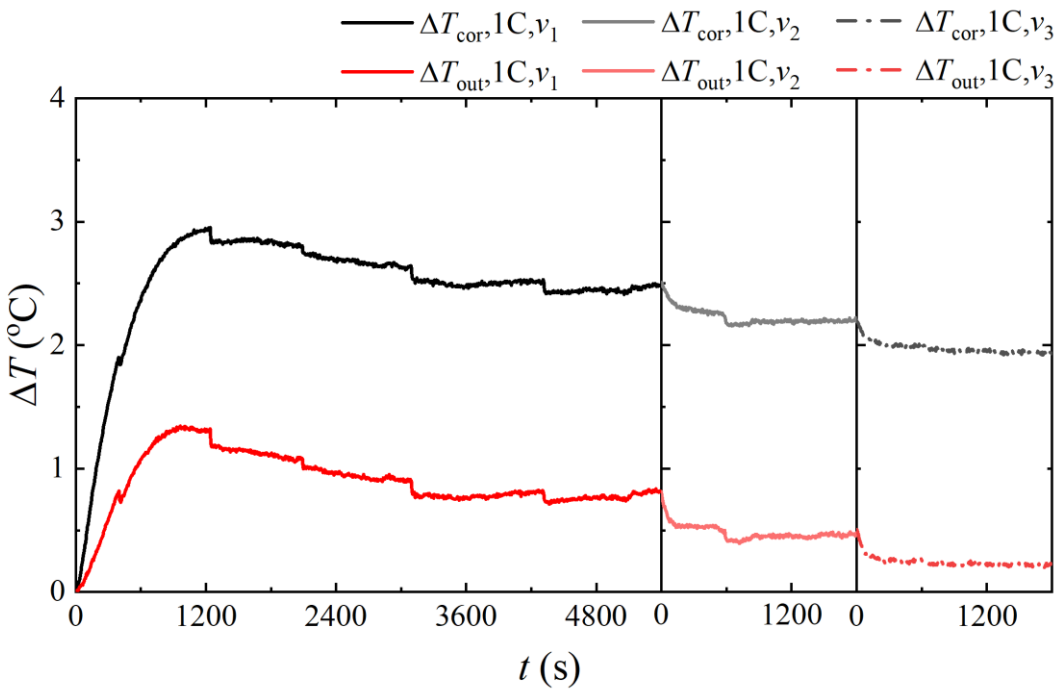

Fig. 4.9 ΔT_{out} and ΔT_{cor} vs. t and v_0, r_C =1C, using water as coolant.

Equation 4.4 presented the calculation of another performance indicator, the temperature changing rate, r_T. With a higher r_T, the temperature could increase faster. Here in the battery cooling, minus value of r_T was preferred with a higher absolute value. In that case, the core battery temperature could be faster controlled within a desired temperature range.

$$r_T = \frac{dT}{dt} \qquad 4.4$$

Fig. 4.10 displays the temperature changing rate, r_T, of T_{cor}, when C-rate and water volume flow rate were separately set to 1C and v_1 to v_3. Obviously, from v_1 to v_3, the time for T_{cor} to become stable, t_{sta}, was reduce. For water volume flow rate was v_1, t_{sta} was approximately 910 s, while for that was v_2 and v_3 respectively, t_{sta} was about 155 s and 115 s. The result demonstrated that the high coolant volume flow rate could also decrease the cooling time required by BTM. This could be resulted by the enhanced

heat transfer between the battery to the cooling module, as the increased water volume flow rate could positively influence on the heat transfer coefficient and thus improve the heat transfer rate per unit time.

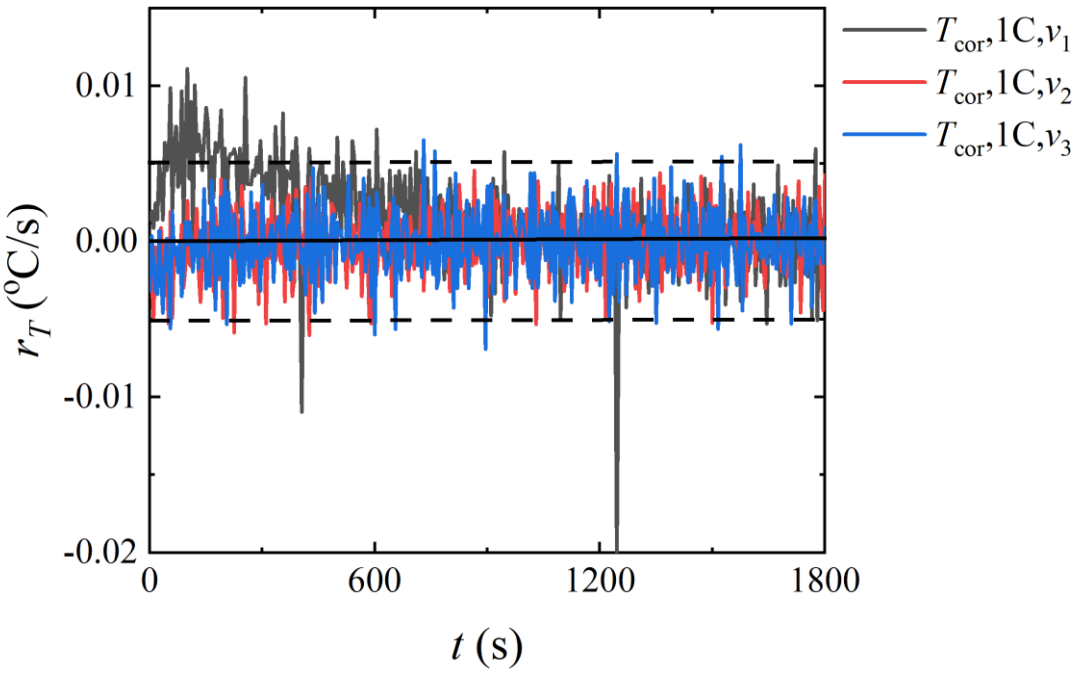

Fig. 4.10 r_T (T_{cor}) vs. t and v_0, r_C =1C, using water as coolant.

Fig. 4.11 is the illustration considering the temperature change, ΔT, of T_{cor} and T_{out} in the condition with C-rate of 2C. The water volume flow rate ranges from v_1 to v_3. The maximum temperature change of T_{cor} and T_{out} were separately 6.33 °C and 3.60 °C, found between the beginning and the equilibrium of v_1. The temperature drops for T_{cor} from the maximum to the equilibrium value were 0.03 °C, 0.72 °C, and 1.30 °C for v_1, v_2 and v_3. The result demonstrats that with a C-rate of 2C, the equilibrium T_{cor} or T_{out} could not be controlled under its maximum value with the water volume flow rate of v_1. Higher volume flow rate is desired if core battery temperature lower than its maixmum teperature is required in the condition with C-rate no smaller than 2C. It could be due to the high C-rate leading into higher heat generation in both rate (quicker generation) and amount (more generation).

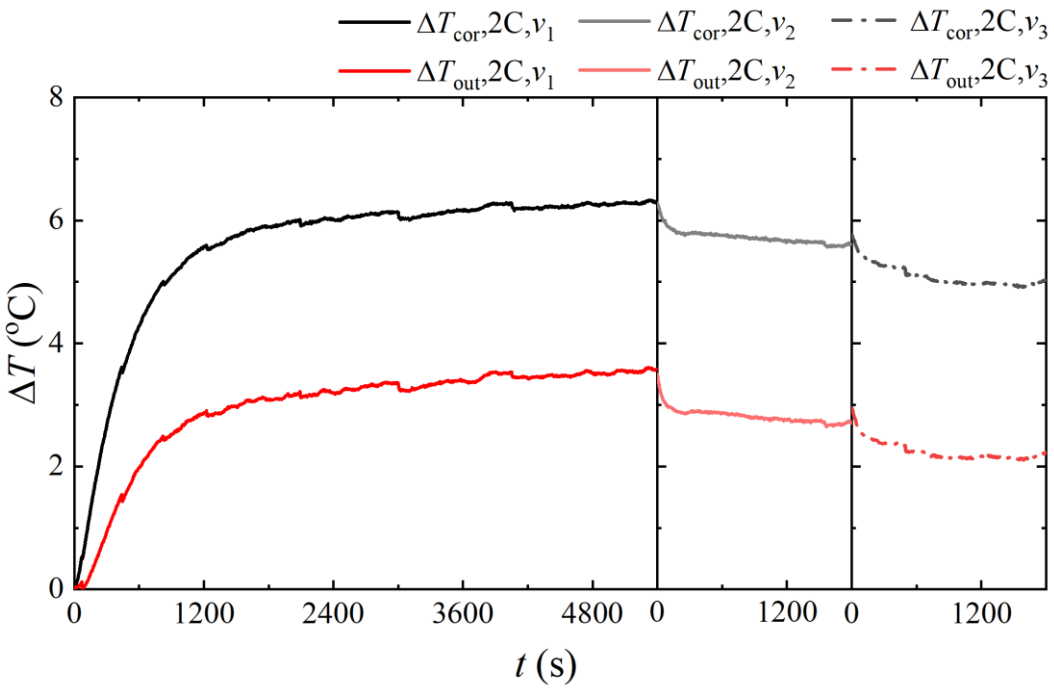

Fig. 4.11 ΔT_{out} and ΔT_{cor} vs. t and v_0, r_C =2C, using water as coolant.

Fig. 4.12 displays the temperature changing rate, r_T, of T_{cor}. In this group, the C-rate and water volume flow rate were separately set to 2C and v_1 to v_3. It was discovered that from v_1 to v_3, the time for T_{cor} to become stable, t_{sta}, was declined. For water volume flow rate was v_1, t_{sta} was approximately 1510 s, while for that was v_2 or v_3 respectively, t_{sta} was 330 s or 135 s. Moreover, at the start of the red and blue curves (with the volume flow rate of v_2 and v_3, respectively), minus value is observed, which means that the core battery temperature was decreased for a while until stable (r_T was almost none).

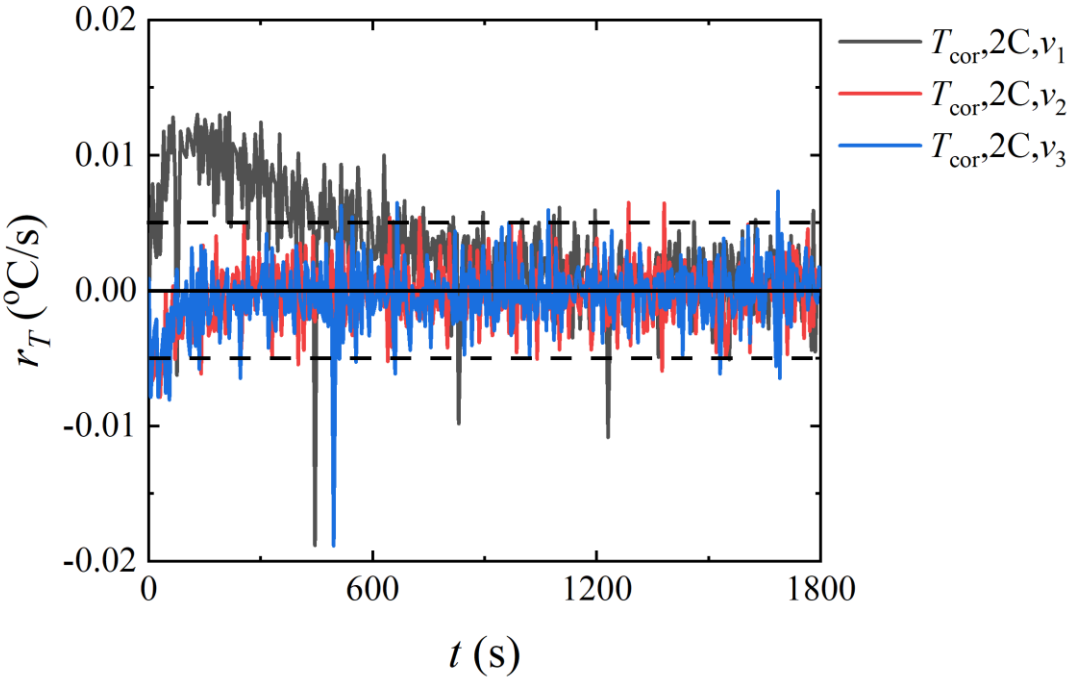

Fig. 4.12 r_T (T_{cor}) vs. t and v_0, r_C =2C, using water as coolant.

Fig. 4.13 shows the temperature change, ΔT, of T_{cor} and T_{out} with a C-rate of 3C, when the water volume flow rate was from v_1 to v_3. The maximum temperature change of T_{cor} and T_{out} were separately 9.22 °C and 5.24 °C, found between the beginning and the equilibrium of v_1. The temperature drops for T_{cor} and T_{out} from the maximum to the equilibrium value were 0.03 °C, 0.35 °C, and 0.81 for v_1, v_2 and v_3. The higher volume flow rate could further decrease the core battery temperature and outlet coolant temperature. The reason has been discussed in above contents.

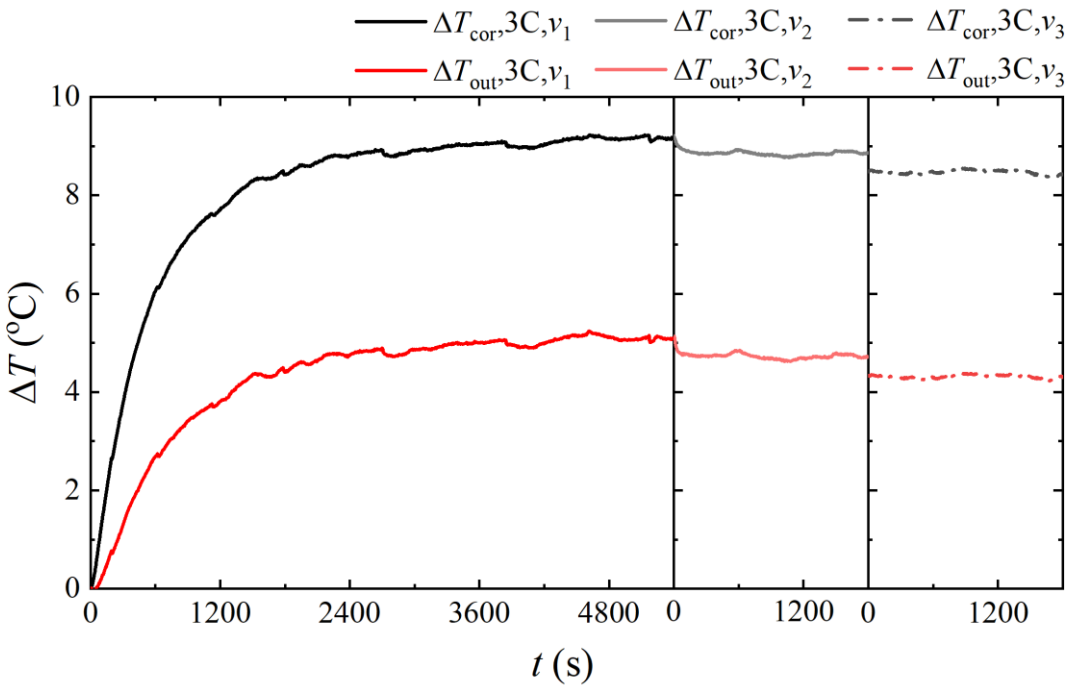

Fig. 4.13 ΔT_{out} and ΔT_{cor} vs. t and v_0, r_C =3C, using water as coolant.

Fig. 4.14 displayed the temperature changing rate, r_T, of T_{cor}, with C-rate and water volume flow rate being 3C and v_1 to v_3, relatively. It was discovered that from v_1 to v_3, the time for T_{cor} to become stable, t_{sta}, was declined. For water volume flow rate was v_1, t_{sta} was 1540 s, while for that was v_2 or v_3 respectively, t_{sta} was 210 s or 110 s. Again, a high coolant volume flow rate could faster remove the heat from the cooling-required battery.

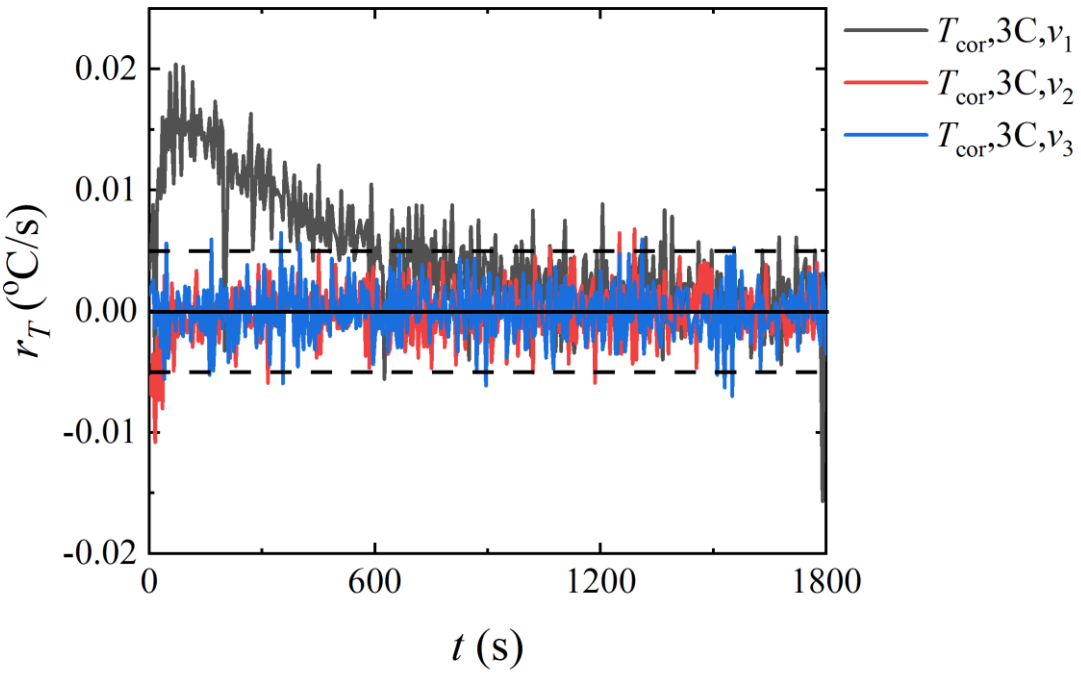

Fig. 4.14 r_T (T_{cor}) vs. t and v_0, r_C =3C, using water as coolant.

Fig. 4.15 is the experimental result of the temperature change, ΔT, of T_{cor} and T_{out} with C-rate of 4C, when the water volume flow rate was from v_1 to v_3. The maximum temperature change of T_{cor} and T_{out} were separately 15.22 °C and 10.31 °C, found between the beginning and the equilibrium of v_1. The temperature drops for T_{cor} from the maximum to the equilibrium value were separately 0.16 °C and 0.82 for v_2 and v_3. It was revealed that with a C-rate of 4C, the water volume flow rate v_1 is hard to control and decrease the core battery temperatrue. Even v_2 is not enough to decrease the core battery temperature to under its maximum value.

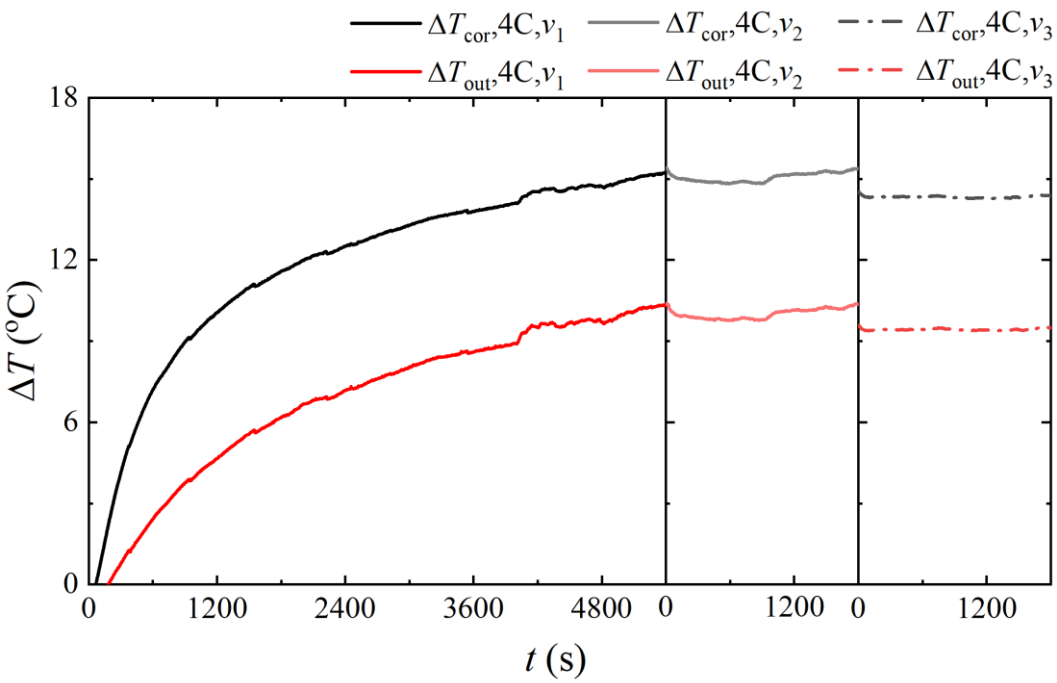

Fig. 4.15 ΔT_{out} and ΔT_{cor} vs. t and v_0, r_C =4C, using water as coolant.

Fig. 4.16 displays the temperature changing rate, r_T, of T_{cor}, when C-rate and water volume flow rate were separately set to 4C and v_1 to v_3. From v_1 to v_3, the time for T_{cor} to become stable, t_{sta}, was declined. For water volume flow rate was v_1, t_{sta} was about 2230 s, while for that was v_2 or v_3 respectively, t_{sta} was 180 s or 80 s. The result showed that with the C-rate increasing, the time for T_{cor} to be stable was also enlarged using the water volume flow rate of v1. However, the influence of C-rate on the t_{sta} was very limited, as this time was in a similar value given the lower C-rate.

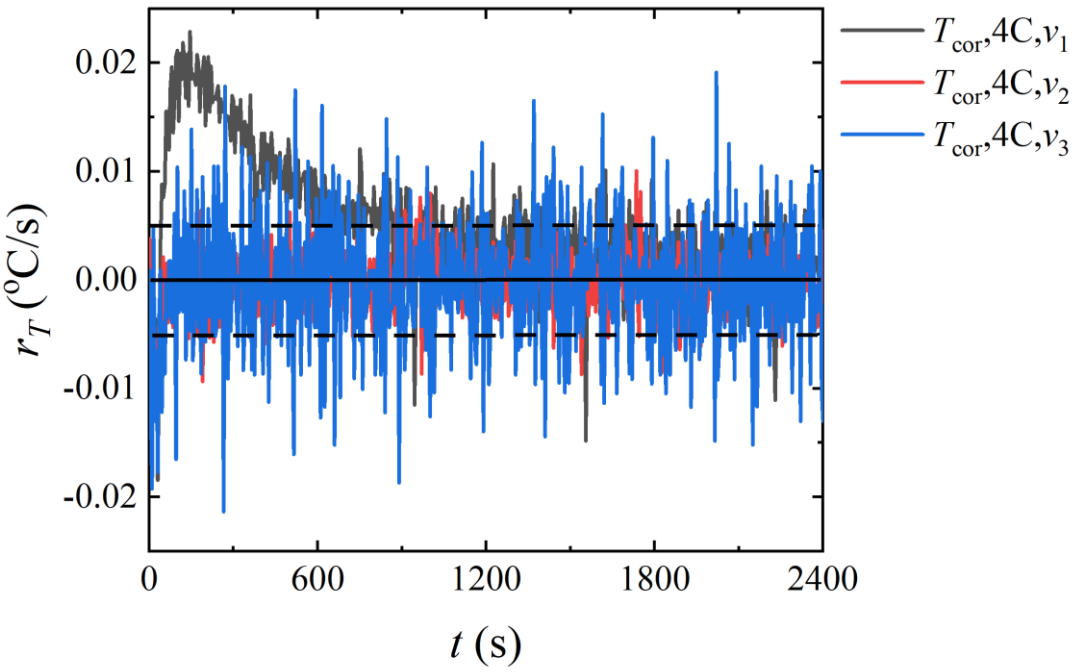

Fig. 4.16 r_T (T_{cor}) vs. t and v_0, r_C =4C, using water as coolant.

Fig. 4.17 is the diagram considering the temperature change, ΔT, of T_{cor} and T_{out} in condition 5C, when the water volume flow rate was from v_1 to v_3. The maximum temperature change of T_{cor} and T_{out} were separately 17.73 °C and 11.33 °C, found between the beginning and the equilibrium of v_1. The temperature drops for T_{cor} from the maximum to the equilibrium value were 0.13 °C, 1.11 °C, and 1.58 °C for v_1, v_2 and v_3.

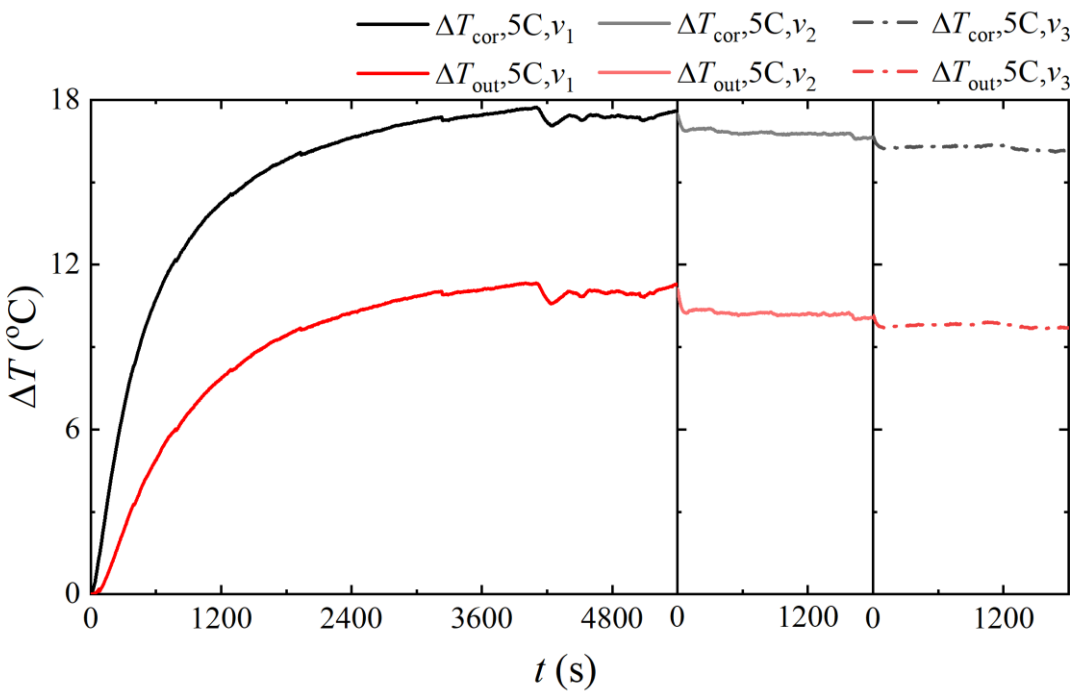

Fig. 4.17 ΔT_{out} and ΔT_{cor} vs. t and v_0, r_C =5C, using water as coolant.

Fig. 4.18 displays the temperature changing rate, r_T, of T_{cor}, when C-rate and water volume flow rate were separately set to 5C and v_1 to v_3. It was discovered that from v_1 to v_3, the time for T_{cor} to become stable, t_{sta}, was declined. For water volume flow rate was v_1, t_{sta} was 2375 s, while for that was v_2 or v_3 respectively, t_{sta} was 145 s or 90 s. Even though the C-rate was set to as high as 5C, the tsta is still quite similar with that in the conditions where C-rate was lower, using the water volume flow rate of v_2 and v_3. It could be easily understood, as the first setting of water volume flow rate of v_1, the coolant was required to absorb the rapidly increased core battery temperature at the starting stage, while v_2 and v_3 were tested when the first stage using v_1 was stable. In these following stages, the thermal state of the battery is balanced rather than huge heat was accumulated until the equilibrium between the coolant and battery heat source was formed.

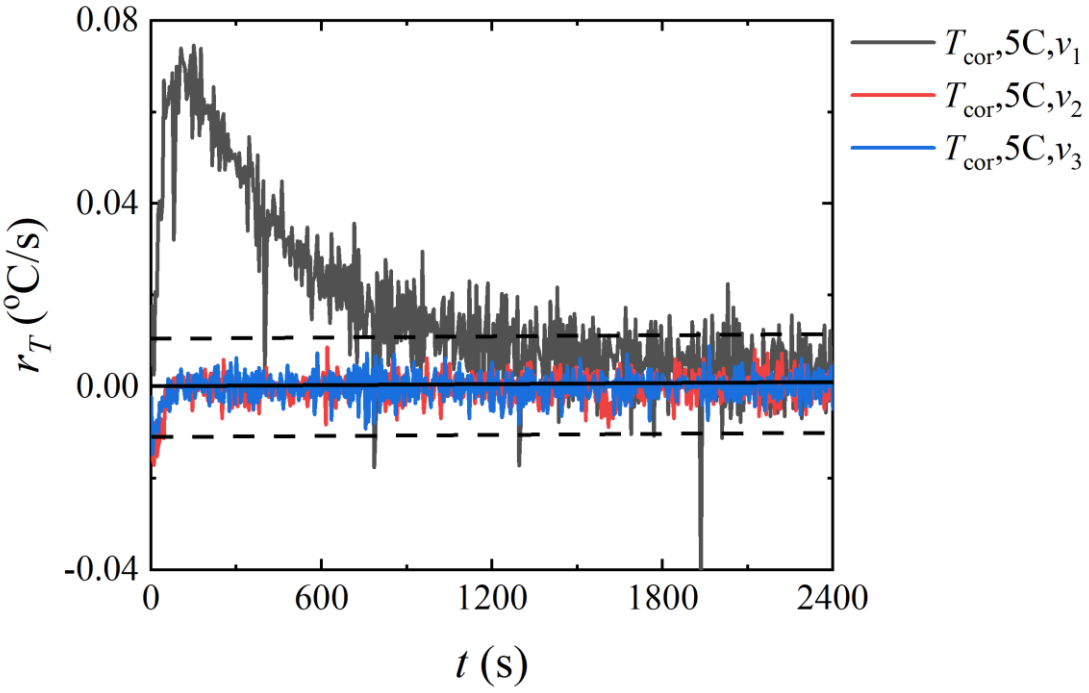

Fig. 4.18 r_T (T_{cor}) vs. t and v_0, r_C =5C, using water as coolant.

The influence of various water volume flow rate from v_1 to v_3 on the BTM performance was compared as shown from Fig. 4.18 to Fig. 4.23. The practical water volume flow rates were listed in Tab 4.7.

Fig. 4.19 is the illustration considering the temperature change, ΔT, of T_{cor} and T_{out} in condition where the water volume flow rate was v_1 and C-rate varied from 1C to 5C. Obviously, with C-rate increasing, ΔT also increases at the same time.

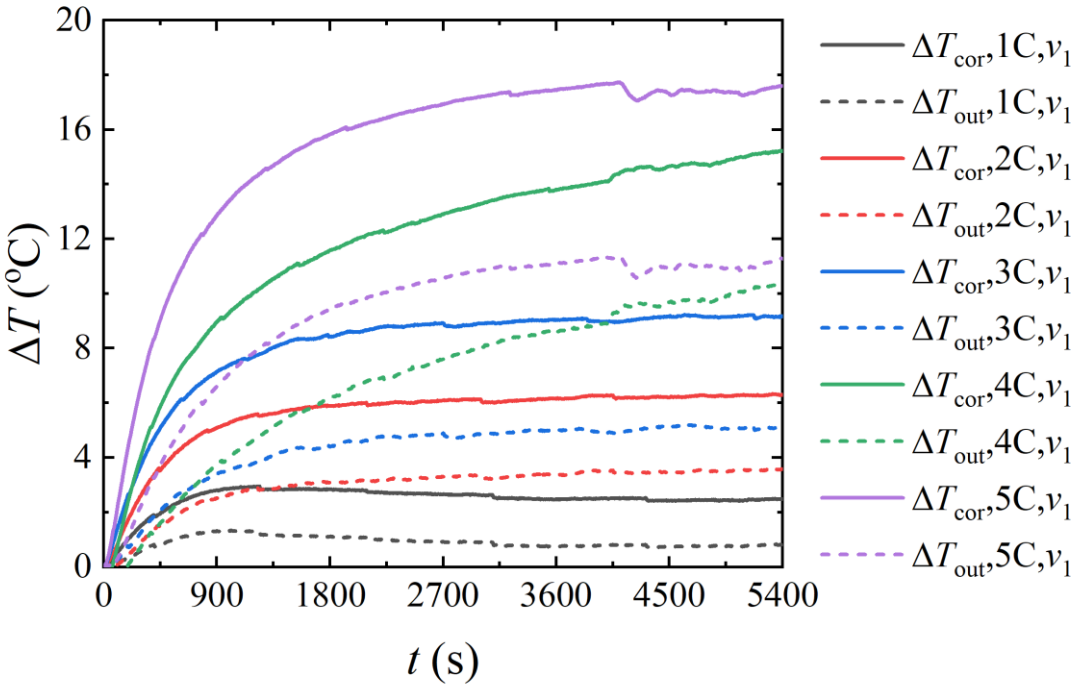

Fig. 4.19 ΔT_{out} and ΔT_{cor} vs. t and r_C, v_0=v_1, using water as coolant.

The maximum temperature change, Max(ΔT), of T_{cor} and T_{out} for various C-rates are listed in Tab. 4.8. The temperature drops, T_{drop}, for T_{cor} and T_{out} from the maximum to the equilibrium value were also recorded in Tab. 4.9. This temperature drop reflected the extent that the battery temperatrue controlled lower than the maximum battery temperature. The largest Max(ΔT) and T_{drop} were found to be in condition where C-rate was 5C and the volume flow rate was v_1, and condition where C-rate was 1C and the volume flow rate was v_1, respectively.

Tab. 4.8 List of Max(ΔT) and T_{drop}, when C-rate changed from 1C to 5C and water volume flow rate was v_1.

Term	Max(ΔT)/ °C	T_{drop}/°C
T_{cor},1C,v_1	2.91	0.43
T_{cor},2C,v_1	6.30	
T_{cor},3C,v_1	9.19	
T_{cor},4C,v_1	15.22	
T_{cor},5C,v_1	17.73	0.13

T_{out},1C,v_1	1.31	0.50
T_{out},2C,v_1	3.58	
T_{out},3C,v_1	5.10	
T_{out},4C,v_1	1031	
T_{out},5C,v_1	11.33	0.05

Fig. 4.20 displays the temperature changing rate, r_T, of T_{cor}, when C-rate and water volume flow rate were separately set to 1C-5C and v_1. It was discovered that from C-rate was 1C to 5C, the time for T_{cor} to become stable, t_{sta}, was inclined from 910 s to 2375 s. Moreover, before stable, r_T increased with C-rate increasing. The maximum r_T was 7.46 x 10^{-2} °C/s at t= 150 s, when C-rate was 5C. It revealed the rapidly increased core battery temperatrue stage at the strating stage of a battery. Moreover, it was clear that with the C-rate increasing, the tsta was increased as the it was enlarged in both battery heat generation rate and amount. Thus, the higher C-rate means more challenge.

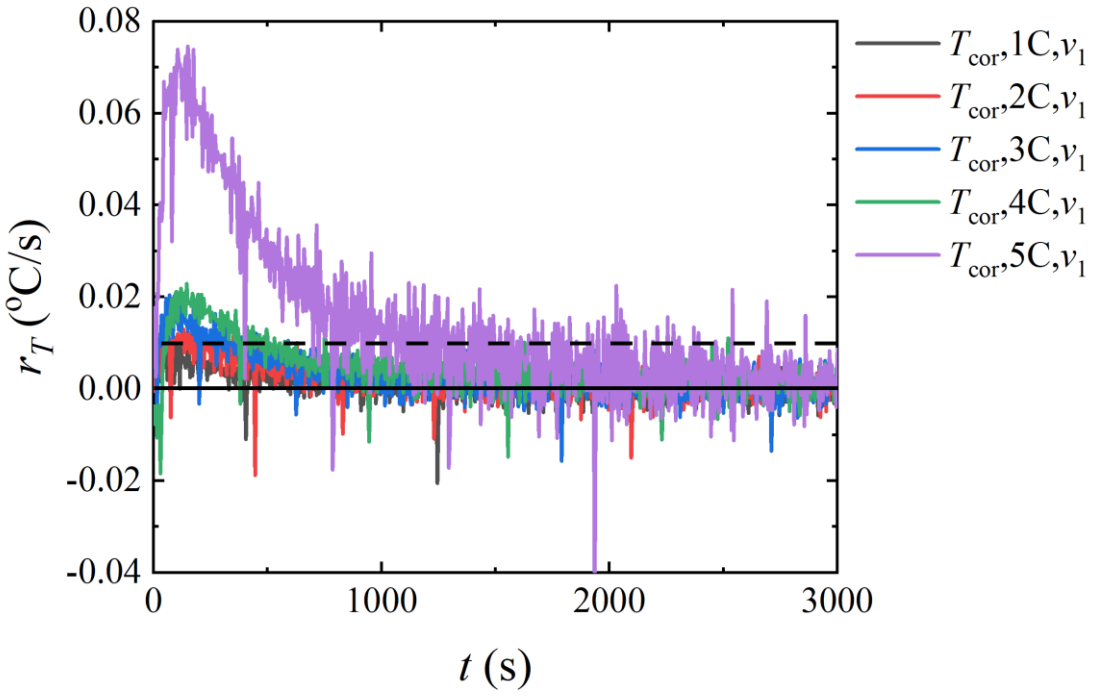

Fig. 4.20 r_T (T_{cor}) vs. t and r_C, v_0=v_1, using water as coolant.

Fig. 4.21 is the illustration considering the temperature change, ΔT, of T_{cor} and T_{out} in condition where the water volume flow rate was v_2 and C-rate varied from 1C to 5C. Obviously, with C-rate increasing, ΔT also increased at the same time. It could be seen that in the very early time, a tiny drop of each curve existed. This is due to the more heat removed by the more coolant circulating through the cooling module in unit time.

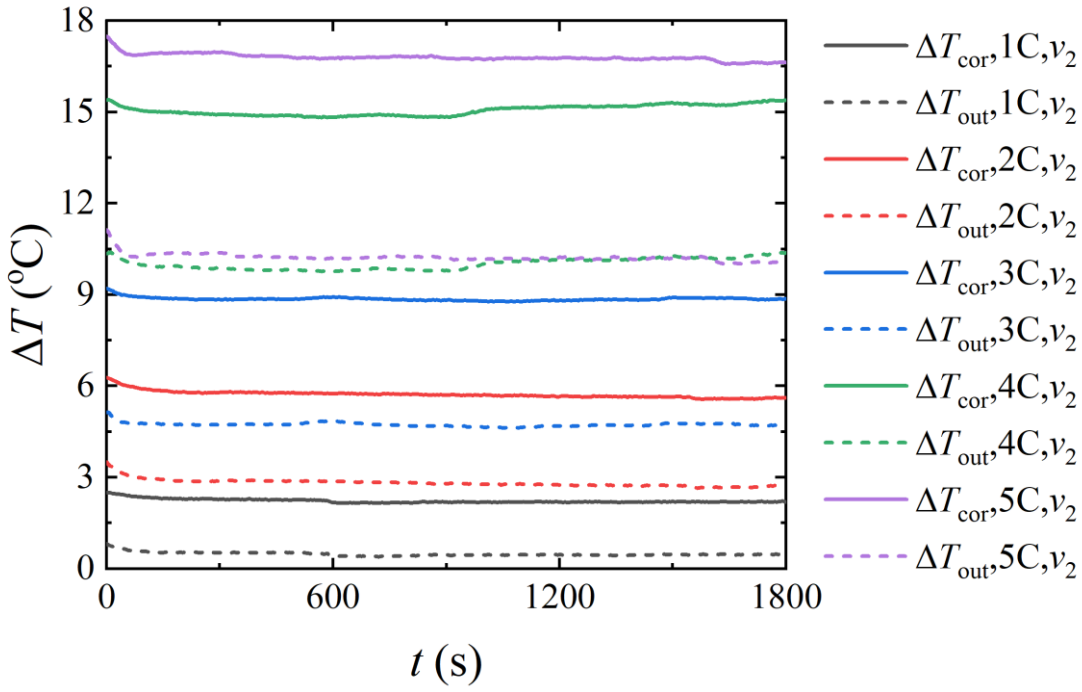

Fig. 4.21 Schematic diagram of ΔT_{out} and ΔT_{cor} vs. t and r_C, v_0=v_2, using water as coolant.

The maximum temperature change, Max(ΔT), of T_{cor} and T_{out} for various C-rates are listed in Tab. 4.9. The temperature drops, T_{drop}, for T_{cor} and T_{out} from the maximum to the equilibrium value were also recorded in Tab. 4.10. The largest Max(ΔT) and T_{drop} were found to be in condition 5C.

Tab. 4.9 List of Max(ΔT) and T_{drop}, when C-rate changed from 1C to 5C and water volume flow rate was v_2.

	Max(ΔT)/ °C	T_{drop}/°C
T_{cor},1C,v_2	2.51	0.32

T_{cor},2C,v_2	6.28	0.67
T_{cor},3C,v_2	9.21	0.34
T_{cor},4C,v_2	15.38	0.52*
T_{cor},5C,v_2	17.48	0.86
T_{out},1C,v_2	0.81	0.34
T_{out},2C,v_2	3.50	0.79
T_{out},3C,v_2	5.13	0.41
T_{out},4C,v_2	10.35	0.56
T_{out},5C,v_2	11.12	1.06

Fig. 4.22 displays the temperature changing rate, r_T, of T_{cor}, when C-rate and water volume flow rate were separately set to 1C-5C and v_2. It was discovered that from C-rate was 1C to 5C, the time for T_{cor} to become stable, t_{sta}, ranged from 145 s to 330 s. Moreover, before stable, r_T increases with C-rate increasing. The maximum r_T was -1.71 x 10^{-2} °C/s at t = 10 s, when C-rate was 5C. In the figure, the minus r_T could be observed at the starting time, which reflected the dynamic temperature controlling stage of the BTM when switching to the higher coolant volume flow rate. With r_C changing, at the testing procedure using water volume flow rate of v_2 could have similar tsta.

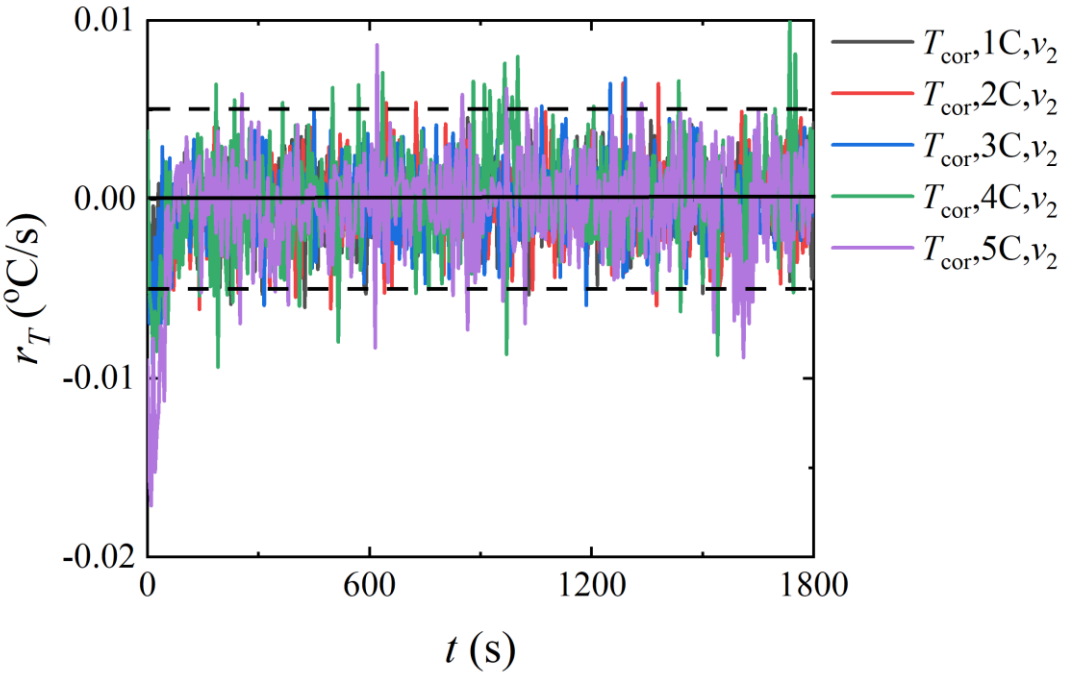

Fig. 4.22 r_T (T_{cor}) vs. t and r_C, v_0=v_2, using water as coolant.

Fig. 4.23 is the illustration considering the temperature change, ΔT, of T_{cor} and T_{out} in condition where the water volume flow rate was v_3 and C-rate varied from 1C to 5C. Obviously, with C-rate increasing, ΔT also increases at the same time. Similarly with Fig. 4.21, a temperature drop stage was discovered at the beginning of the curves, showing that the battery temperature or the outlet water temperature was quickly decreased by the increment of water volume flow rate. More heat was removed given v_2. Heat transfer rate between the cooling fluid and the battery was also enhanced by the volume flow rate increment.

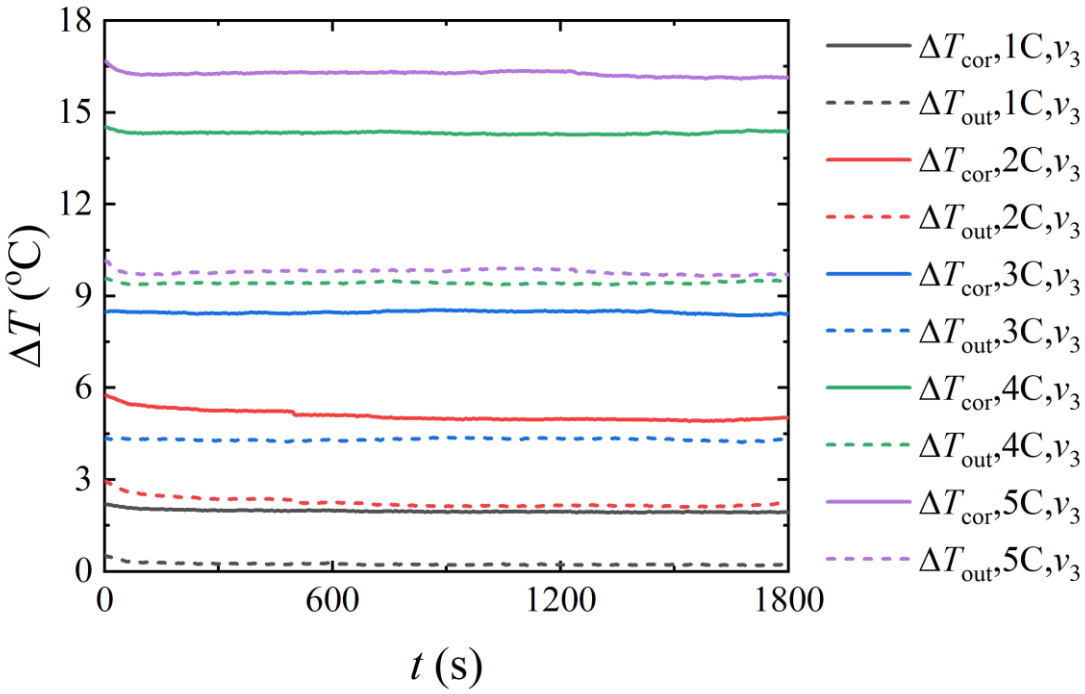

Fig. 4.23 ΔT_{out} and ΔT_{cor} vs. t and r_C, v_0=v_3, using water as coolant.

The maximum temperature change, Max(ΔT), of T_{cor} and T_{out} for various C-rates were listed in Tab. 4.10. The temperature drops, T_{drop}, for T_{cor} and T_{out} from the maximum to the equilibrium value were also recorded in Tab. 4.11. The largest Max(ΔT) and T_{drop} were found to be in the same testing condition with the C-rate of 5C.

Tab. 4.10 List of Max(ΔT) and T_{drop}, when C-rate changed from 1C to 5C and water volume flow rate was v_3.

	Max(ΔT)/ °C	T_{drop}/°C
T_{cor},1C,v_3	2.20	0.27
T_{cor},2C,v_3	5.76	0.73
T_{cor},3C,v_3	8.48	0.04
T_{cor},4C,v_3	14.52	0.13
T_{cor},5C,v_3	16.66	0.51
T_{out},1C,v_3	0.51	0.23
T_{out},2C,v_3	2.94	0.73
T_{out},3C,v_3	4.33	0.03
T_{out},4C,v_3	9.56	0.07
T_{out},5C,v_3	10.15	0.45

Fig. 4.24 displays the temperature changing rate, r_T, of T_{cor}, when C-rate and water volume flow rate were separately set to 1C-5C and v_3. It was discovered that from C-rate was 1C to 5C, the time for T_{cor} to become stable, t_{sta}, varied from 80 s to 135 s. Moreover, before stable, r_T increases with C-rate increasing. The maximum r_T was -1.48 x 10^{-2} °C/s at t= 5 s, when C-rate was 5C.

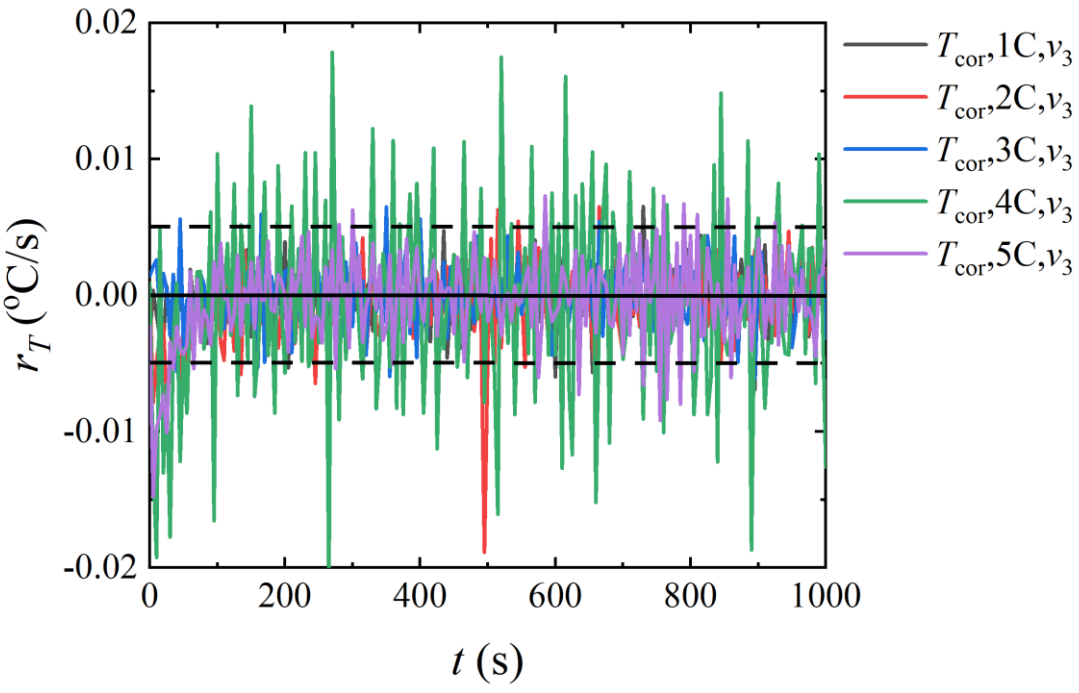

Fig. 4.24 r_T (T_{cor}) vs. t and r_C, v_0=v_3, using water as coolant.

4.3.2 MPCM cooling

MPCM BTM experiments were conducted with only C-rate varying. Fig. 4.25 to Fig. 4.30 were the results of MPCM cooling. The volume flow rate of MPCM slurry was controlled by the same pump power that used in the water-cooling experiment with v_1. In this case, the high viscosity of MPCM slurry could reduce the volume flow rate of MPCM slurry, compared to the water volume flow rate.

Fig. 4.25 presented the core battery temperature change, ΔT_{cor} in condition where the MPCM volume flow rate was fixed and C-rate varied from 1C to 5C. Obviously, with time elapsing or C-rate increasing, ΔT_{cor} became larger. At the end of t=1.2 x 10^4 s, ΔT_{cor} was respectively, 11.66 °C, 26.87 °C, 31.66 °C, 36.50 °C, and 46.26 °C for conditions from C-rate was 1C to 5C. The increment of C-rate raised the battery heat generation rate, thus in the starting stage the higher C-rate curve was always above the lower C-rate curve. A platform shape gradually appeared after the rapid increment showing the MPCM functions to absorb the battery heat (start to melt).

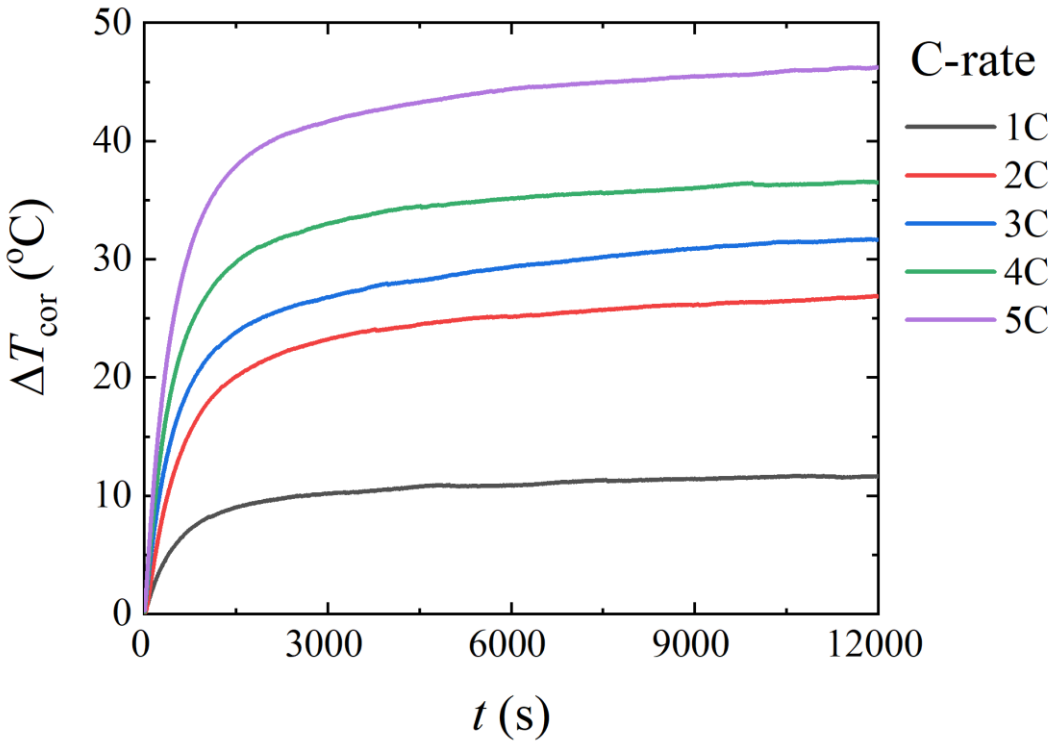

Fig. 4.25 ΔT_{cor} vs. t and r_C, using MPCM slurry as coolant.

Fig. 4.26 displayed the temperature changing rate, r_T, of T_{cor}, when C-rate was set to 1C-5C using MPCM slurry as working media. It was discovered that from C-rate was 1C to 5C, the time for T_{cor} to become stable, t_{sta}, was inclined from 1715 s to 2375 s. Moreover, before stable, r_T increases with C-rate increasing. The maximum r_T was 7.90 °C/s at t= 55 s, when C-rate was 5C. The high C-rate requires high operational current intensity, which could increase the battery generation rate. A peak could be discovere on each curve, which reflected the time point where the core PCM melting latent heat gradually take the main cooling resbonsibility in the BTM system. The heat generation rate was fixed using a constant C-rate, thus the decrease of r_T represents the cooling effect of MPCM.

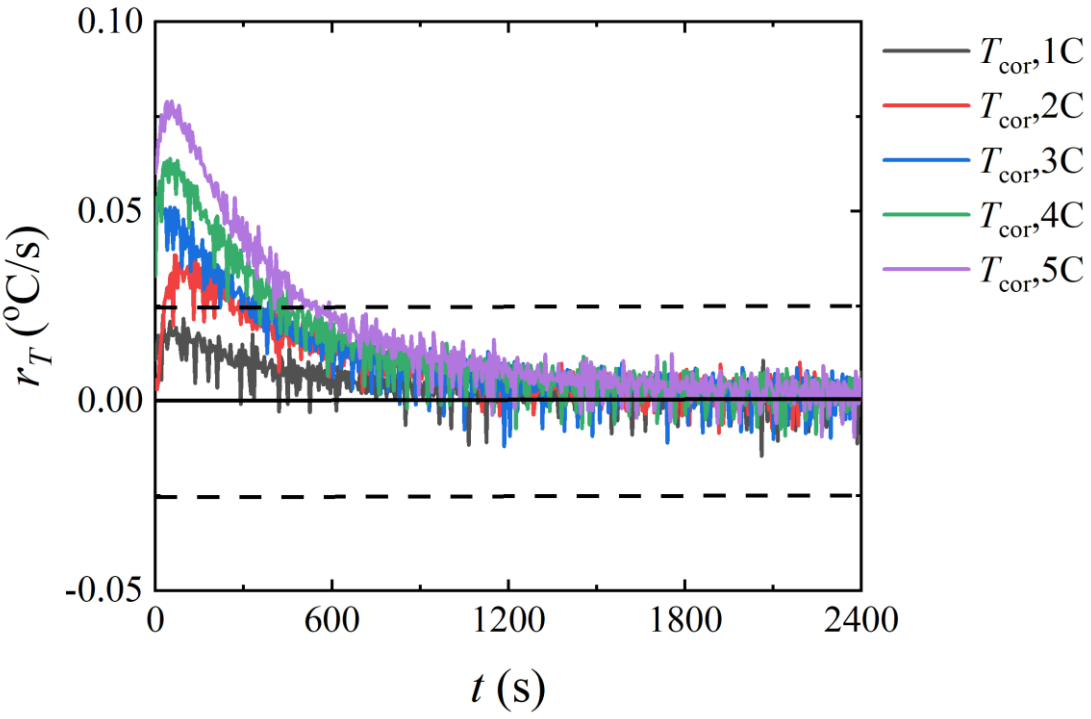

Fig. 4.26 r_T (T_{cor}) vs. t and r_C, using MPCM slurry as coolant.

Fig. 4.27 presents the inlet MPCM slurry temperature change, ΔT_{in}, in condition where the MPCM volume flow rate was fixed, and C-rate varied from 1C to 5C. It was observed that with time elapsing, ΔT_{in} increases, which was due to the lack of the cooling capacity of the employed water bath. Even though part of the heat absorbed in the MPCM slurry could be exchanged with the water bath, it remains some residue in the MPCM slurry, thus the MPCM slurry inlet temperature increased in the coolant circulating process.

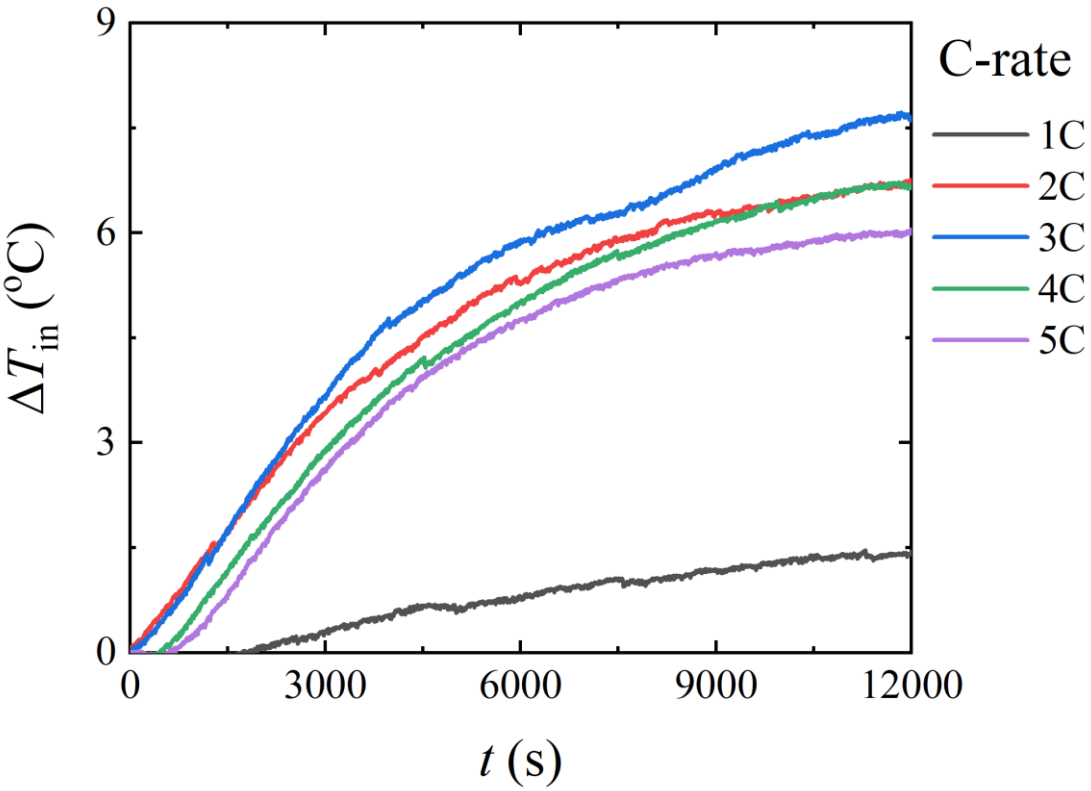

Fig. 4.27 ΔT_{in} vs. t and r_C, using MPCM slurry as coolant.

Fig. 4.28 displayed the absolute temperature of outlet MPCM slurry temperature, T_{out}, versus different C-rates. The grey area was the MPCM melting temperature range, according to the information shown in Tab. 4.1. It was discovered that in condition 1C, T_{out} was below the area, which meant that the outlet MPCM slurry could not reach its lowest melting temperature. In conditions with C-rate higher than 2C, T_{out} reached the suitable working temperature in the order 5C to 2C towards time cost. At the end of 15000 s, T_{out} of condition 2C and 4C were still in the range, while those of condition 3C and 5C came out from the melting temperature range. As at 15000s 2C reached almost the border but still in the grey area, 2C was regarded as the optimal operational condition for the battery cooling.

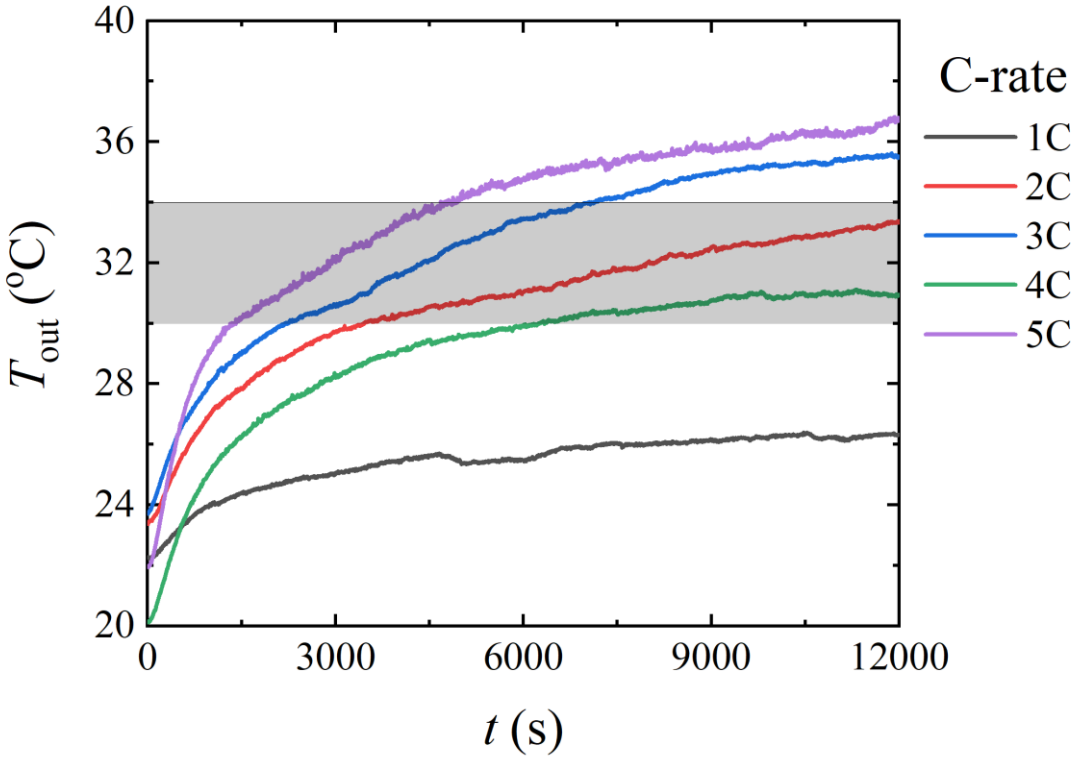

Fig. 4.28 T_{out} vs. t and r_C, using MPCM slurry as coolant.

Fig. 4.29 was the illustration of the outlet MPCM temperature change, considering C-rate from 1C to 5C. Before the time around 6000 s, ΔT_{out} gained the order from smallest to the largest of 1C to 5C, while after that time point, 3C and 4C switched their order. It is because that as shown in Fig. 4.28, the absolute T_{out} included the condition with C-rate of 2C, 3C, and 4C. However, the group using a C-rate of 3C finally reached out of the grey melting zone, which indicated that the MPCM slurry has totally melted to the liquid phase. Different with 3C group, 4C group still in the melting range, which enable the cooling module to better control the core battery temperature and thus achieve the lower outlet coolant temperature change.

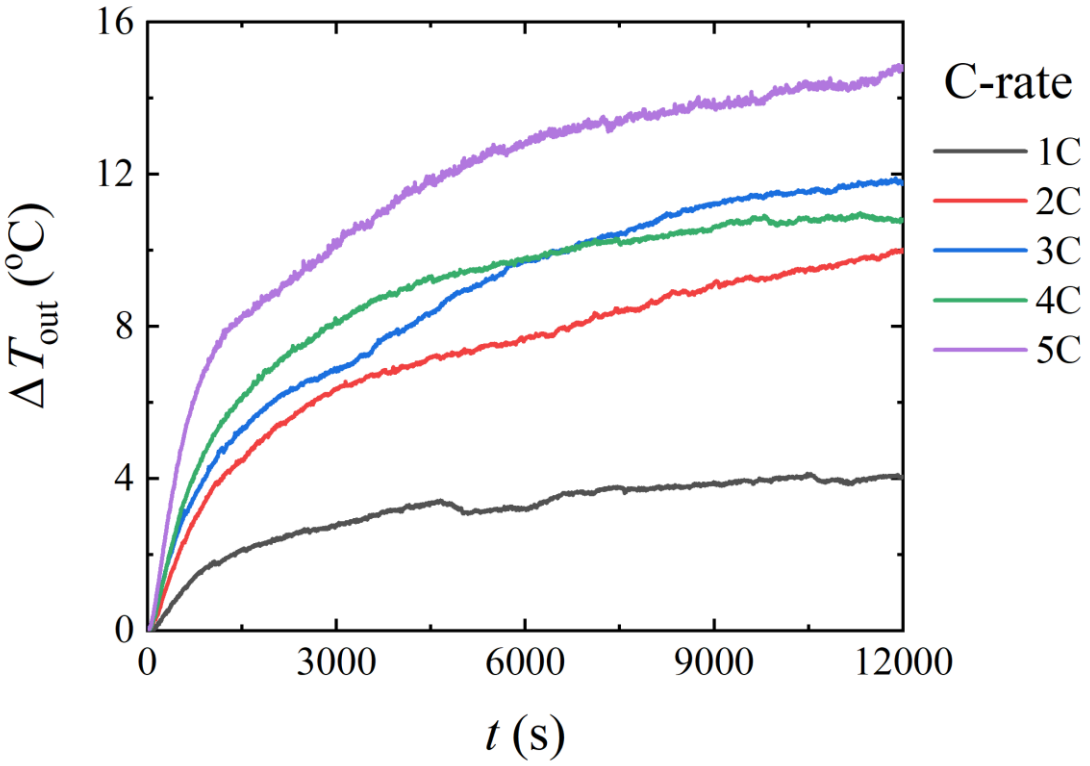

Fig. 4.29 T_{out} vs. t and r_C, using MPCM slurry as coolant.

Fig. 4.30 calculated the rate of outlet MPCM slurry temperature change. It was discovered that from C-rate was 1C to 5C, the time for T_{cor} to become stable, t_{sta}, was inclined from 1065 s to 2020 s. Moreover, before stable, r_T increases with C-rate increasing. The maximum r_T was 2.00 x 10^{-2} °C/s at t= 265 s, when C-rate was 5C. Compared to that of T_{cor}, the r_T of T_{out} were roughly lower than 0.025 °C/s, showing a milder temperature change during the cooling process in the coolant than in the battery.

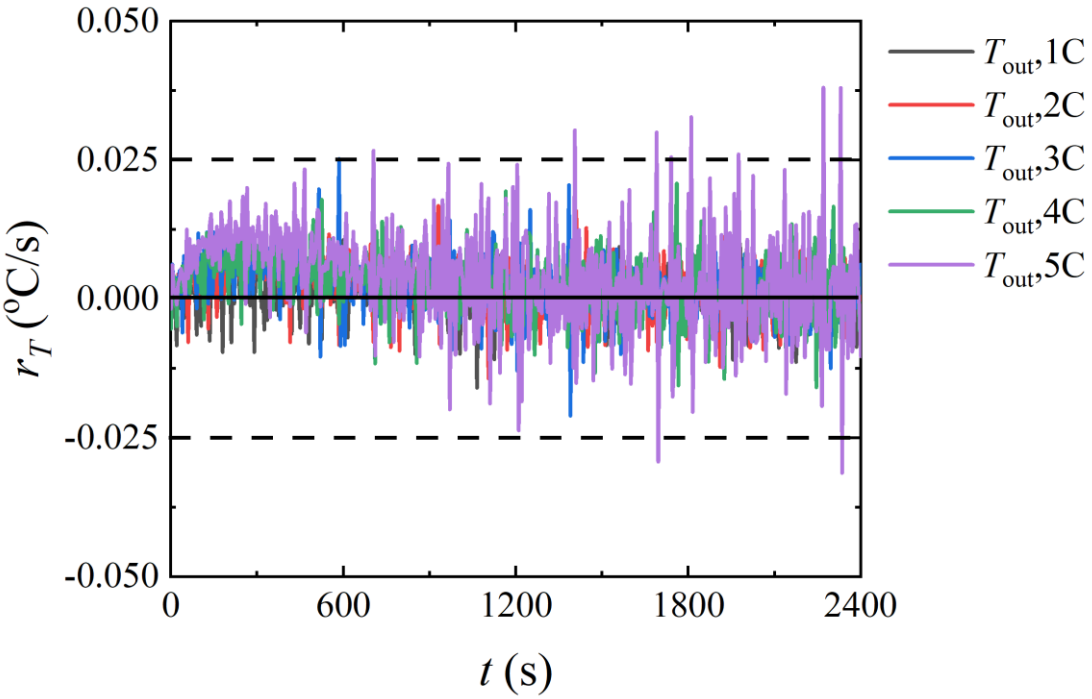

Fig. 4.30 r_T (T_{out}) vs. t and r_C, using MPCM slurry as coolant.

4.4 Conclusion

In this chapter, experimental investigation of using water or MPCM slurry as cooling media to circulate in the BTM was conducted.

In water cooling experiment, the discovery was concluded as:

- With the water flow rate increasing, T_{out} and T_{cor} could be further decreased. The maximum T_{cor} in condition 1C was 17.71 °C. The equilibrium T_{cor} or T_{out} was further controlled to a lower level because that more battery heat generation was absorbed and removed by the water with a higher volume flow rate. Moreover, the high coolant volume flow rate could also increase the battery temperature decreasing rate.

- With the C-rate increasing, T_{out} and T_{cor} were increased given the same running time. The high C-rate means a high operation current density, which enlarge the battery heat generation in both gross amount and rate.

In MPCM slurry experiment, the findings were summarised as:

- With C-rate increasing, T_{out} and T_{cor} were enlarged at the same time point over the experimental tests. The reason was the same as it has been explained in the water-cooling experiment.
- The optimal working condition for employing MPCM slurry BTM was 2C, as it could be deduced that the group using C-rate of 2C has the longest time of MPCM slurry spend in the melting range from the result of absolute outlet MPCM slurry temperature.

In a summary, in a flow BTM system, high coolant flow rate would be preferred as it provides higher cooling capacity and cooling rate. The working condition should be carefully considered to select the optimal coolant, as different cooling fluid may refer to distinguished optimal function temperatrue range, especially for PCMs. In the melting temperature range, with the latent heat functioning, the MPCM has huge potential to mamnage the battery temperature in a desired range with enhanced heat transfer between the PCM core and the battery heat generation, which could accelerate the heat rejection from the battery. Moreover, with PCM research development, higher heat capacity of MPCM poweder and slurry is expected to further increase the MPCM applicability in BTM, as more heat is removed within unit coolant. Besides, the improvement of the experimental setting could be achieved with more compatible accessories such as pump, pipe, flow meter and differential pressure sensor.

Chapter 5. Ansys modelling of PCM BTM

5.1 Introduction

The BTM system was simulated in this chapter with the utilization of ANSYS. The cooling module was the main simulation target, and the normally used aluminium plate in the battery cooling module was further substituted by the FSPCM studied in Chapter 3, aiming to enhance the cooling performance. Moreover, both of water and the MPCM slurry investigated in Chapter 4 were used as cooling fluid. These numerical investigations were conducted to further predict the BTM performance influenced by various thermal management methodologies.

5.2 Methodology

5.2.1 Geometry design

The experimental setup for evaluating the designed BTMS was shown in Fig. 4.2, Chapter. 4. According to the selected cells and design, the battery pack size, power, heat generation were determined, with the specification stated in Tab. 4.2, Chapter. 4. The equations for calculation of thermal conductivities, specific heat capacities and other thermal properties were listed in Chapter. 3.

The 3-dimensional geometry of the battery cooling module is illustrated in Fig. 5.1, corresponding to the experimental tested battery cooling module in Fig. 4.4 and Fig. 4.5, Chapter. 4. The cooling fluid media, water or MPCM slurry, goes from the inlet, through the pipe, and exits from the outlet. The cooper pipe (in grey) was fixed inside the cooling basement with S-shape to increase the heat exchange surface area. The cooling basement (in red) could be made by either aluminium, or the FSPCM, in a symmetric shape. The battery was simulated in cuboid geometry in dark blue.

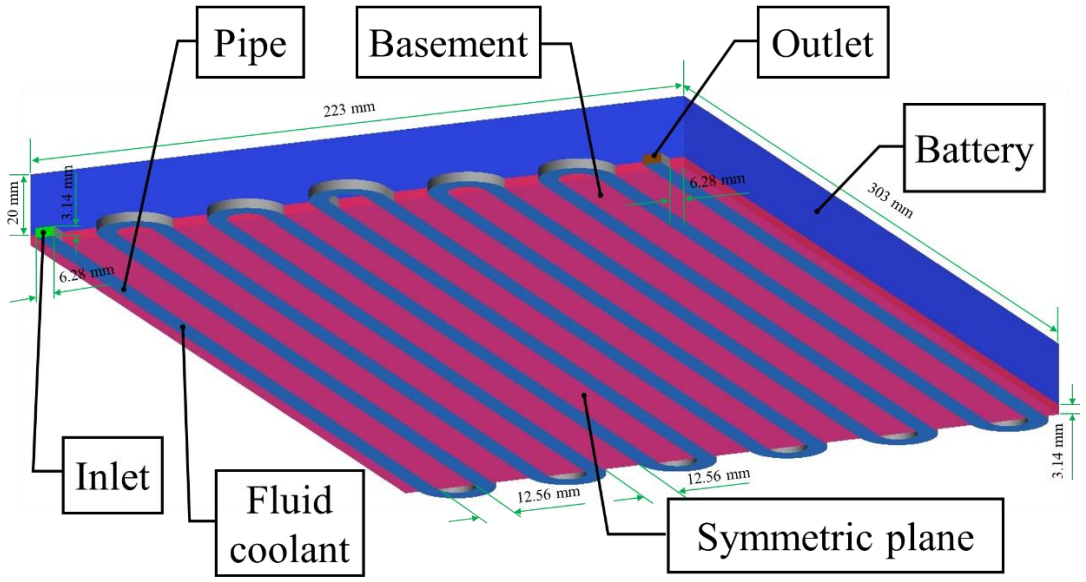

Fig. 5.1 3-dimensional geometry of the battery cooling module.

Fig. 5.2 showed the battery heat source modelled in the numerical simulation. The battery heat source was assumed to be a cuboid in the central of the battery. The volume of the simulated battery heat source cube was 0.00015 m^3.

- In the model validation with water coolant (Al-basement) and in the mesh sensitivity analysis, C-rate was 2C, corresponding to the volumetric heat generation of 490000 w/m^3.
- In the model validation with 10% MPCM slurry coolant (Al-basement), C-rate was 5C, corresponding to the volumetric heat generation of 1195378 w/m^3.
- In transient analyses, C-rates of 3C, 5C and 10C were tested, corresponding to the volumetric heat generation of 717227 w/m^3, 1195378 w/m^3, and 2390756 w/m^3, respectively.

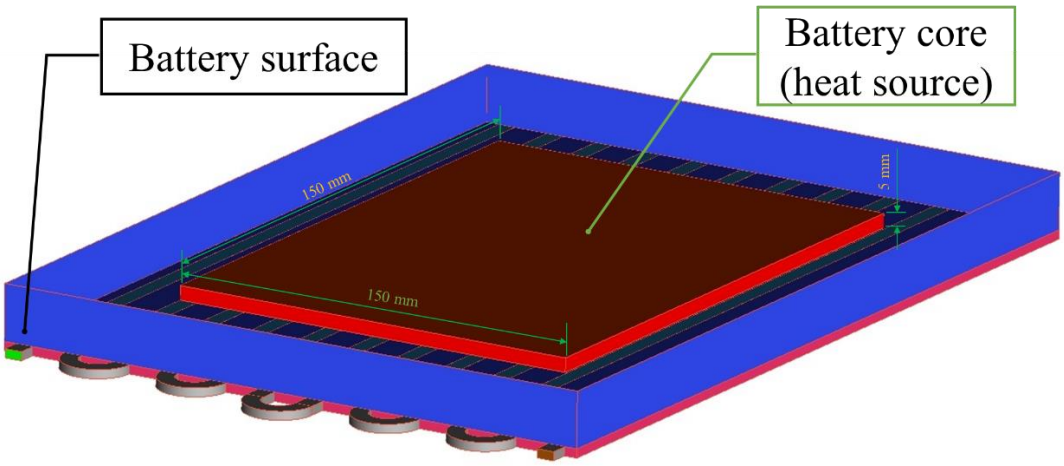

Fig. 5.2 The schematic diagram of battery heat source in the model.

5.2.2 Governing equations

The model used in this chapter was Shear-stress Transport (SST) *k-ω* model embedded in Ansys.

The flow equation was baseline (BSL) *k-ω* model, as expressed in Equation 5.1 and Equation 5.2 [155],

$$\frac{\partial}{\partial t}(\rho k)+\frac{\partial}{\partial x_i}(\rho k u_i)=\frac{\partial}{\partial \mathrm{x_j}}\left(\Gamma_k \frac{\partial k}{\partial \mathrm{x_j}}\right)+G_k-Y_k+S_k \qquad 5.1$$

$$\frac{\partial}{\partial t}(\rho \omega_k)+\frac{\partial}{\partial j}(\rho k u_j)=\frac{\partial}{\partial x_j}\left(\Gamma_\omega \frac{\partial \omega}{\partial x_j}\right)+G_\omega-Y_\omega+D_\omega+S_\omega \qquad 5.2$$

where t is the time. ρ is the density. The character k and ω are respectively the turbulence kinetic energy and the dissipation rate of k. The terms x_i and x_j are axial coordinates. The terms u_i and u_j are velocity components. Γ_k and Γ_ω are respectively the effective diffusivity of k and ω, expressed in Equation 5.3 and Equation 5.4, respectively. G_k is the production of the turbulence kinetic energy, which is exactly defined the same as it is in the standard *k-ω* model. G_ω is the ω-generation. Y_k and Y_ω are respectively the dissipation of k and ω because of the turbulence. D_ω stands for the

cross-diffusion term. S_k and S_ω are user-defined source terms.

$$\Gamma_k = \mu + \frac{\mu_t}{\sigma_k} \quad 5.3$$

$$\Gamma_\omega = \mu + \frac{\mu_t}{\sigma_\omega} \quad 5.4$$

where μ was the fluid viscosity. σ_k and σ_ω are, respectively, the Prandtl number for k and ω, determined by the distance to surfaces and cross-diffusion. μ_t is calculated by Equation 5.5.

$$\mu_t = \frac{\rho k}{\omega} \cdot \frac{1}{\max\left(\frac{1}{\alpha^*}, \frac{SF_2}{a_1 \omega}\right)} \quad 5.5$$

where S is the strain rate magnitude. α^* is a coefficient, which was determined by k, ω, μ, and ρ, when it is in the low-Reynolds number condition. Otherwise, α^* is 1 when it is in the high-Reynolds number condition.

G_k and G_ω could be calculated by Equation 5.6 and Equation 5.7, respectively.

$$G_k = -\rho \overline{u_i' u_j'} \frac{\partial u_j}{\partial x_i} \quad 5.6$$

where u_i' and u_j' are the fluctuation components of velocity. The symbol $\bar{}$ meant the time averaged components.

$$G_\omega = \frac{\alpha \alpha^*}{v_t} G_k \quad 5.7$$

5.2.3 Boundary conditions

Corresponding to the computational domain, Fig. 5.1, the boundary conditions were confined as follows:

- Inlet – The inlet velocity was set to 0.5 mL/min or 0.35 mL/min according to the testing group (Chapter 4) as listed in Tab. 5.1. The static fluid temperature at the inlet was set to 307 K.
- Interaction walls – The outside tube wall temperature was the same temperature with the cooling basement (Al or the FSPCM). The inside tube wall temperature was calculated according to the heat transfer equations.
- Wall between the battery and the cooling module – This wall temperature was the same with the battery inner surface temperature, according to the battery heat generation conditions.
- Outer wall – These walls were regarded as stationary adiabatic walls.

Tab. 5.1 The modelling groups.

	Basement	Mass fraction (%)	C-rate	Volume flow rate (mL/min)
1	Al	10	3C	0.35/0.5
2	Al	10	5C	0.35/0.5
3	Al	10	10C	0.35/0.5
4	Al	5	5C	0.35
5	PCM	10	3C	0.35/0.5
6	PCM	10	5C	0.35/0.5
7	PCM	10	10C	0.35/0.5
8	PCM	5	5C	0.35

5.3 Pre-simulation

5.3.1 Mesh sensitivity

The numerical model of the designed BTM was tested for the mesh sensitivity. Al was used as the main body of the battery cooling module. Water was employed as the cooling fluid, while C-rate was set to 2C. Mesh 1-4 respectively represented mesh numbers of 1534567, 2832701, 7140009, and 13326566, as shown in Fig. 5.3 to Fig. 5.6, corresponding to the global element sizes of 2.5 mm, 2.0 mm, 1.5 mm, and 1.0 mm.

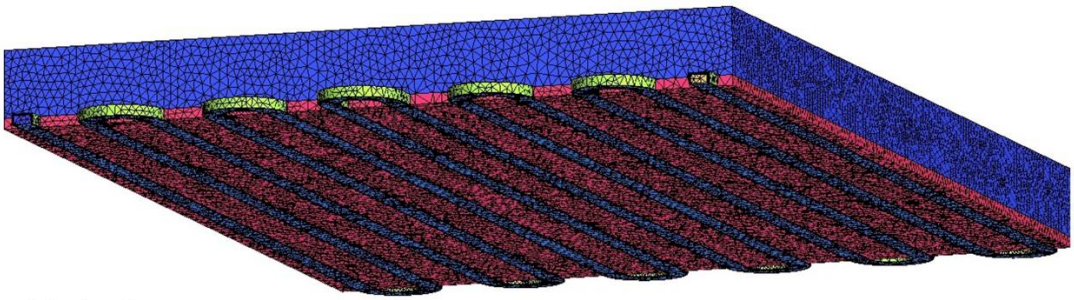

Mesh - 1
- Global element size – 2.5 mm
- Element number – 1534567

Fig. 5.3 The unstructured tetra meshing performed in the BTMS cooling module with a mesh number of 1534567.

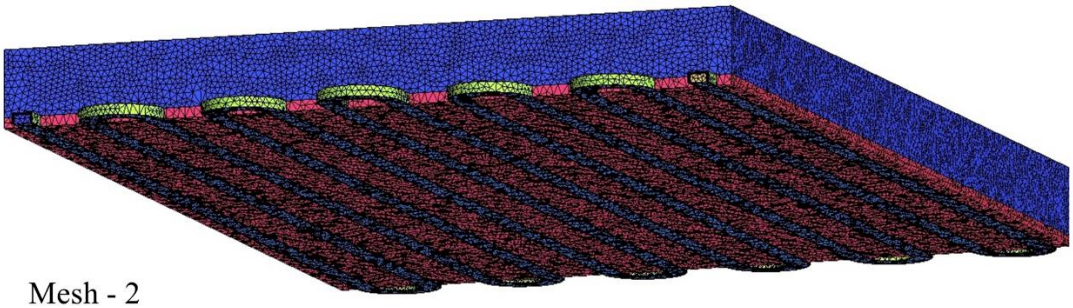

Mesh - 2
- Global element size – 2 mm
- Element number – 2832701

Fig. 5.4 The meshing performed in the BTMS cooling module with a mesh number of 2832701.

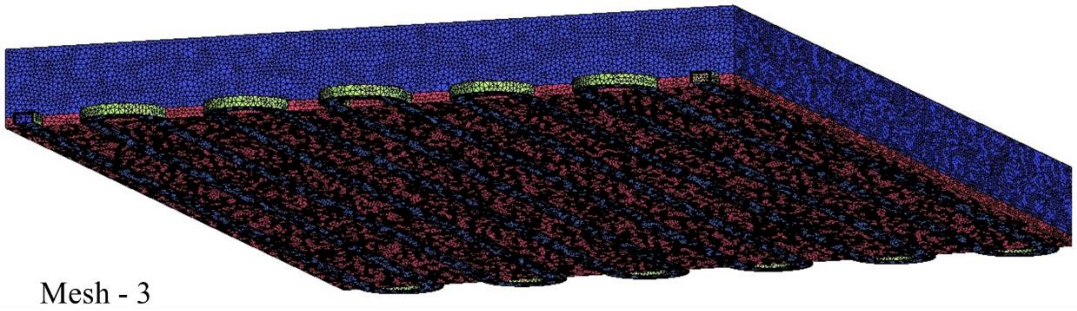

Mesh - 3
- Global element size – 1.5 mm
- Element number – 7140009

Fig. 5.5 The meshing performed in the BTMS cooling module with a mesh number of 7140009.

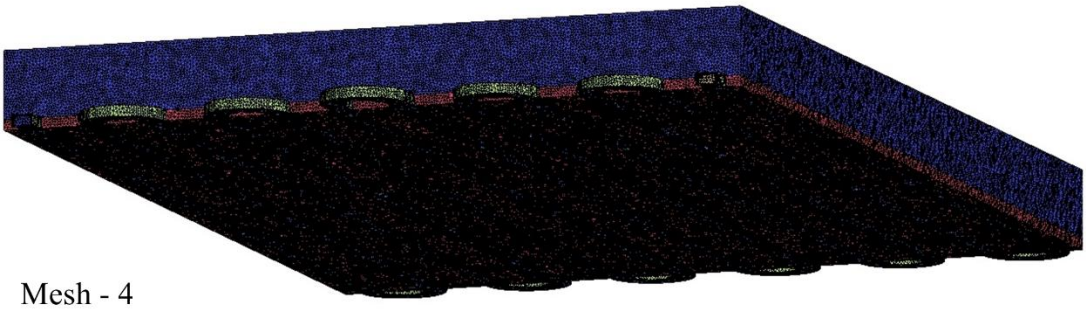

Mesh - 4
- Global element size – 1 mm
- Element number – 13326566

Fig. 5.6 The meshing performed in the BTMS cooling module with a mesh number of 13326566.

Fig. 5.7 illustrated the mesh validation of T_{out}, the temperature at the outlet (same with the experimental chapter), using the coded ANSYS model. When the experimental T_{out} was 290.78 K, the modelling result of T_{out} was in the range of 290.05 K to 290.16 K. The difference between the simulation and experiment result were further analysed in the next sector, while the mesh-determined difference was discussed in this section. It was obvious that Mesh 1-4 led to very similar T_{out} results with error less than 1.16 %. The minimum between the candidates was found to be Mesh 4, 1.13 %.

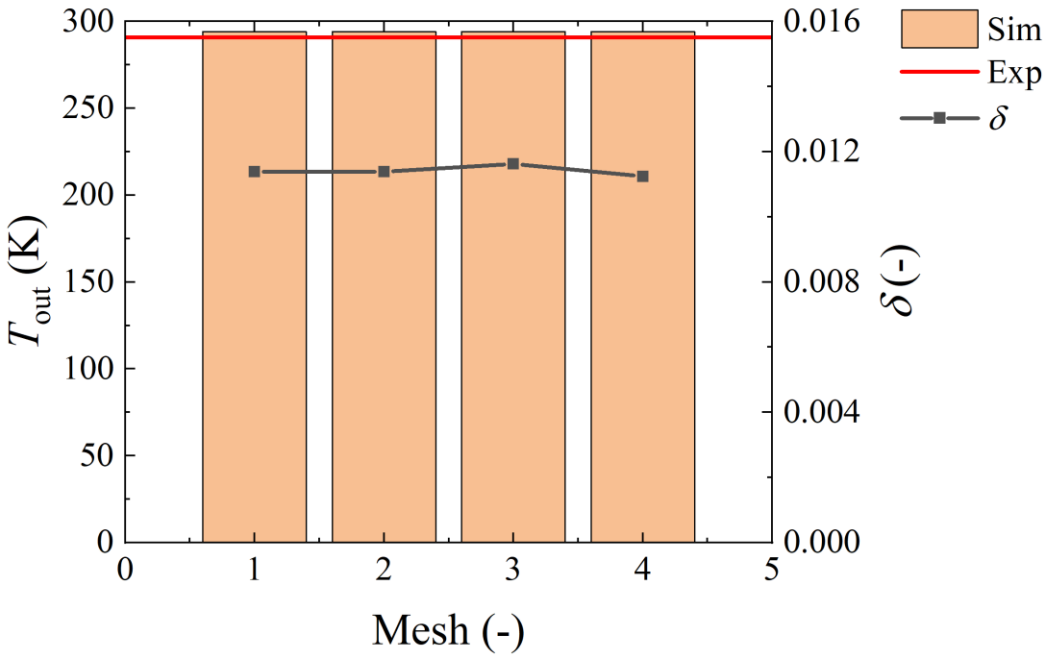

Fig. 5.7 Mesh sensitivity of T_{out}.

Fig. 5.8 exhibited the mesh validation of T_{cor}, the core temperature of the battery pack (same with the setting in Chapter. 3 and Chapter. 4), under the same circumstance of that in Fig. 5.7. The difference between the experimental and numerical T_{cor} was relatively and slightly larger than that for T_{out}. The error of T_{cor} was within 2.21 % and 2.62 %. When the experimental data of T_{cor} retrieved from Chapter. 4 was 307.04 K, the simulation result of T_{cor} could vary from 299.01 K to 300.25 K, which were lower than experimental data. The reasons could be various. The most possible one should be that the heat transfer between the coolant and the battery heat source was in a theoretical condition which was better than that in the practical experiment, thus the battery temperature was further controlled to a lower level. Besides, the position of the thermocouple inside the battery in the experimental setting could also raise discrepancy between the simulation and the reality. However, T_{cor} was still in a reliable range. Mesh 2-3 have similar results.

To balance the precision of the numerical results and the computational calculation complexity, Mesh 3 (mesh number of 7140009) was fixed in the following simulations. In this case, the error for T_{out} and T_{cor} were respectively 1.16% and 2.54%, which was still highly reliable for the further analysis.

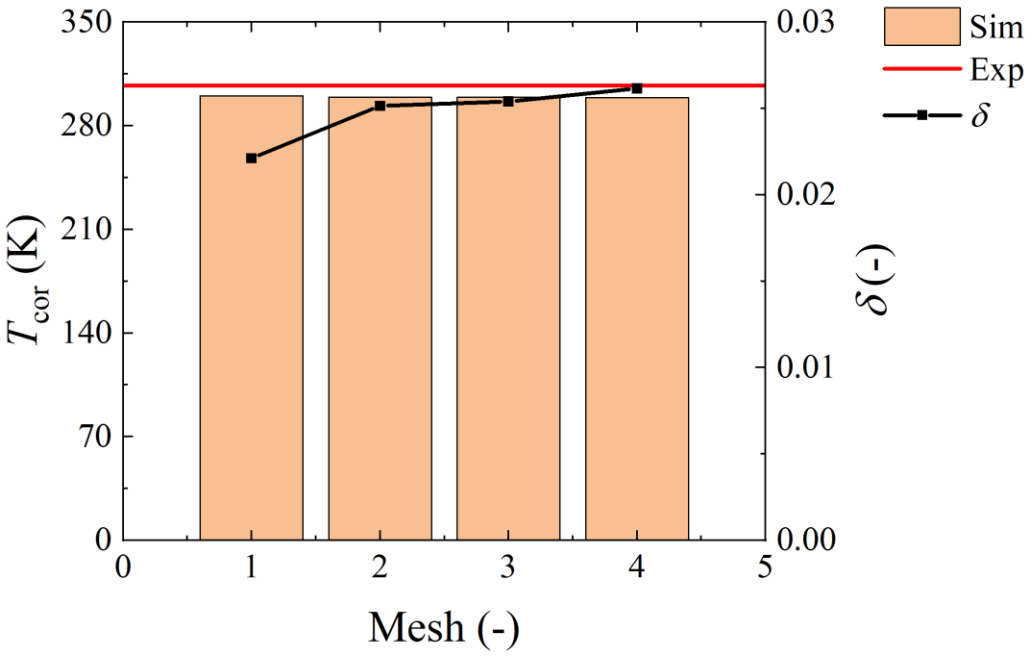

Fig. 5.8 Mesh sensitivity of T_{cor}.

5.3.2 Model validation

The corresponding voltages towards C-rate of 1C, 2C, 3C, 4C, and 5C were 74V, 105V, 127V, 147V, and 164V. These values were calculated according to Equation 3.19, which represented the heat generation rate of the EV battery packs. The corresponding t_C could be calculated if interested, by Equation 3.7. Condition 1-5 represented C-rate was 1C-5C, when the water was employed as the cooling fluid. Condition 6 stood for the condition in which the 10% MPCM slurry was employed as the cooling flow, when C-rate was 5C. The validation conditions were summarized in Tab. 5.2.

Tab. 5.2 The validation conditions.

Condition	C-rate	Cooling medium
1	1C	Water
2	2C	Water
3	3C	Water
4	4C	Water
5	5C	Water
6	5C	10% MPCM slurry

Fig. 5.9 presented the validation result of T_{out}, which represented the outlet temperature of the cooling medium. The results demonstrated that the experimental data and the numerical results were very close as the error was no higher than 3.5%. With the increment of C-rate, the error of T_{out} was increased but still in a reliable range. The maximum discrepancy between the experimental and simulated data was found in Condition 5 (C-rate was 5C), 3.29%. The minimum error was found in Condition 1 (C-rate was 1C), 0.31%. Substituting the cooling fluid by 10% MPCM slurry, the error between the experimental and simulated results was 2.37%.

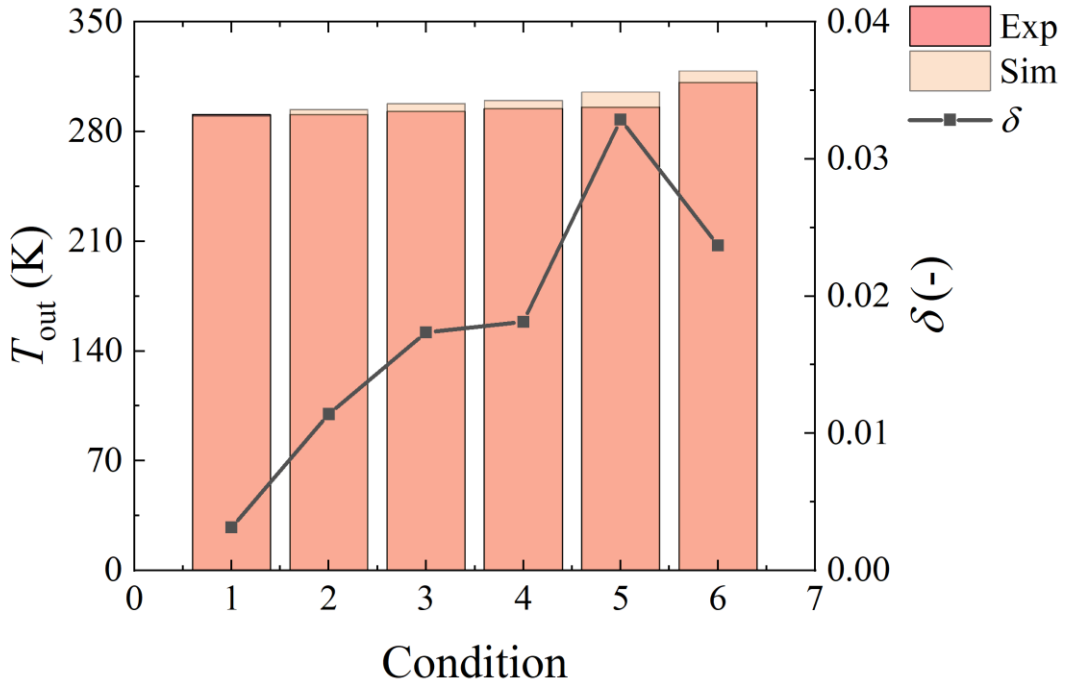

Fig. 5.9 Model validation of T_{out}.

Fig. 5.10 was the model validation results of T_{cor}, which reflected the temperature of the core in the battery package. As presented in the figure, with C-rate ranging in 1C-5C, the error of T_{cor} was less than 7%, which showed the good agreement between the simulating model with the practical experiments of BTMS. The minimum error among all was found in Condition 2 (C-rate was 2C), 1.84%, while the maximum discrepancy was discovered in Condition 5 (C-rate was 5C), 6.47%. Replacing water by 10% MPCM slurry in the modelling, the error was 4.42%.

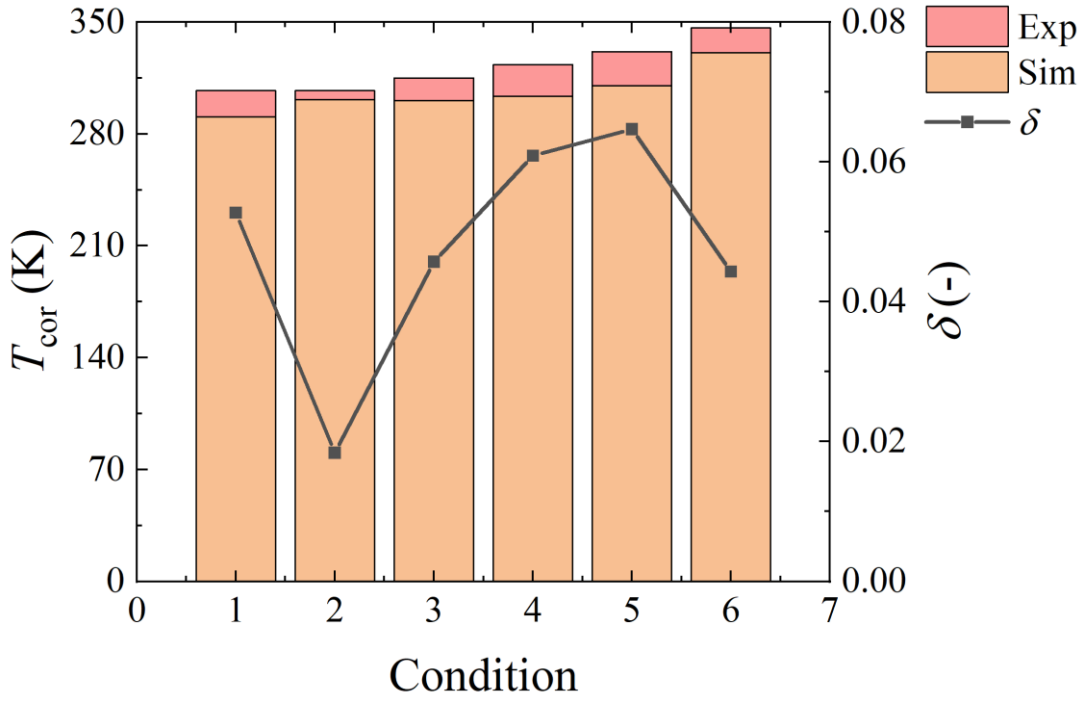

Fig. 5.10 Model validation of T_{cor}.

These validation results demonstrated that the numerical model of the designed BTM was reliable. The error between the experiment and the simulation could be that, in practice, the insulation could be limited, and heat loss happened inevitably. Furthermore, the insulation could be limited, and heat loss happened inevitably. In a summary, the difference between the reality and the theoretically serious governing such as the experimental error all contributes to the error between the experiment and the modelling. As long as the result was confined in the tolerance, the model could be regarded as acceptable.

5.4 Al basement

5.4.1 Influence of C-rate

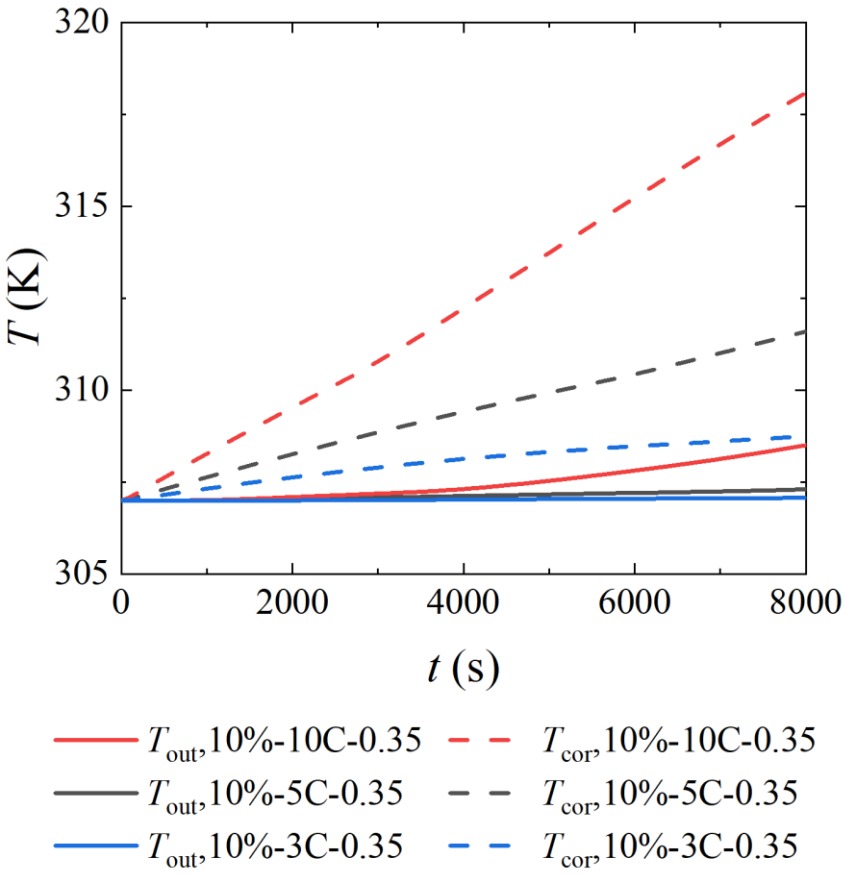

Fig. 5.11 T_{out} and T_{cor} *vs*. r_Cs, Al basement, 10% MPCM slurry, v_0 = 0.35 mL/min

Fig. 5.11 shows the performance of BTM system influence by alteration of C-rates between 10C and 3C, using the volume flow rate of 0.35 mL/min and the basement of Al. T_{out} is represented by solid line and T_{cor} is stood by dash line. It is noticed that T_{out} and T_{cor} increase with time evolution, and they also increase with the C-rate increasing. At the start of 0 s, they were at the same temperature, 307 K. This start point was set according to the experiments conducted in Chapter. 4. At the end of 8000 s, the maximum temperature is always found to be with C-rate of 10C. The maximum T_{out} and T_{cor} are respectively 308.50 K and 318.09 K. Interestingly, the unique temperature profile of a platform-shape is not observed in the figure, as under these simulation scenarios, the T_{cor} was too low to melt the core PCM.

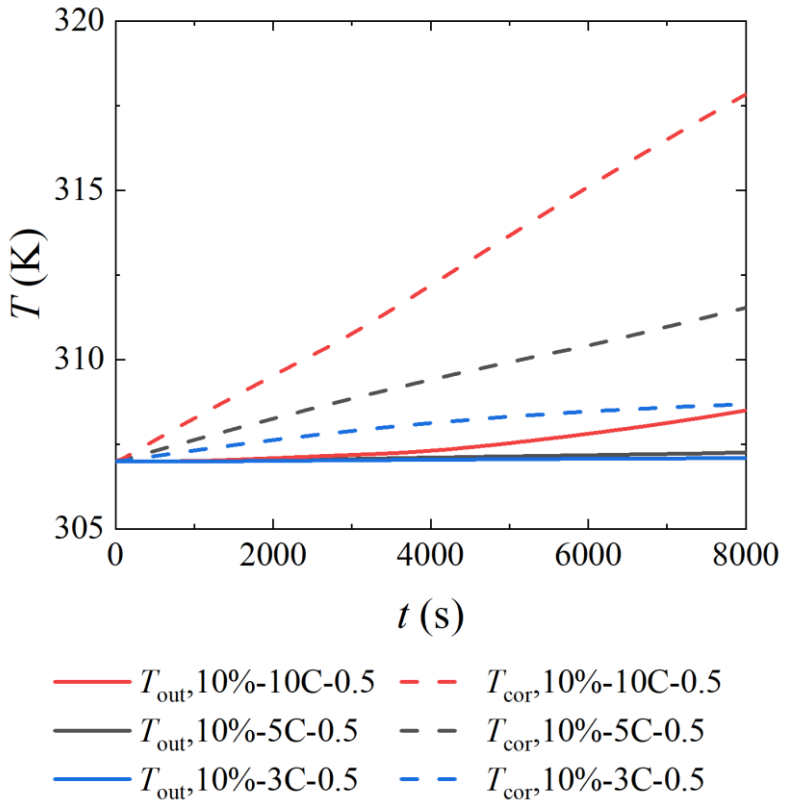

Fig. 5.12 T_{out} and T_{cor} vs. C-rates, Al basement, 10% MPCM slurry, v_0 = 0.5 mL/min

Fig. 5.12 is the result that compared the BTM performance with different C-rates between 10C and 3C, when the Al-basement and the volume flow rate of 0.5 mL/min were set as the simulation condition. Again, it is found that T_{out} and T_{cor} were enlarged with the C-rate increasing. This is because that a high C-rate could increase the gross heat generation both in the scale and the rate. At the end of 8000 s, the maximum temperature was always found to be with C-rate of 10C. The maximum T_{out} and T_{cor} are respectively 307.26 K and 311.54 K. It is easy to understand that the core temperature inside the battery accumulate the thermal energy and thus show a higher temperature than that of the outlet coolant, considering that the limited heat absorbed by the flowing cooling fluid.

5.4.2 Influence of coolant flow rate

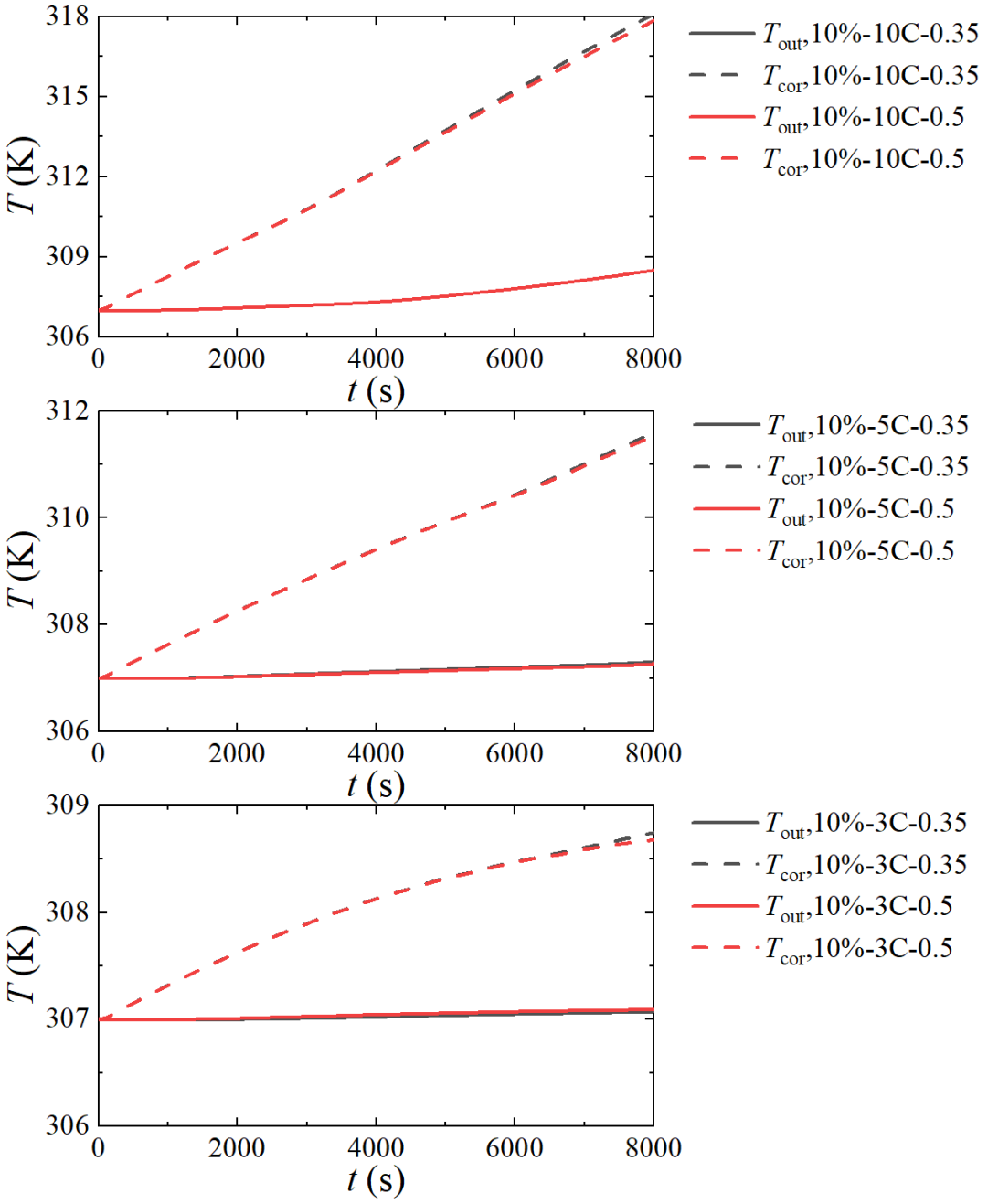

Fig. 5.13 T_{out} and T_{cor} versus different water volume flow rate, v_0, using an Al-basement.

Fig. 5.13 is the result of the BTM performance influenced by the volume flow rate varying from 0.5 mL/min to 0.35 mL/min, applying a basement made by aluminium in the cooling module. It is found that T_{out} and T_{cor} have limited fluctuations during the switching of the water volume flow rate. At the end of 8000 s, T_{cor} can still decrease a little bit, compared to smaller water volume flow rate. Corresponding to C-rate of 10C, 5C, and 3C, the decrease of T_{cor} at the end of 8000 s are respectively 0.08%, 0.02%,

and 0.02%. These results indicate that in these modelling conditions, the increment of 0.15 mL/min could only influence very limit on the battery cooling effect. This is because that the heat transfer coefficient, K (similarly as it is in Equation 3.8), enhanced by the enlarged coolant volume flow rate is limited. Moreover, the exchanged thermal energy should be increased by enhancing the heat transfer between the coolant and the battery wall or enlarging the heat exchanging surface area to reduce the difference between T_{cor} and T_{out}. In this case, more accumulative heat could be removed from the core battery, and both the battery safety and performance could be thus improved.

5.4.3 Influence of MPCM mass ratio

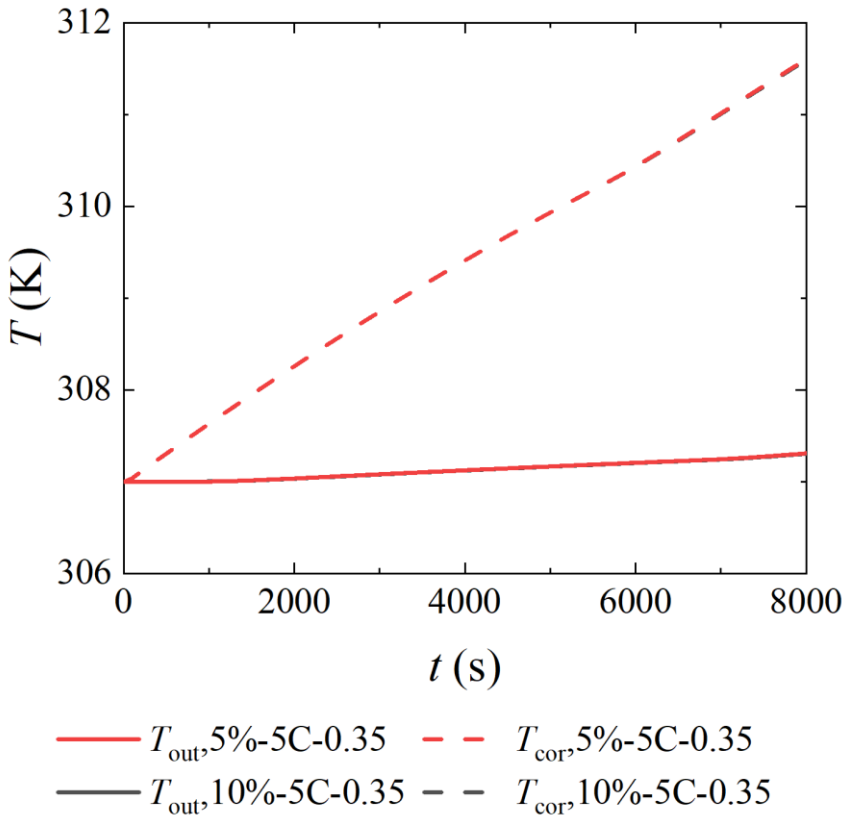

Fig. 5.14 T_{out} and T_{cor} vs. MPCM slurry mass ratios, using an Al-basement.

Fig. 5.14 is the simulation results comparing the different mass ratios used in the MPCM slurry. It is almost the same when 5% and 10% MPCM slurry mass ratios are employed in the BTMS performance tests. This may be due to the unreached optimal

MPCM working temperature. The results demonstrate that the mass ratio of the MPCM can be low to reduce the BTM capital costs, given that the mass ratio seemed no influence on the battery cooling effect in these simulating circumstances.

5.5 FSPCM basement

5.5.1 Influence of C-rate

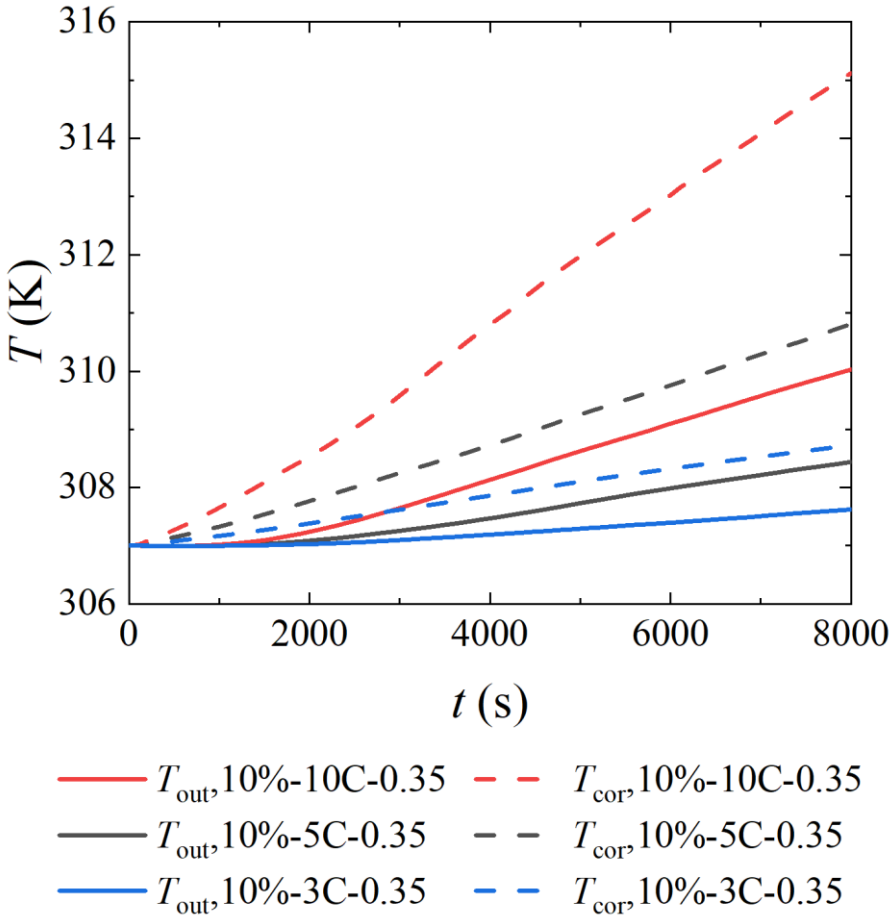

Fig. 5.15 T_{out} and T_{cor} vs. C-rates, FSPCM basement, 10% MPCM slurry, v_0 = 0.35 mL/min

Fig. 5.15 presents the BTM performance altering C-rates between 10C and 3C with the volume flow rate of 0.35 mL/min and the basement of the FSPCM, which has been discussed in Chapter. 3. It is demonstrated that T_{out} and T_{cor} increased with time evolution, and they also increase with the C-rate increasing. The reason has been discussed in 5.4.1. At the end of 8000 s, the maximum temperature is always found to

be with C-rate of 10C, represented in red. The maximum T_{out} and T_{cor} are respectively 310.03 K and 315.12 K.

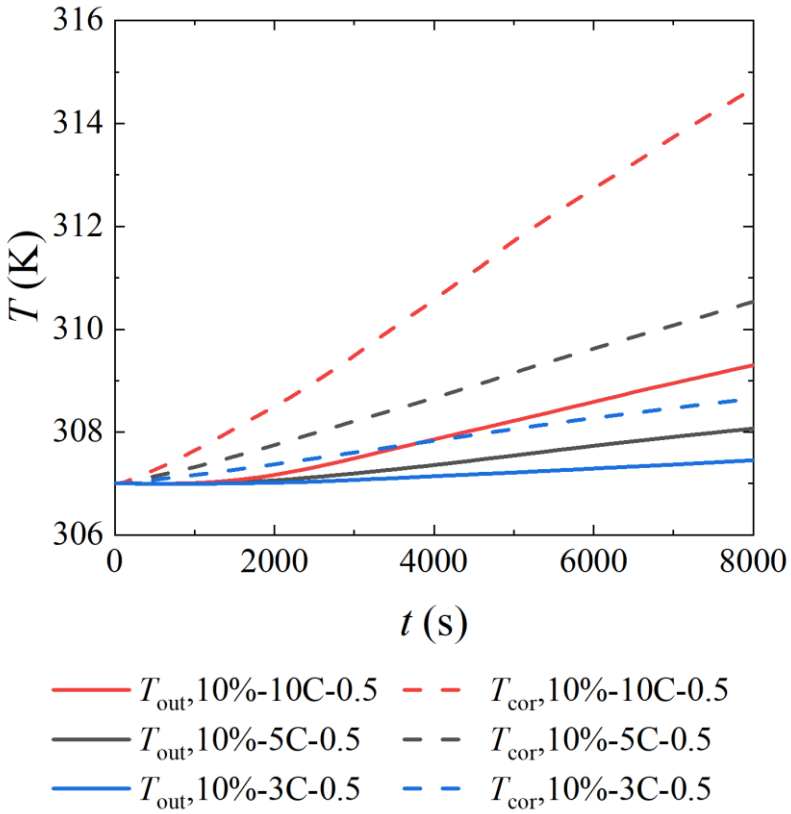

Fig. 5.16 T_{out} and T_{cor} vs. C-rates, FSPCM basement, 10% MPCM slurry, v_0 = 0.5 mL/min

Fig. 5.16 exhibits the BTM performance influenced by various C-rates between 10C and 3C, with the FSPCM-basement and the volume flow rate of 0.5 mL/min. Again, it was found that T_{out} and T_{cor} increased with the C-rate increasing. At the end of 8000 s, the maximum temperature at the same point was always found to be with C-rate of 10C. The maximum T_{out} and T_{cor} were respectively 309.30 K and 314.68 K.

5.5.2 Influence of coolant flow rate

Fig. 5.17 compares the numerical result of the BTM performance effected by the volume flow rates of 0.50 mL/min and 0.35 mL/min, employing the FSPCM-basement in the cooling module. It is found that T_{out} and T_{cor} have small decrements during the switching of the volume flow rate from 0.35 mL/min to 0.50 mL/min. The increased

volume flow rate could change the flow condition (reflecting on parameters such as *Re*) which could enhance the heat transfer coefficient, *K*, and thus improve the BTM performance. Corresponding to C-rate of 10C, 5C, and 3C, the decrease of T_{cor} at the end of 8000 s were respectively 1.40%, 0.09%, and 0.03%. These results indicate that in the modelling with a FSPCM-basement, the increment of 0.15 mL/min could have larger influence on the battery cooling effect, compared to the BTM system employing an Al-basement.

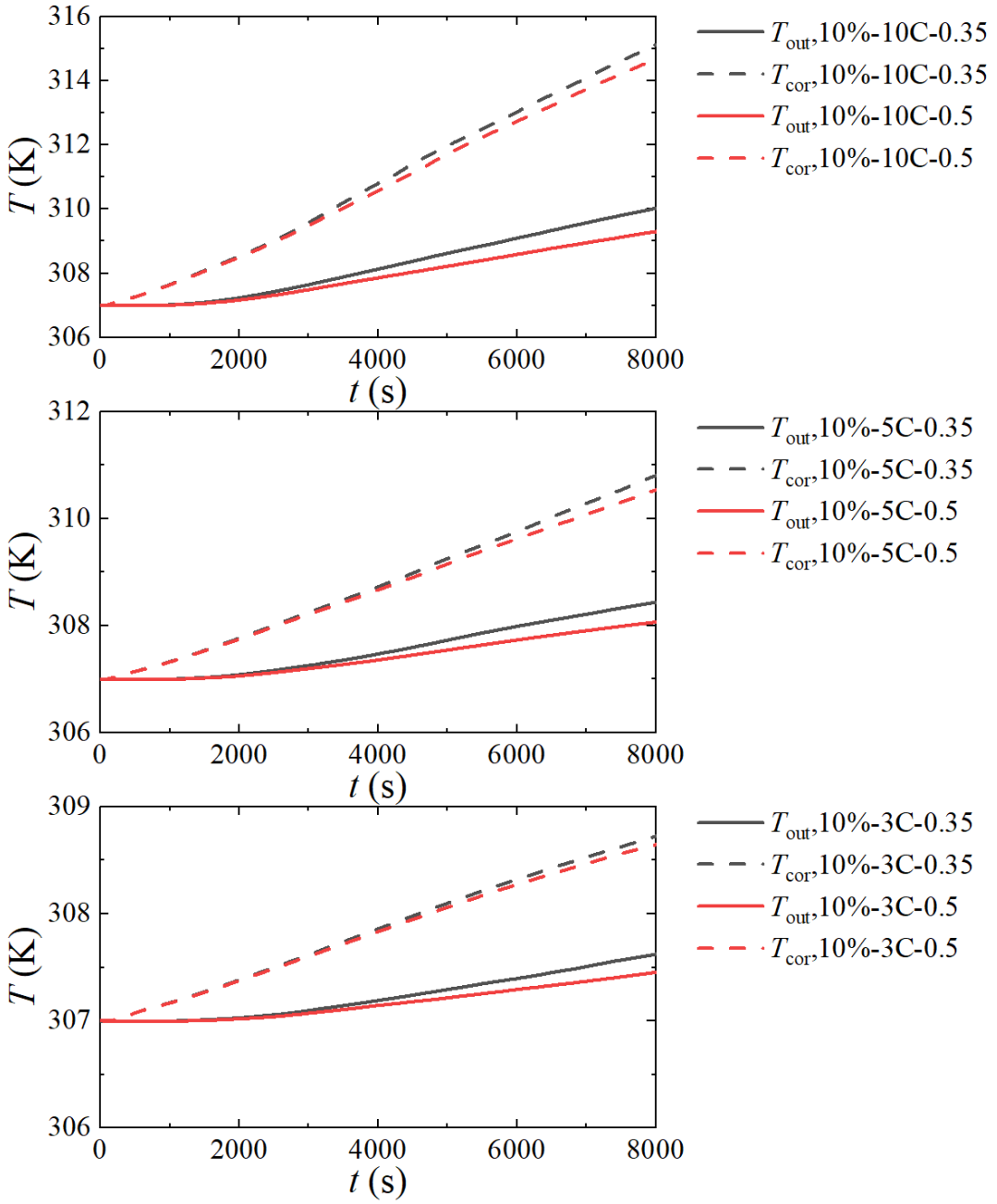

Fig. 5.17 T_{out} and T_{cor} vs. different volume flow rate, v_0, using a basement of FSPCM.

5.5.3 Influence of MPCM mass ratio

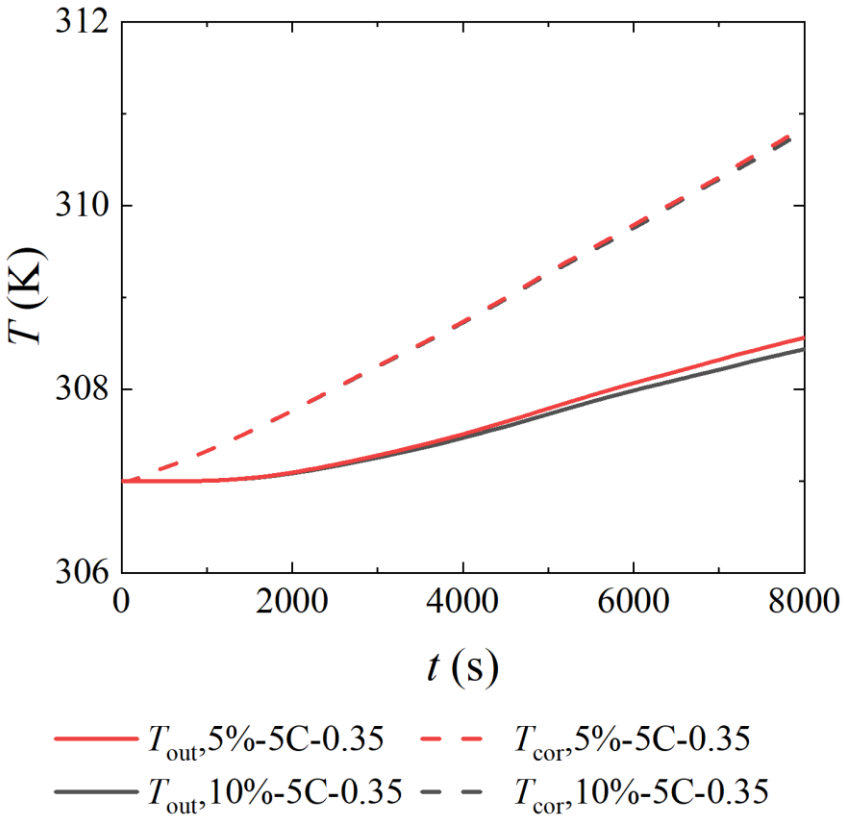

Fig. 5.18 T_{out} and T_{cor} vs. MPCM slurry mass ratios, using a FSPCM-basement.

Fig. 5.18 shows the simulation results comparing the different mass ratios used in the MPCM slurry. It was found that when MPCM slurry mass ratio increased from 5% to 10%, the BTMS performance is slightly improved. T_{out} and T_{cor} are reduced by 0.04% and 0.02%. The results demonstrated that increasing the mass ratio of the MPCM slurry can improve the BTMS performance in these tested simulating circumstances. The increased MPCM mass ratio could enlarge the specific heat capacity of the MPCM slurry (the coolant), which potentially enhance the cooling ability of the MPCM BTM. The liquid fraction information of the core PCM could be directed read in the model, which could be referred in Appendix. C if interested.

5.6 Different basements

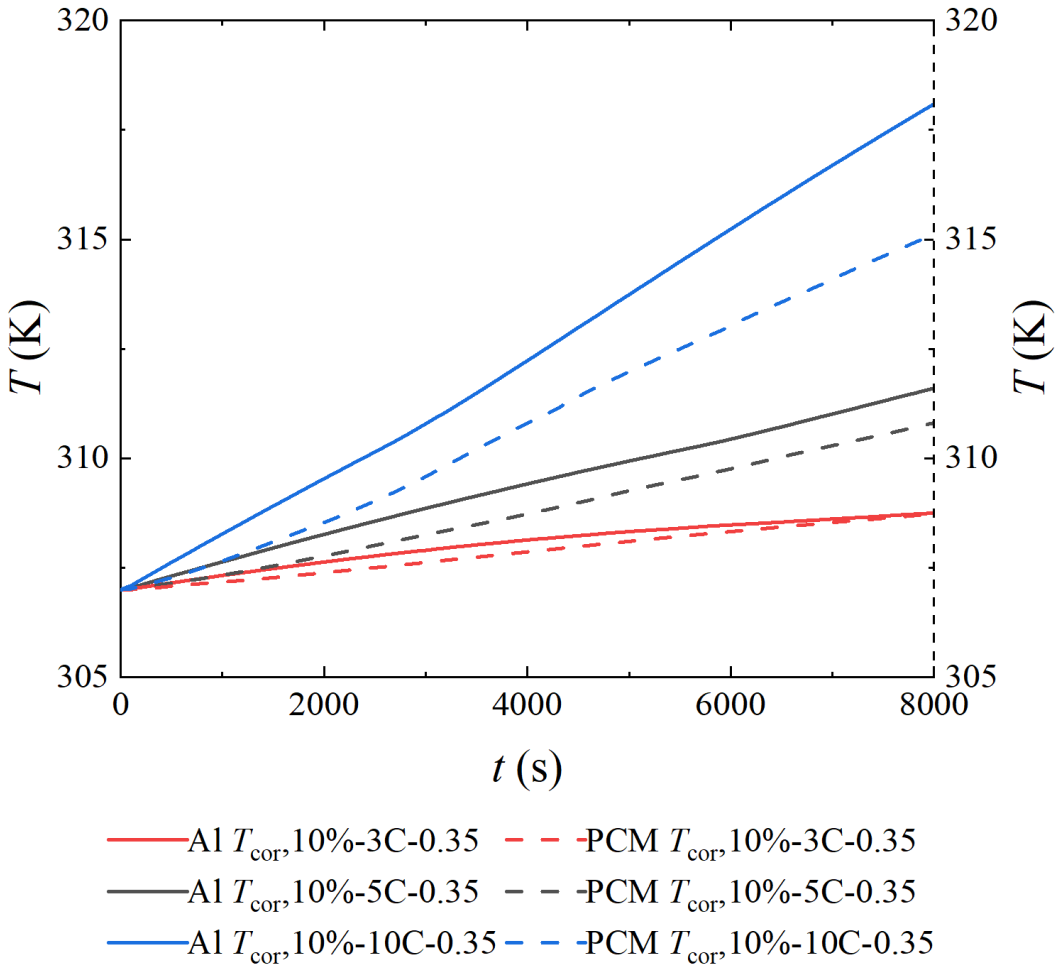

Fig. 5.19 T_{cor} *vs*. different basement and C-rates.

Fig. 5.19 is the T_{cor} profile versus Al/FSPCM-basements and different C-rates. As expected, T_{cor} of FSPCM-basement (in dashed line) is always below that of Al-basement (in solid line), when the other operational conditions are the same (in the same colour). The reduction of replacing aluminium by FSPCM is 0.94%, 0.25%, and 0.01%, respectively in the condition with C-rate of 10C, 5C, and 3C. It was demonstrated that the substitute of basement material from aluminium to FSPCM could improve the BTM performance, controlling the working battery temperature in a desired range when the heat was accumulated in the battery. Moreover, the higher C-rate could result in even larger improvement in respect of BTM performance, using the basement made by FSPCM.

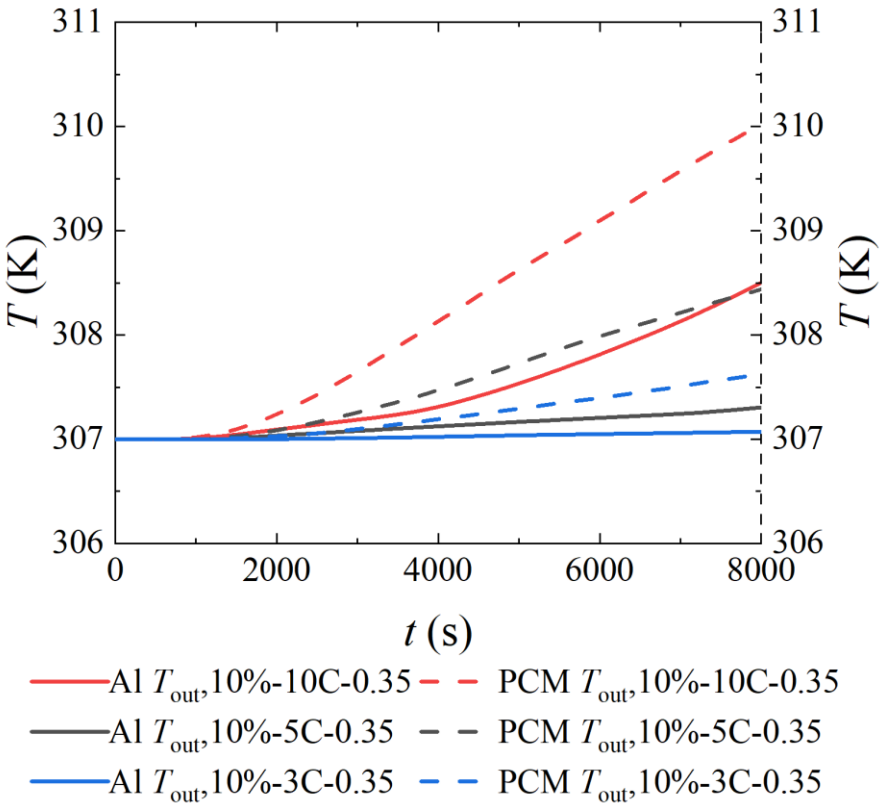

Fig. 5.20 T_{out} *vs*. different basement and C-rates, when v_0 was 0.35 mL/min.

Fig. 5.20 shows the simulating results comparing the different basement influences on the BTM performance, along with different C-rates. The MPCM slurry flow rate was 0.35 mL/min. The results show that FSPCM-basement generally located above the other candidate, meaning that Al-basement always proved a higher outlet coolant temperature. The T_{out} increased by replacing FSPCM-basement by Al-basement when C-rate is 10C, 5C and 3C at the MPCM slurry volume flow rate of 0.35 mL/min is by 0.49%, 0.37%, and 0.18%. These results demonstrate that in these designed simulation conditions, FSPCM-basement could exchange more heat with the battery and the coolant, thus the outlet coolant temperature grows, compared with that with Al-basement. The reason could be that, in this case, the PCM mixed in the matrix enhanced the heat transfer between the battery wall and the cooper coolant pipe.

5.7 Conclusion

In this chapter, ANSYS was used to simulate the BTM system. The geometry of the battery cooling module was built, the boundary conditions and the governing equations were rationally selected and set. The results can be summarized as follows:

- A high MPCM slurry volume flow rate can reduce T_{out} and T_{cor}, but it showed very limited influence when the basement was made of Al, due to the unreached optimal MPCM working temperature.
- High MPCM mass ratio has limited effect on BTM system performance using Al-basement, but it can slightly reduce the temperature increase using FSPCM-basement, which could be due to the temperature range (not in the optimal FSPCM working temperature range). Moreover, the heat transfer should be improved, between the FSPCM and the battery wall, or between the FSPCM and the coolant pipe.
- FSPCM-basement was more promising to be employed in the BTM system for a lower battery temperature, compared to Al-basement. It could be contributed by enhanced heat transfer between the battery and the coolant with the application of FSPCM-basement. The T_{cor} reduction of replacing aluminium by FSPCM is 0.94%, 0.25%, and 0.01%, respectively, in the condition with C-rate altered from 10C to 3C.

Chapter 6. Conclusions

6.1 Summaries of chapters

Electricity-driven vehicles, which use the battery as the power source, attract increasing research interests by reducing the demand of fossil fuel. However, the battery temperature can rapidly increase during charging, and thus negatively influence the Evs (Electric vehicles) and HEVs (hybrid electric vehicles) performance. BTM (battery thermal management) system, which can enhance the EVs and HEVs performance by controlling the battery temperature in the optimal working range, is important in the EV/HEV application.

This PhD project reseached on a potentially high-performance BTM system for battery used in EV/HEV, which integrated FSPCM (form stable phase material) and MPCM (micro-encapsulated phase change material) as the cooling fluid. The summary of Chapter. 1 to Chapter. 5 was listed below.

- Chapter. 1 – The background of this PhD project was introduced, which drove the author to conduct the BTM research with focus on the application of the FSPCM and MPCM. The aim and objectives were listed, and the structure of the thesis was revealed.
- Chapter. 2 – The literature was reviewed for BTM. EVs, HEVs, and FCEVs, regarded as an effective methodology to constrain the carbon footprint, require high power batteries, such as Li-ion, lead acid, and Ni-MH batteries. To achieve high power batteries for EVs and HEVs, BTM is inevitable. Four BTM systems have been introduced including air, liquid, PCM, and PEMFC BTMs. Their features, advantages and disadvantages are discussed. PCM BTM for EVs and HEVs is focused as it takes the advantage of the huge heat storage capacity. However, it suffers from the low thermal conductivity and the leakage during phase transition. With the addition of rationally-selected materials, the composite PCMs can be created to have high latent heat capacity and high thermal conductivity, exempting from leaking issues. One of these promising PCMs is the FSPCM, while the other is the MPCM. However, FSPCM and MPCM were barely utilized in the BTM system at the current research stage.
- Chapter. 3 – The FSPCM BTM was simulationally studied using MATLAB. The FSPCM was composed by paraffin (PA), expanded graphite (EG), and high

density polyethylene (HDPE). A one-dimensional numerical model was established and developed to comprehensively understand the working mechnics of FSPCM BTM. Four different scenarios were compared, including the blank group, FSPCM BTM, air-cooling BTM, and hybrid FSPCM-air BTM systems. The result demonstrated FSPCM to be a promising candidate for BTM. The optimal BTM was proved to be the integrated FSPCM with forced air convection BTM, which could maximally prevent the heat accumulation of battery (temperature reduction of 15.9 K). Besides, the optimal FSPCM parameters $r_{PCM\text{-}b}$ (thickness ratio between the FSPCM and battery) and ω_{EG} (mass fraction of EG in FSPCM) were proved to be 0.08 and 4.6 wt%, respectively. Moreover, higher air velocity was preferred at a low r_C (C-rate).

- Chapter. 4 – The MPCM BTM was experimentally investigated. A BTM system test rig was established. The basement of the cooling plate was made by aluminum, while the coolant pipe of the plate was made by cooper. The cooling fluid tested included the MPCM slurry and water. The functional PCM was micro-encapsulated in a metal shell to form the MPCM particle, which prevents the PCM leakage and still keeps its high thermal storage capacity. Mixing the MPCM particle with water in a ratio could produce the MPCM slurry used in this experimental test. The result revealed that the optimal working area was determined by the core PCM melting temperature, which should be carefully considered in the practical applicaion. In the confined test conditions, with r_C increasing, T_{cor} (core battery temperature) increased as well, with T_{cor} still controlled under 46.26 °C at a stable state. The maximum r_T (temperature changing rate) was 7.90 °C/s at t= 55 s, when r_C was 5C.

- Chapter. 5 – Both FSPCM and MPCM were integrated to eveluate the BTM performance using ANSYS. The BTM system was modelled as the same with the experimentally studied one in Chapter. 4. The coolant was either water or MPCM slurry, while the cooling basement could be made by aluminum or FSPCM. The result showed that the increment of v_0 (MPCM slurry volume flow rate) could reduce T_{out} and T_{cor}, but the improvement was very limited when the basement was made of Al. Moreover, a high ω_s (MPCM mass ratio) could only slightly restrain the thermal acumulation using FSPCM-basement. FSPCM-basement was more promising to be employed in the BTM system for a lower

battery temperature, compared to Al-basement. It could be contributed by enhanced heat transfer between the battery and the coolant with the application of FSPCM-basement. The T_{cor} reduction of replacing aluminium by FSPCM is 0.94%, 0.25%, and 0.01%, respectively, in the condition with C-rate altered from 10C to 3C.

In a summary, BTM with FSPCM and MPCM could decrease the battery temperature during the battery working period, demonstrating that they are potential technologies to control the battery temperature in a suitable working range. However, the selection of FSPCM and MPCM (category, mass ratio, ways to apply, and so on) should be carefully considered towards the working condition - especially the battery temperature range during working. The enhancement of heat transfer between the battery and the coolant and the improvement of heat capacity of the rationally manufactured FSPCM and MPCM are the two main aspects need to be further studied.

6.2 Future directions

During the experimental and simulational investigation of the FSPCM and MPCM BTM, some problems still remained to be solved. One prospect should be the experimental operation issue when MPCM slurry was employed in the BTM system. Due to the unevenly disstributed temperatures over the whole cooling module, the phase of the core PCM was hard to be determined, which meaned the differential pressure monitored based on several assumptions have impact on the gross accuracy (especially when predicting the viscosity of the real time MPCM slurry). Moreover, the high viscosity compatible pipeworks, connections, pump and flow meter used in this experiments seemed not efficient enough for this reason. Even though this was the best operational plan at the author's current acknowledge, the further researchers should consider these mentioned problems. Enhanced monitoring system and calibration methodology was suggested with more expenses expected. The other prospect should be the selection simulation scenarios. Given more computational time, the studied paramters could be more in both categories and ranges in value, even though some of the parameters may be not meaningful to practical application in batteries for EV/HEV, as these PCM (MPCM and FSPCM) could have wider utilization range towards thermal management and storage. This PhD project did not only provide researchers the

reported data, but also the useful models exploring PCM application on BTM with further user-defined settings, corresponding to the desired functions.

Besides, other thermal management for battery also develops fast, and one should always keep going on with up to date technologies. For exmaple, the heat pipe also attracts lots of interests due to its superconductive capability, which enables heat trasfer at a very low temperatrue gradients [156]. Majority studies of the heat pipe BTM using the conventional tubular heat pipes, flat heat pipes and flat-ended tubular heat pipes. Other heat pipe BTM technologies include oscillating/ pulsating heat pipes, and loop heat pipes. Neverthelss, the impact of transient heating conditions and multiple heat loads on the heat pipe performance have still been insufficiently investigated.

Appendix. A T_{cor} and T_{out} with water-cooling BTM

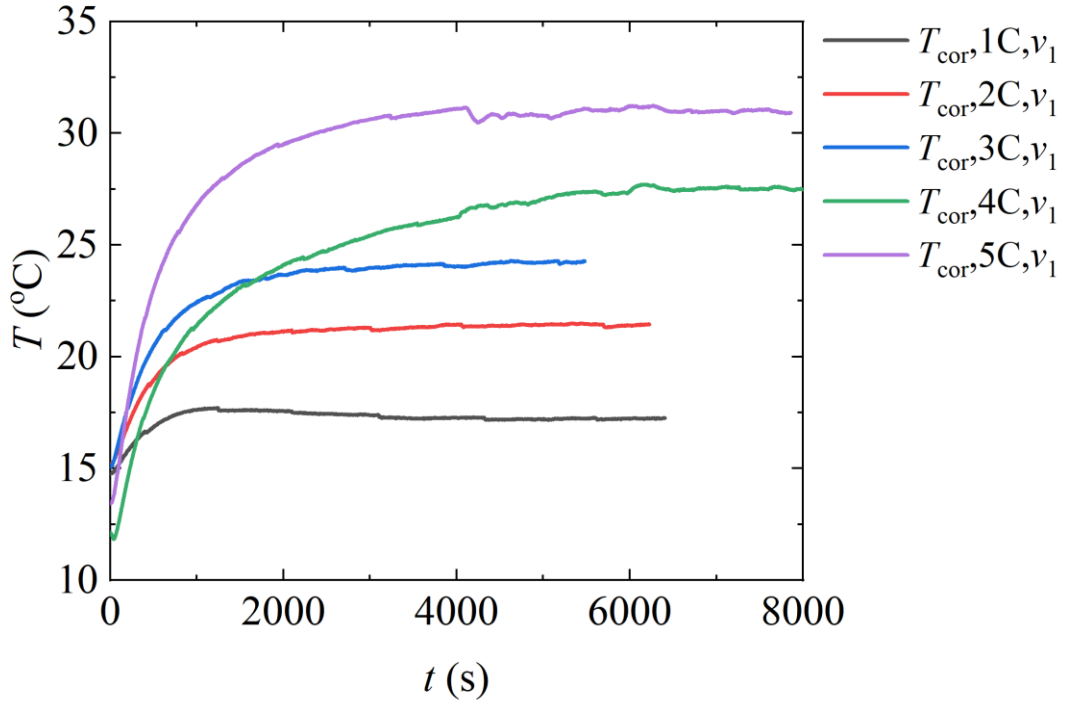

Figure. A1 Core battery temperature of water-cooling BTM with v_1

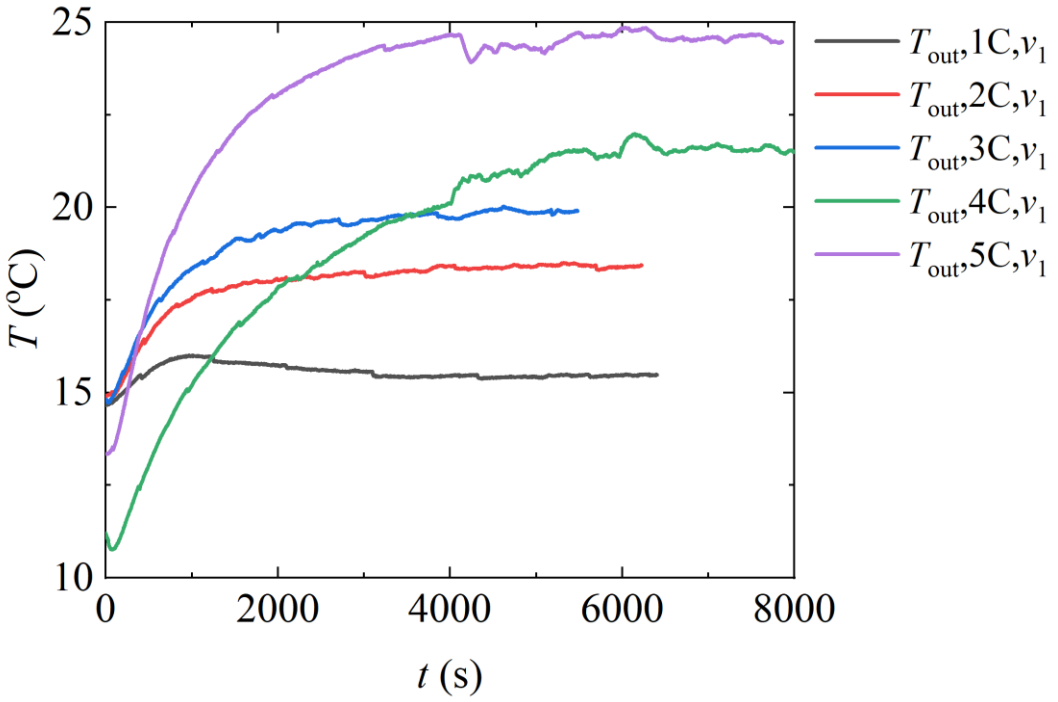

Figure. A2 Outlet water temperature of water-cooling BTM with v_1

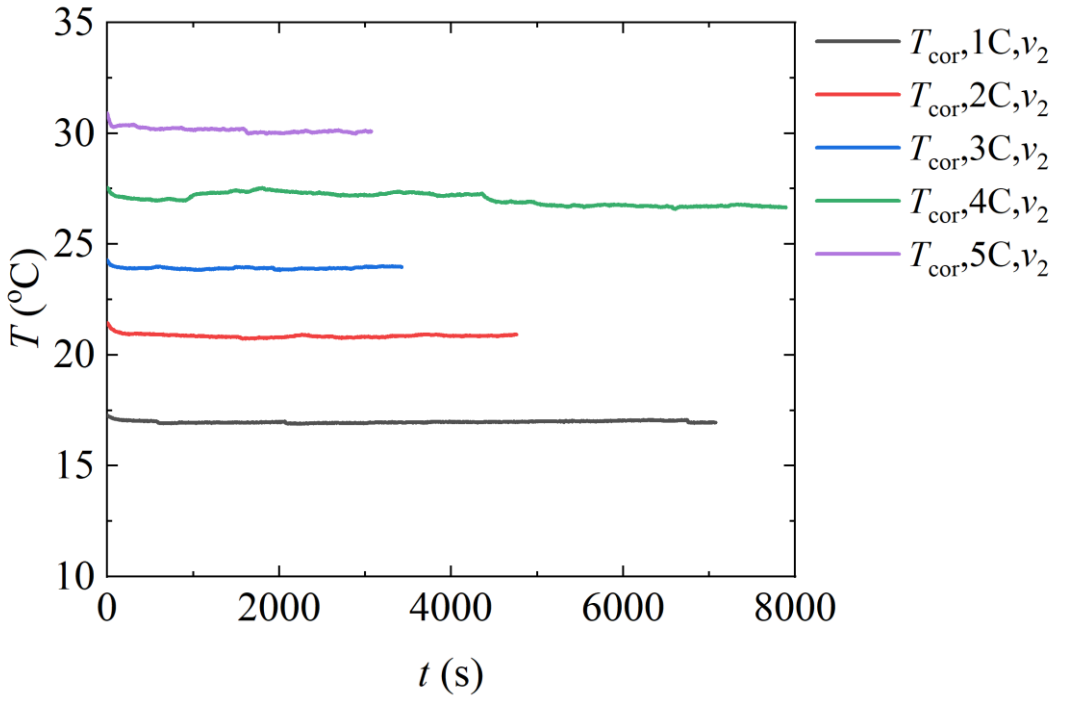

Figure. A3 Core battery temperature of water-cooling BTM with v_2

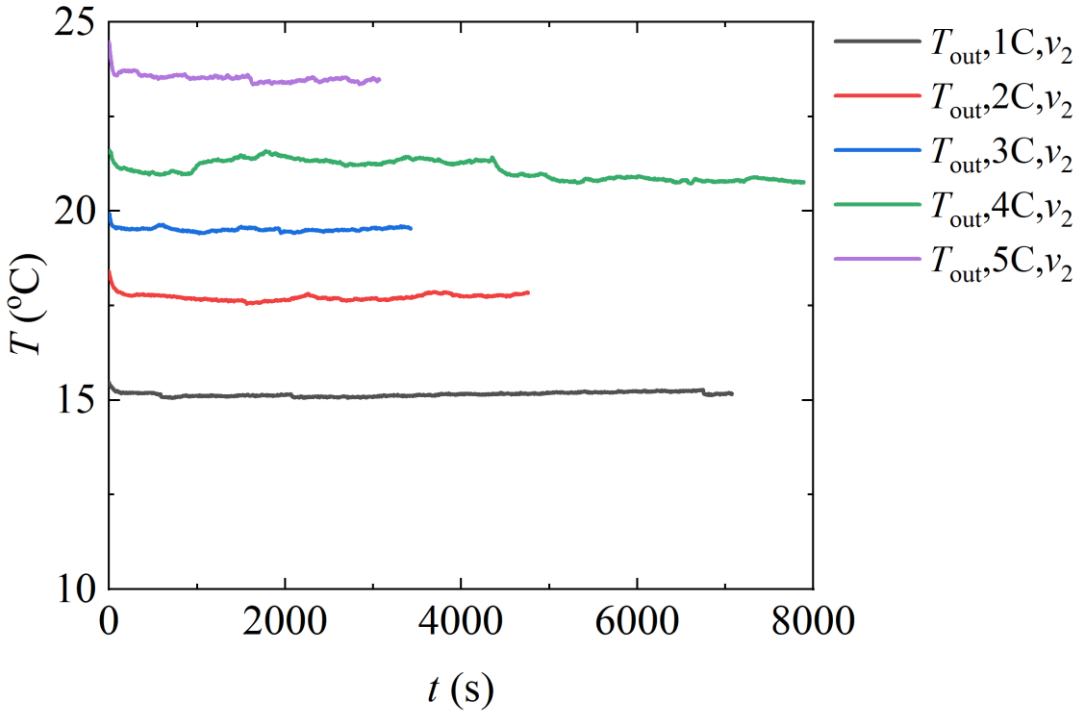

Figure. A4 Outlet water temperature of water-cooling BTM with v_2

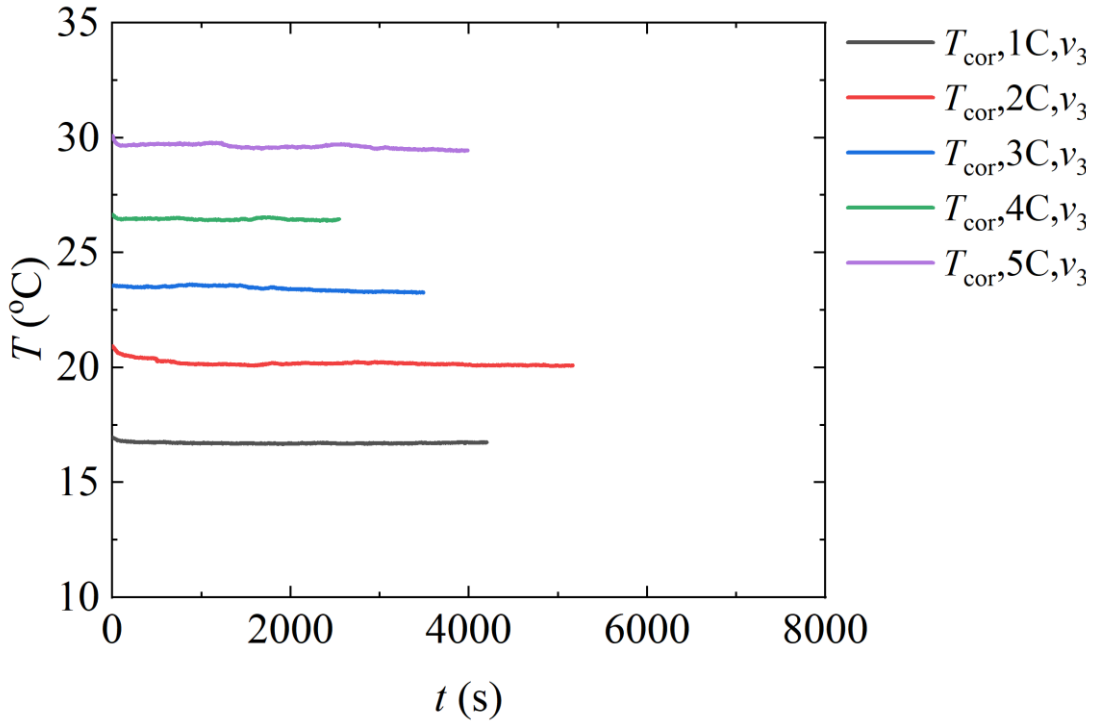

Figure. A5 Core battery temperature of water-cooling BTM with v_3

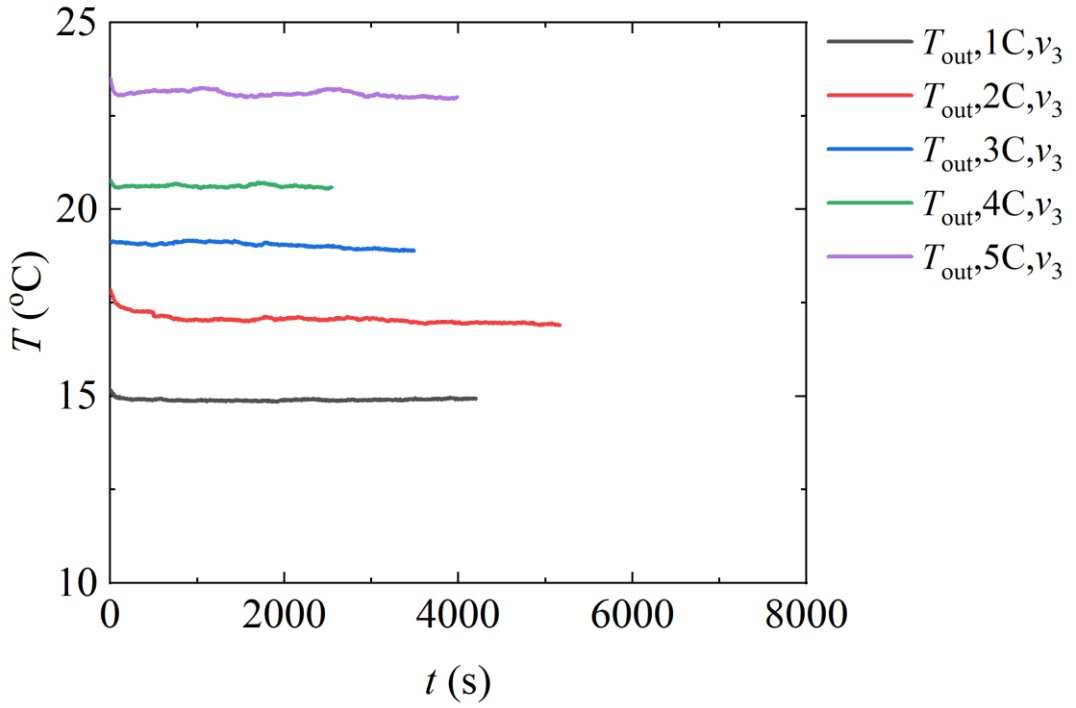

Figure. A6 Outlet water temperature of water-cooling BTM with v_3

Appendix. B T_{cor} and T_{out} with MPCM BTM

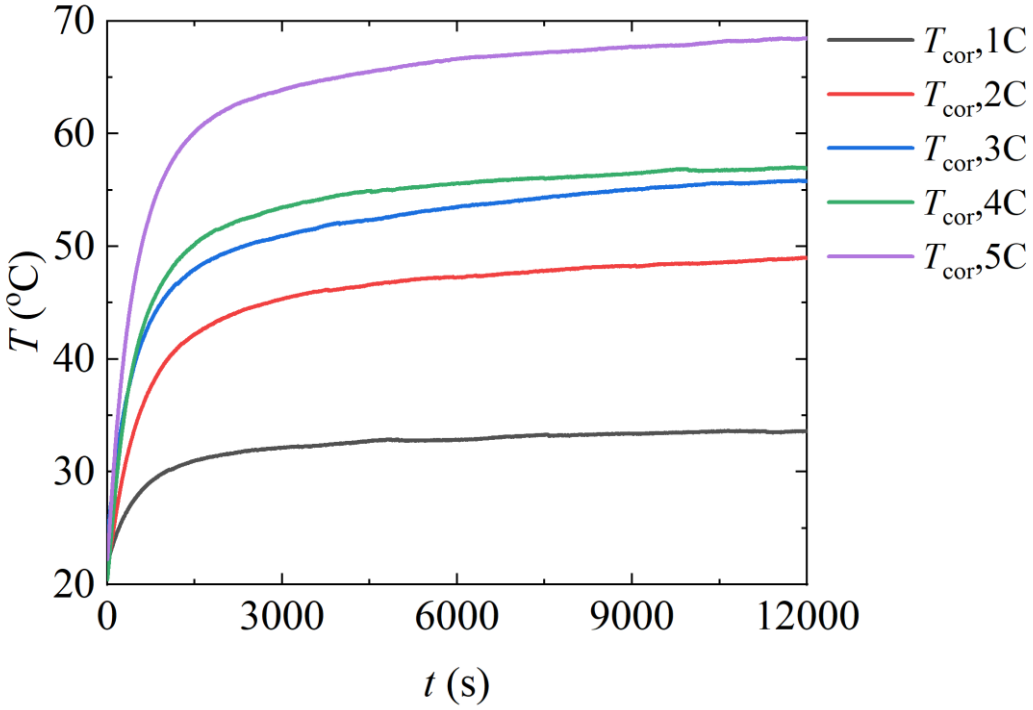

Figure. B1 Outlet water temperature of MPCM BTM with different C-rates

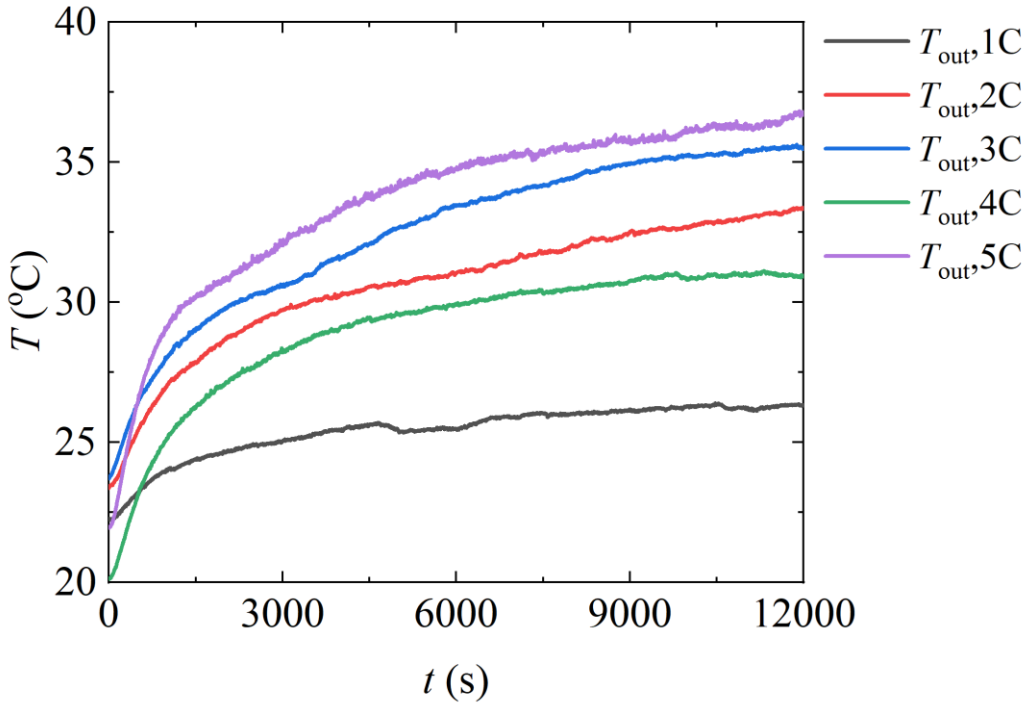

Figure. B2 Outlet slurry temperature of MPCM BTM with different C-rates

Appendix. C Liquid fraction in simulated BTM system

The term of F_1 represents liquid fraction of the PCM source in FSPCM.

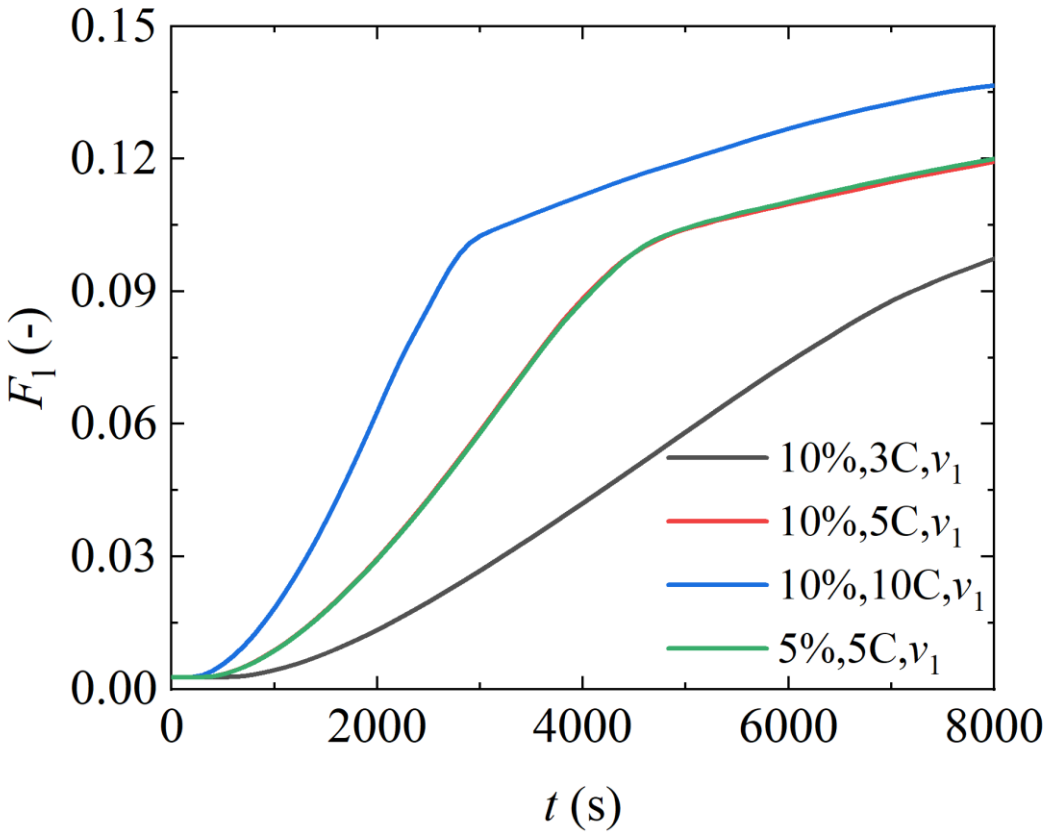

Figure. C1 Liquid fraction of MPCM in FSPCM basement BTM with different C-rate and MPCM mass ratios, using slurry volume flow rate of 0.35 mL/min

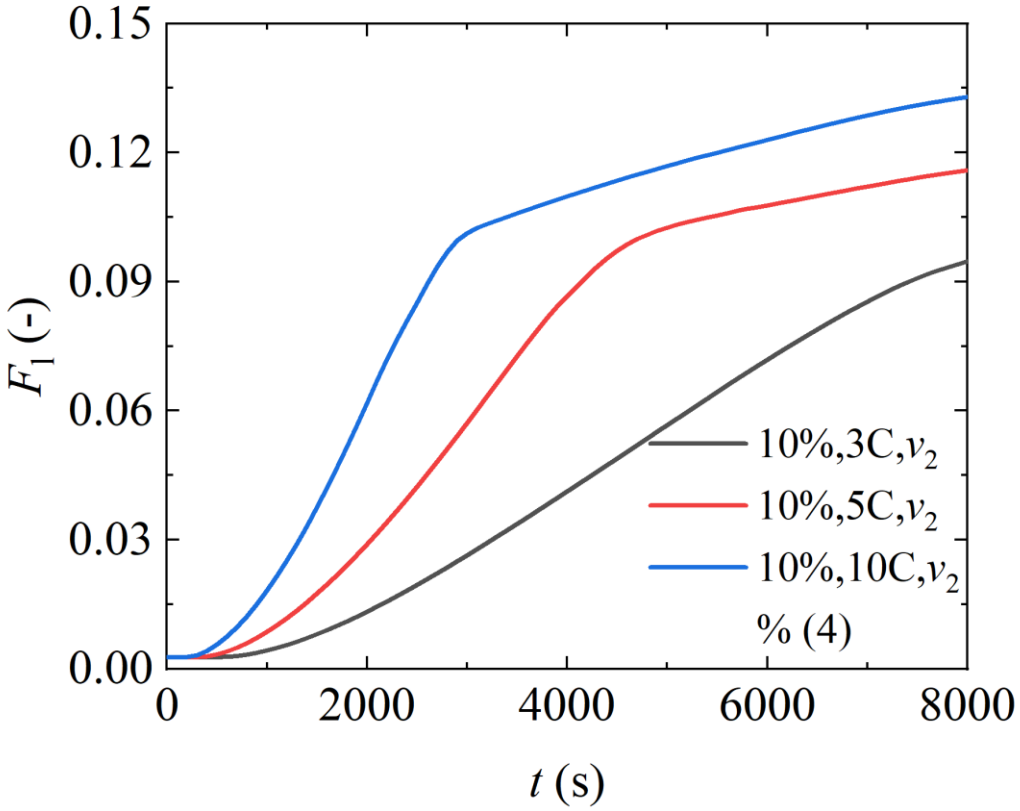

Figure. C2 Liquid fraction of MPCM in FSPCM basement BTM with different C-rate and MPCM mass ratios, using slurry volume flow rate of 0.50 mL/min

Reference

[1] J. Wang, W. Huang, A. Pei, Y. Li, X. Yu, and Y. Cui, "Improving cyclability of Li metal batteries at elevated temperatures and its origin revealed by cryo-electron microscopy," *Nature Energy,* vol. 4, p. 1, 08/01 2019.

[2] P. Ramadass, B. Haran, R. White, and B. N. Popov, "Capacity fade of Sony 18650 cells cycled at elevated temperatures: Part II. Capacity fade analysis," *Journal of Power Sources,* vol. 112, no. 2, pp. 614-620, 2002/11/14/ 2002.

[3] J. R. Selman, S. Al Hallaj, I. Uchida, and Y. Hirano, "Cooperative research on safety fundamentals of lithium batteries," *Journal of Power Sources,* vol. 97-98, pp. 726-732, 2001/07/01/ 2001.

[4] S. A. Khateeb, M. M. Farid, J. R. Selman, and S. Al-Hallaj, "Design and simulation of a lithium-ion battery with a phase change material thermal management system for an electric scooter," *Journal of Power Sources,* vol. 128, no. 2, pp. 292-307, 2004/04/05/ 2004.

[5] I. Uchida, H. Ishikawa, M. Mohamedi, and M. Umeda, "AC-impedance measurements during thermal runaway process in several lithium/polymer batteries," *Journal of Power Sources,* vol. 119-121, pp. 821-825, 2003/06/01/ 2003.

[6] A. Pesaran, M. Keyser, and S. Burch, "An Approach for Designing Thermal Management Systems for Electric and Hybrid Vehicle Battery Packs," presented at the Conference: The Fourth Vehicle Thermal Management Systems Conference and Exhibition, London (GB), 05/24/1999--05/27/1999; Other Information: PBD: 1 Jan 1999; PBD: 1 Jan 1999, United States, 1999. Available: https://www.osti.gov/biblio/3530

https://www.osti.gov/servlets/purl/3530

[7] X. Tang, Q. Guo, M. Li, C. Wei, Z. Pan, and Y. Wang, "Performance analysis on liquid-cooled battery thermal management for electric vehicles based on machine learning," *Journal of Power Sources,* vol. 494, p. 229727, 2021/05/15/ 2021.

[8] A. Verma, S. Shashidhara, and D. Rakshit, "A comparative study on battery thermal management using phase change material (PCM)," *Thermal Science and Engineering Progress,* vol. 11, pp. 74-83, 2019/06/01/ 2019.

[9] X. Y. D. Soo *et al.*, "A highly flexible form-stable silicone-octadecane PCM composite for heat harvesting," *Materials Today Advances,* vol. 14, p. 100227, 2022/06/01/ 2022.

[10] J. Paul *et al.*, "Nano-enhanced organic form stable PCMs for medium temperature solar thermal energy harvesting: Recent progresses, challenges, and opportunities," *Renewable and Sustainable Energy Reviews,* vol. 161, p. 112321, 2022/06/01/ 2022.

[11] A. Yousefi, W. Tang, M. Khavarian, and C. Fang, "Development of novel form-stable phase change material (PCM) composite using recycled expanded glass for thermal energy storage in cementitious composite," *Renewable Energy,* vol. 175, pp. 14-28, 2021/09/01/ 2021.

[12] F. K. Gbekou, K. Benzarti, A. Boudenne, A. Eddhahak, and M. Duc, "Mechanical and thermophysical properties of cement mortars including bio-based microencapsulated phase change materials," *Construction and Building Materials,* vol. 352, p. 129056, 2022/10/17/ 2022.

[13] L. Xu, L. Pu, Z. Angelo, D. Zhang, M. Dai, and S. Zhang, "An experimental investigation on performance of microencapsulated phase change material slurry in ground heat exchanger," *Renewable Energy,* vol. 198, pp. 296-305, 2022/10/01/ 2022.

[14] J. M. Laza *et al.*, "Analysis of the influence of microencapsulated phase change materials on the behavior of a new generation of thermo-regulating shape memory polyurethane fibers," *Polymer Testing,* vol. 116, p. 107807, 2022/12/01/ 2022.

[15] Y. Ji, J. Zhang, S. Li, Y. Deng, and Y. Mu, "Electric vehicles acceptance capacity evaluation in distribution network considering photovoltaics access," *Energy Reports,* vol. 9, pp. 602-608, 2023/03/01/ 2023.

[16] X. Guo, Y. Sun, and D. Ren, "Life cycle carbon emission and cost-effectiveness analysis of electric vehicles in China," *Energy for Sustainable Development,* vol. 72, pp. 1-10, 2023/02/01/ 2023.

[17] M. S. Mastoi *et al.*, "An in-depth analysis of electric vehicle charging station infrastructure, policy implications, and future trends," *Energy Reports,* vol. 8, pp. 11504-11529, 2022/11/01/ 2022.

[18] E. Vinot, R. Trigui, and B. Kabalan, "Rule-based energy management of hybrid electric vehicles focus on load following strategy," in *Encyclopedia of Electrical and Electronic Power Engineering*, J. García, Ed. Oxford: Elsevier, 2023, pp. 529-541.

[19] Z. Liu, S. Liu, T. Zheng, and X. Bao, "Research and verification of energy consumption and E-range of heavy-duty plug-in hybrid electric vehicle," *Energy Reports,* vol. 9, pp. 265-274, 2023/03/01/ 2023.

[20] H. Zhang, S. Liu, N. Lei, Q. Fan, and Z. Wang, "Leveraging the benefits of ethanol-fueled advanced combustion and supervisory control optimization in hybrid biofuel-electric vehicles," *Applied Energy,* vol. 326, p. 120033, 2022/11/15/ 2022.

[21] J. Jung, D.-J. Lee, and K. Yoshida, "Comparison between Korean and Japanese consumers' preferences for fuel cell electric vehicles," *Transportation Research Part D: Transport and Environment,* vol. 113, p. 103511, 2022/12/01/ 2022.

[22] D. Rašić and T. Katrašnik, "Multi-domain and Multi-scale model of a fuel cell electric vehicle to predict the effect of the operating conditions and component sizing on fuel cell degradation," *Energy Conversion and Management,* vol. 268, p. 116024, 2022/09/15/ 2022.

[23] H. Lan, D. Hao, W. Hao, and Y. He, "Development and comparison of the test methods proposed in the Chinese test specifications for fuel cell electric vehicles," *Energy Reports,* vol. 8, pp. 565-579, 2022/07/01/ 2022.

[24] Y. Wu, X. Long, J. Lu, R. Zhou, L. Liu, and Y. Wu, "Long-life in-situ temperature field monitoring using Fiber Bragg grating sensors in electromagnetic launch high-rate hardcase lithium-ion battery," *Journal of Energy Storage,* vol. 57, p. 106207, 2023/01/01/ 2023.

[25] Z. Liu, X. Guo, N. Meng, Z. Yu, and H. Yang, "Study of thermal runaway and the combustion behavior of lithium-ion batteries overcharged with high current rates," *Thermochimica Acta,* vol. 715, p. 179276, 2022/09/01/ 2022.

[26] Y. Wu, X. Long, J. Lu, Y. Wu, R. Zhou, and L. Liu, "Effect of temperature on the high-rate pulse charging of lithium-ion batteries," *Journal of Electroanalytical Chemistry,* vol. 922, p. 116773, 2022/10/01/ 2022.

[27] B. E. White, "Beyond the battery," *Nature Nanotechnology,* vol. 3, no. 2, pp. 71-72, 2008/02/01 2008.

[28] S. Campanari, G. Manzolini, and F. Garcia de la Iglesia, "Energy analysis of electric vehicles using batteries or fuel cells through well-to-wheel driving cycle simulations," *Journal of Power Sources,* vol. 186, no. 2, pp. 464-477, 2009/01/15/ 2009.

[29] C. E. Sandy Thomas, "Transportation options in a carbon-constrained world: Hybrids, plug-in hybrids, biofuels, fuel cell electric vehicles, and battery electric vehicles," *International Journal of Hydrogen Energy,* vol. 34, no. 23, pp. 9279-9296, 2009/12/01/ 2009.

[30] C. Brand, J. Anable, I. Ketsopoulou, and J. Watson, "Road to zero or road to nowhere? Disrupting transport and energy in a zero carbon world," *Energy Policy,* vol. 139, p. 111334, 2020/04/01/ 2020.

[31] Z. Rao and S. Wang, "A review of power battery thermal energy management," *Renewable and Sustainable Energy Reviews,* vol. 15, no. 9, pp. 4554-4571, 2011/12/01/ 2011.

[32] Z. Wang, Y. Jin, M. Wang, and W. Wei, "New fuel consumption standards for Chinese passenger vehicles and their effects on reductions of oil use and CO2 emissions of the Chinese passenger vehicle fleet," *Energy Policy,* vol. 38, no. 9, pp. 5242-5250, 2010/09/01/ 2010.

[33] K. T. Chau, Y. S. Wong, and C. C. Chan, "An overview of energy sources for electric vehicles," *Energy Conversion and Management,* vol. 40, no. 10, pp. 1021-1039, 1999/07/01/ 1999.

[34] "Automakers commit to fuel cell vehicles from 2015," *Fuel Cells Bulletin,* vol. 2009, no. 10, p. 2, 2009/10/01/ 2009.

[35] G. J. Offer, D. Howey, M. Contestabile, R. Clague, and N. P. Brandon, "Comparative analysis of battery electric, hydrogen fuel cell and hybrid vehicles in a future sustainable road transport system," *Energy Policy,* vol. 38, no. 1, pp. 24-29, 2010/01/01/ 2010.

[36] M. A. Delucchi and T. E. Lipman, "An analysis of the retail and lifecycle cost of battery-powered electric vehicles," *Transportation Research Part D: Transport and Environment,* vol. 6, no. 6, pp. 371-404, 2001/11/01/ 2001.

[37] P. T. Moseley and A. Cooper, "Progress towards an advanced lead–acid battery for use in electric vehicles," *Journal of Power Sources,* vol. 78, no. 1, pp. 244-250, 1999/03/01/ 1999.

[38] P. T. Moseley, "Characteristics of a high-performance lead/acid battery for electric vehicles — an ALABC view," *Journal of Power Sources,* vol. 67, no. 1, pp. 115-119, 1997/07/01/ 1997.

[39] S. D. McAllister, S. N. Patankar, I. F. Cheng, and D. B. Edwards, "Lead dioxide coated hollow glass microspheres as conductive additives for lead acid batteries," *Scripta Materialia,* vol. 61, no. 4, pp. 375-378, 2009/08/01/ 2009.

[40] P. Gifford, J. Adams, D. Corrigan, and S. Venkatesan, "Development of advanced nickel/metal hydride batteries for electric and hybrid vehicles," *Journal of Power Sources,* vol. 80, no. 1, pp. 157-163, 1999/07/01/ 1999.

[41] U. Köhler, J. Kümpers, and M. Ullrich, "High performance nickel-metal hydride and lithium-ion batteries," *Journal of Power Sources,* vol. 105, no. 2, pp. 139-144, 2002/03/20/ 2002.

[42] G. Venugopal, "Characterization of thermal cut-off mechanisms in prismatic lithium-ion batteries," *Journal of Power Sources,* vol. 101, no. 2, pp. 231-237, 2001/10/15/ 2001.

[43] N. Terada *et al.*, "Development of lithium batteries for energy storage and EV applications," *Journal of Power Sources,* vol. 100, no. 1, pp. 80-92, 2001/11/30/ 2001.

[44] M. Kise *et al.*, "Development of new safe electrode for lithium rechargeable battery," *Journal of Power Sources,* vol. 146, no. 1, pp. 775-778, 2005/08/26/ 2005.

[45] F. G. Will, "Impact of lithium abundance and cost on electric vehicle battery applications," *Journal of Power Sources,* vol. 63, no. 1, pp. 23-26, 1996/11/01/ 1996.

[46] T. Horiba, K. Hironaka, T. Matsumura, T. Kai, M. Koseki, and Y. Muranaka, "Manganese-based lithium batteries for hybrid electric vehicle applications," *Journal of Power Sources,* vol. 119-121, pp. 893-896, 2003/06/01/ 2003.

[47] K. Kitoh and H. Nemoto, "100 Wh Large size Li-ion batteries and safety tests," *Journal of Power Sources,* vol. 81-82, pp. 887-890, 1999/09/01/ 1999.

[48] Y. Nishi, "Lithium ion secondary batteries; past 10 years and the future," *Journal of Power Sources,* vol. 100, no. 1, pp. 101-106, 2001/11/30/ 2001.

[49] D. H. Johnson, "Design of a safe cylindrical lithium/thionyl chloride cell," in *The 1982 Goddard Space Flight Center Battery Workshop*, 1983, pp. 75-84.

[50] K. Tamura and T. Horiba, "Large-scale development of lithium batteries for electric vehicles and electric power storage applications," *Journal of Power Sources,* vol. 81-82, pp. 156-161, 1999/09/01/ 1999.

[51] K. Onda, T. Ohshima, M. Nakayama, K. Fukuda, and T. Araki, "Thermal behavior of small lithium-ion battery during rapid charge and discharge cycles," *Journal of Power Sources,* vol. 158, no. 1, pp. 535-542, 2006/07/14/ 2006.

[52] J. X. Weinert, A. F. Burke, and X. Wei, "Lead-acid and lithium-ion batteries for the Chinese electric bike market and implications on future technology advancement," *Journal of Power Sources,* vol. 172, no. 2, pp. 938-945, 2007/10/25/ 2007.

[53] D. D. MacNeil and J. R. Dahn, "The Reaction of Charged Cathodes with Nonaqueous Solvents and Electrolytes: I. Li0.5CoO2," *Journal of The Electrochemical Society,* vol. 148, no. 11, p. A1205, 2001/09/20 2001.

[54] D. D. MacNeil and J. R. Dahn, "The Reaction of Charged Cathodes with Nonaqueous Solvents and Electrolytes: II. LiMn2 O 4 charged to 4.2 V," *Journal of The Electrochemical Society,* vol. 148, no. 11, p. A1211, 2001/09/20 2001.

[55] R. Venkatachalapathy, C. W. Lee, W. Lu, and J. Prakash, "Thermal investigations of transitional metal oxide cathodes in Li-ion cells," *Electrochemistry Communications,* vol. 2, no. 2, pp. 104-107, 2000/02/01/ 2000.

[56] A. Pesaran, A. Vlahinos, and T. Stuart, "Cooling and preheating of batteries in hybrid electric vehicles," in *6th ASME-JSME Thermal Engineering Joint Conference*, 2003, pp. 1-7: Citeseer.

[57] P. Biensan *et al.*, "On safety of lithium-ion cells," *Journal of Power Sources,* vol. 81-82, pp. 906-912, 1999/09/01/ 1999.

[58] M. N. Richard and J. R. Dahn, "Predicting electrical and thermal abuse behaviours of practical lithium-ion cells from accelerating rate calorimeter studies on small samples in electrolyte," *Journal of Power Sources,* vol. 79, no. 2, pp. 135-142, 1999/06/01/ 1999.

[59] U. von Sacken, E. Nodwell, A. Sundher, and J. R. Dahn, "Comparative thermal stability of carbon intercalation anodes and lithium metal anodes for rechargeable lithium batteries," *Journal of Power Sources,* vol. 54, no. 2, pp. 240-245, 1995/04/01/ 1995.

[60] H. Maleki, G. Deng, A. Anani, and J. Howard, "Thermal Stability Studies of Li-Ion Cells and Components," *Journal of The Electrochemical Society,* vol. 146, no. 9, p. 3224, 1999/09/01 1999.

[61] Z. Zhang, D. Fouchard, and J. R. Rea, "Differential scanning calorimetry material studies: implications for the safety of lithium-ion cells," *Journal of Power Sources,* vol. 70, no. 1, pp. 16-20, 1998/01/30/ 1998.

[62] R. A. Leising, M. J. Palazzo, E. S. Takeuchi, and K. J. Takeuchi, "A study of the overcharge reaction of lithium-ion batteries," *Journal of Power Sources,* vol. 97-98, pp. 681-683, 2001/07/01/ 2001.

[63] R. Sabbah, R. Kizilel, J. R. Selman, and S. Al-Hallaj, "Active (air-cooled) vs. passive (phase change material) thermal management of high power lithium-ion packs: Limitation of temperature rise and uniformity of temperature distribution," *Journal of Power Sources,* vol. 182, no. 2, pp. 630-638, 2008/08/01/ 2008.

[64] S. C. Nagpure, R. Dinwiddie, S. S. Babu, G. Rizzoni, B. Bhushan, and T. Frech, "Thermal diffusivity study of aged Li-ion batteries using flash method," *Journal of Power Sources,* vol. 195, no. 3, pp. 872-876, 2010/02/01/ 2010.

[65] A. A. Pesaran, "Battery thermal models for hybrid vehicle simulations," *Journal of Power Sources,* vol. 110, no. 2, pp. 377-382, 2002/08/22/ 2002.

[66] N. Sato, "Thermal behavior analysis of lithium-ion batteries for electric and hybrid vehicles," *Journal of Power Sources,* vol. 99, no. 1, pp. 70-77, 2001/08/01/ 2001.

[67] B. L. McKinney, G. L. Wierschem, and E. N. J. S. T. Mrotek, "Thermal management of lead-acid batteries for electric vehicles," pp. 839-845, 1983.

[68] H. Giess, "Investigation of thermal phenomena in VRLA/AGM stationary lead/acid batteries with a thermal video imaging system," *Journal of Power Sources,* vol. 67, no. 1, pp. 49-59, 1997/07/01/ 1997.

[69] A. Jossen, V. Späth, H. Döring, and J. Garche, "Reliable battery operation — a challenge for the battery management system," *Journal of Power Sources,* vol. 84, no. 2, pp. 283-286, 1999/12/01/ 1999.

[70] R. Kizilel, R. Sabbah, J. R. Selman, and S. Al-Hallaj, "An alternative cooling system to enhance the safety of Li-ion battery packs," *Journal of Power Sources,* vol. 194, no. 2, pp. 1105-1112, 2009/12/01/ 2009.

[71] M. A. Abdelkareem *et al.*, "Thermal management systems based on heat pipes for batteries in EVs/HEVs," *Journal of Energy Storage,* vol. 51, p. 104384, 2022/07/01/ 2022.

[72] X. Zhang, Z. Li, L. Luo, Y. Fan, and Z. Du, "A review on thermal management of lithium-ion batteries for electric vehicles," *Energy,* vol. 238, p. 121652, 2022/01/01/ 2022.

[73] M. Subramanian *et al.*, "A technical review on composite phase change material based secondary assisted battery thermal management system for electric vehicles," *Journal of Cleaner Production,* vol. 322, p. 129079, 2021/11/01/ 2021.

[74] S. Al-Hallaj and J. R. Selman, "Thermal modeling of secondary lithium batteries for electric vehicle/hybrid electric vehicle applications," *Journal of Power Sources,* vol. 110, no. 2, pp. 341-348, 2002/08/22/ 2002.

[75] D. Y. Jung, B. H. Lee, and S. W. Kim, "Development of battery management system for nickel–metal hydride batteries in electric vehicle applications," *Journal of Power Sources,* vol. 109, no. 1, pp. 1-10, 2002/06/15/ 2002.

[76] M. Zolot, A. A. Pesaran, and M. J. S. t. p. Mihalic, "Thermal evaluation of Toyota Prius battery pack," pp. 01-1962, 2002.

[77] L. Y, "Nickel-metal hydride battery cooling system research for hybrid electric vehicle," *Shanghai: Shanghai Jiao Tong University [in Chinese],* 2007.

[78] P. Nelson, D. Dees, K. Amine, and G. Henriksen, "Modeling thermal management of lithium-ion PNGV batteries," *Journal of Power Sources,* vol. 110, no. 2, pp. 349-356, 2002/08/22/ 2002.

[79] M.-S. Wu, K. H. Liu, Y.-Y. Wang, and C.-C. Wan, "Heat dissipation design for lithium-ion batteries," *Journal of Power Sources,* vol. 109, no. 1, pp. 160-166, 2002/06/15/ 2002.

[80] A. N. Jansen, D. W. Dees, D. P. Abraham, K. Amine, and G. L. Henriksen, "Low-temperature study of lithium-ion cells using a LiySn micro-reference electrode," *Journal of Power Sources,* vol. 174, no. 2, pp. 373-379, 2007/12/06/ 2007.

[81] Y. Chen and J. W. Evans, "Heat Transfer Phenomena in Lithium/Polymer-Electrolyte Batteries for Electric Vehicle Application," *Journal of The Electrochemical Society,* vol. 140, no. 7, p. 1833, 1993/07/01 1993.

[82] A. A. J. B. M. Pesaran, "Battery thermal management in EV and HEVs: issues and solutions," vol. 43, no. 5, pp. 34-49, 2001.

[83] D. R. Pendergast, E. P. DeMauro, M. Fletcher, E. Stimson, and J. C. Mollendorf, "A rechargeable lithium-ion battery module for underwater use," *Journal of Power Sources,* vol. 196, no. 2, pp. 793-800, 2011/01/15/ 2011.

[84] J.-C. Jang and S.-H. Rhi, "Battery thermal management system of future electric vehicles with loop thermosyphon," in *US-Korea conference on science, technology, and entrepreneurship (UKC)*, 2010.

[85] G. Swanepoel, "Thermal management of hybrid electrical vehicles using heat pipes," Stellenbosch: Stellenbosch University, 2001.

[86] S. A. Hallaj and J. R. Selman, "A Novel Thermal Management System for Electric Vehicle Batteries Using Phase-Change Material," *Journal of The Electrochemical Society,* vol. 147, no. 9, p. 3231, 2000/09/01 2000.

[87] A. Mills and S. Al-Hallaj, "Simulation of passive thermal management system for lithium-ion battery packs," *Journal of Power Sources,* vol. 141, no. 2, pp. 307-315, 2005/03/01/ 2005.

[88] S. A. Khateeb, S. Amiruddin, M. Farid, J. R. Selman, and S. Al-Hallaj, "Thermal management of Li-ion battery with phase change material for electric scooters: experimental validation," *Journal of Power Sources,* vol. 142, no. 1, pp. 345-353, 2005/03/24/ 2005.

[89] R. Kizilel, A. Lateef, R. Sabbah, M. M. Farid, J. R. Selman, and S. Al-Hallaj, "Passive control of temperature excursion and uniformity in high-energy Li-ion battery packs at high current and ambient temperature," *Journal of Power Sources,* vol. 183, no. 1, pp. 370-375, 2008/08/15/ 2008.

[90] Z. Rao, G. J. E. S. Zhang, Part A: Recovery, Utilization,, and E. Effects, "Thermal properties of paraffin wax-based composites containing graphite," vol. 33, no. 7, pp. 587-593, 2011.

[91] M. R. Cosley and M. P. Garcia, "Battery thermal management system," in *INTELEC 2004. 26th Annual International Telecommunications Energy Conference*, 2004, pp. 38-45.

[92] S. Yu and D. Jung, "Thermal management strategy for a proton exchange membrane fuel cell system with a large active cell area," *Renewable Energy,* vol. 33, no. 12, pp. 2540-2548, 2008/12/01/ 2008.

[93] A. Faghri and Z. Guo, "Challenges and opportunities of thermal management issues related to fuel cell technology and modeling," *International Journal of Heat and Mass Transfer,* vol. 48, no. 19, pp. 3891-3920, 2005/09/01/ 2005.

[94] Y. Huang, X. Xiao, H. Kang, J. Lv, R. Zeng, and J. Shen, "Thermal management of polymer electrolyte membrane fuel cells: A critical review of heat transfer mechanisms, cooling approaches, and advanced cooling techniques analysis," *Energy Conversion and Management,* vol. 254, p. 115221, 2022/02/15/ 2022.

[95] J. Xu, C. Zhang, Z. Wan, X. Chen, S. H. Chan, and Z. Tu, "Progress and perspectives of integrated thermal management systems in PEM fuel cell vehicles: A review," *Renewable and Sustainable Energy Reviews,* vol. 155, p. 111908, 2022/03/01/ 2022.

[96] L. Matamoros and D. Brüggemann, "Simulation of the water and heat management in proton exchange membrane fuel cells," *Journal of Power Sources,* vol. 161, no. 1, pp. 203-213, 2006/10/20/ 2006.

[97] L. Dumercy, R. Glises, H. Louahlia-Gualous, and J. M. Kauffmann, "Thermal management of a PEMFC stack by 3D nodal modeling," *Journal of Power Sources,* vol. 156, no. 1, pp. 78-84, 2006/05/19/ 2006.

[98] C. Bao, M. Ouyang, and B. Yi, "Analysis of the water and thermal management in proton exchange membrane fuel cell systems," *International Journal of Hydrogen Energy,* vol. 31, no. 8, pp. 1040-1057, 2006/07/01/ 2006.

[99] Y. Zong, B. Zhou, and A. Sobiesiak, "Water and thermal management in a single PEM fuel cell with non-uniform stack temperature," *Journal of Power Sources,* vol. 161, no. 1, pp. 143-159, 2006/10/20/ 2006.

[100] D. H. Ahmed, H. J. Sung, and J. Bae, "Effect of GDL permeability on water and thermal management in PEMFCs—I. Isotropic and anisotropic permeability," *International Journal of Hydrogen Energy,* vol. 33, no. 14, pp. 3767-3785, 2008/07/01/ 2008.

[101] F. Agyenim, N. Hewitt, P. Eames, and M. Smyth, "A review of materials, heat transfer and phase change problem formulation for latent heat thermal energy storage systems (LHTESS)," *Renewable and Sustainable Energy Reviews,* vol. 14, no. 2, pp. 615-628, 2010/02/01/ 2010.

[102] A. Sharma, V. V. Tyagi, C. R. Chen, and D. Buddhi, "Review on thermal energy storage with phase change materials and applications," *Renewable and Sustainable Energy Reviews,* vol. 13, no. 2, pp. 318-345, 2009/02/01/ 2009.

[103] L. M. Bal, S. Satya, and S. N. Naik, "Solar dryer with thermal energy storage systems for drying agricultural food products: A review," *Renewable and Sustainable Energy Reviews,* vol. 14, no. 8, pp. 2298-2314, 2010/10/01/ 2010.

[104] Y. Dutil, D. R. Rousse, N. B. Salah, S. Lassue, and L. Zalewski, "A review on phase-change materials: Mathematical modeling and simulations," *Renewable and Sustainable Energy Reviews,* vol. 15, no. 1, pp. 112-130, 2011/01/01/ 2011.

[105] S. Jegadheeswaran and S. D. Pohekar, "Performance enhancement in latent heat thermal storage system: A review," *Renewable and Sustainable Energy Reviews,* vol. 13, no. 9, pp. 2225-2244, 2009/12/01/ 2009.

[106] M. M. Kenisarin, "High-temperature phase change materials for thermal energy storage," *Renewable and Sustainable Energy Reviews,* vol. 14, no. 3, pp. 955-970, 2010/04/01/ 2010.

[107] R. Kandasamy, X.-Q. Wang, and A. S. Mujumdar, "Application of phase change materials in thermal management of electronics," *Applied Thermal Engineering,* vol. 27, no. 17, pp. 2822-2832, 2007/12/01/ 2007.

[108] A. Mills, M. Farid, J. R. Selman, and S. Al-Hallaj, "Thermal conductivity enhancement of phase change materials using a graphite matrix," *Applied Thermal Engineering,* vol. 26, no. 14, pp. 1652-1661, 2006/10/01/ 2006.

[109] A. Alrashdan, A. T. Mayyas, and S. Al-Hallaj, "Thermo-mechanical behaviors of the expanded graphite-phase change material matrix used for thermal management of Li-ion battery packs," *Journal of Materials Processing Technology,* vol. 210, no. 1, pp. 174-179, 2010/01/01/ 2010.

[110] Y. Cai, L. Song, Q. He, D. Yang, and Y. Hu, "Preparation, thermal and flammability properties of a novel form-stable phase change materials based on high density polyethylene/poly(ethylene-co-vinyl acetate)/organophilic montmorillonite nanocomposites/paraffin compounds," *Energy Conversion and Management,* vol. 49, no. 8, pp. 2055-2062, 2008/08/01/ 2008.

[111] X. Zhou, H. Xiao, J. Feng, C. Zhang, and Y. Jiang, "Preparation and thermal properties of paraffin/porous silica ceramic composite," *Composites Science and Technology,* vol. 69, no. 7, pp. 1246-1249, 2009/06/01/ 2009.

[112] C. J. Ho and J. Y. Gao, "Preparation and thermophysical properties of nanoparticle-in-paraffin emulsion as phase change material," *International Communications in Heat and Mass Transfer,* vol. 36, no. 5, pp. 467-470, 2009/05/01/ 2009.

[113] E.-B. S. Mettawee and G. M. R. Assassa, "Thermal conductivity enhancement in a latent heat storage system," *Solar Energy,* vol. 81, no. 7, pp. 839-845, 2007/07/01/ 2007.

[114] P. Zhang, Y. Hu, L. Song, J. Ni, W. Xing, and J. Wang, "Effect of expanded graphite on properties of high-density polyethylene/paraffin composite with intumescent flame retardant as a shape-stabilized phase change material," *Solar Energy Materials and Solar Cells,* vol. 94, no. 2, pp. 360-365, 2010/02/01/ 2010.

[115] Y. Cai, Q. Wei, F. Huang, S. Lin, F. Chen, and W. Gao, "Thermal stability, latent heat and flame retardant properties of the thermal energy storage phase change materials based on paraffin/high density polyethylene composites," *Renewable Energy,* vol. 34, no. 10, pp. 2117-2123, 2009/10/01/ 2009.

[116] W. Wu, W. Wu, and S. Wang, "Form-stable and thermally induced flexible composite phase change material for thermal energy storage and thermal management applications," *Applied Energy,* vol. 236, pp. 10-21, 2019/02/15/ 2019.

[117] C. Chen, X. Liu, W. Liu, and M. Ma, "A comparative study of myristic acid/bentonite and myristic acid/Eudragit L100 form stable phase change materials for thermal energy storage," *Solar Energy Materials and Solar Cells,* vol. 127, pp. 14-20, 2014/08/01/ 2014.

[118] K. Wei *et al.*, "Preparation of polyurethane solid-solid low temperature PCMs granular asphalt mixes and study of phase change temperature control behavior," *Solar Energy,* vol. 231, pp. 149-157, 2022/01/01/ 2022.

[119] C. Alkan, K. Kaya, and A. Sarı, "Preparation, Thermal Properties and Thermal Reliability of Form-Stable Paraffin/Polypropylene Composite for Thermal Energy Storage," *Journal of Polymers and the Environment,* vol. 17, no. 4, p. 254, 2009/10/07 2009.

[120] A. Karaipekli, A. Biçer, A. Sarı, and V. V. Tyagi, "Thermal characteristics of expanded perlite/paraffin composite phase change material with enhanced thermal conductivity using carbon nanotubes," *Energy Conversion and Management,* vol. 134, pp. 373-381, 2017/02/15/ 2017.

[121] P. Zhang, Y. Cui, K. Zhang, S. Wu, D. Chen, and Y. Gao, "Enhanced thermal storage capacity of paraffin/diatomite composite using oleophobic modification," *Journal of Cleaner Production,* vol. 279, p. 123211, 2021/01/10/ 2021.

[122] Y. Qu, S. Wang, Y. Tian, and D. Zhou, "Comprehensive evaluation of Paraffin-HDPE shape stabilized PCM with hybrid carbon nano-additives," *Applied Thermal Engineering,* vol. 163, p. 114404, 2019/12/25/ 2019.

[123] P. Sobolciak, M. Karkri, M. A. Al-Maadeed, and I. Krupa, "Thermal characterization of phase change materials based on linear low-density polyethylene, paraffin wax and expanded graphite," *Renewable Energy,* vol. 88, pp. 372-382, 2016/04/01/ 2016.

[124] R. Taherian, "7 - Application of Polymer-Based Composites: Bipolar Plate of PEM Fuel Cells," in *Electrical Conductivity in Polymer-Based Composites*, R. Taherian and A. Kausar, Eds.: William Andrew Publishing, 2019, pp. 183-237.

[125] W.-l. Cheng, R.-m. Zhang, K. Xie, N. Liu, and J. Wang, "Heat conduction enhanced shape-stabilized paraffin/HDPE composite PCMs by graphite addition: Preparation and thermal properties," *Solar Energy Materials and Solar Cells,* vol. 94, no. 10, pp. 1636-1642, 2010/10/01/ 2010.

[126] R. Simón-Allué, I. Guedea, R. Villén, and G. Brun, "Experimental study of Phase Change Material influence on different models of Photovoltaic-Thermal collectors," *Solar Energy,* vol. 190, pp. 1-9, 2019/09/15/ 2019.

[127] P. B. Salunkhe and P. S. Shembekar, "A review on effect of phase change material encapsulation on the thermal performance of a system," *Renewable and Sustainable Energy Reviews,* vol. 16, no. 8, pp. 5603-5616, 2012/10/01/ 2012.

[128] M. Modjinou *et al.*, "Performance comparison of encapsulated PCM PV/T, microchannel heat pipe PV/T and conventional PV/T systems," *Energy,* vol. 166, pp. 1249-1266, 2019/01/01/ 2019.

[129] H. Fayaz, N. A. Rahim, M. Hasanuzzaman, A. Rivai, and R. Nasrin, "Numerical and outdoor real time experimental investigation of performance of PCM based PVT system," *Solar Energy,* vol. 179, pp. 135-150, 2019/02/01/ 2019.

[130] Y. Su, Y. Zhang, and L. Shu, "Experimental study of using phase change material cooling in a solar tracking concentrated photovoltaic-thermal system," *Solar Energy,* vol. 159, pp. 777-785, 2018/01/01/ 2018.

[131] H. Peng *et al.*, "n-Alkanes Phase Change Materials and Their Microencapsulation for Thermal Energy Storage: A Critical Review," *Energy & Fuels,* vol. 32, no. 7, pp. 7262-7293, 2018/07/19 2018.

[132] Y. Zhang *et al.*, "Hydrocolloids: Nova materials assisting encapsulation of volatile phase change materials for cryogenic energy transport and storage," *Chemical Engineering Journal,* vol. 382, p. 123028, 2020/02/15/ 2020.

[133] Q. Yu, A. Romagnoli, B. Al-Duri, D. Xie, Y. Ding, and Y. Li, "Heat storage performance analysis and parameter design for encapsulated phase change materials," *Energy Conversion and Management,* vol. 157, pp. 619-630, 2018/02/01/ 2018.

[134] Q. Yu, F. Tchuenbou-Magaia, B. Al-Duri, Z. Zhang, Y. Ding, and Y. Li, "Thermo-mechanical analysis of microcapsules containing phase change materials for cold storage," *Applied Energy,* vol. 211, pp. 1190-1202, 2018/02/01/ 2018.

[135] Q. Yu, X. Chen, and H. Yang, "Research progress on utilization of phase change materials in photovoltaic/thermal systems: A critical review," *Renewable and Sustainable Energy Reviews,* vol. 149, p. 111313, 2021/10/01/ 2021.

[136] M. Delgado, A. Lázaro, J. Mazo, and B. Zalba, "Review on phase change material emulsions and microencapsulated phase change material slurries: Materials, heat transfer studies and applications," *Renewable and Sustainable Energy Reviews,* vol. 16, no. 1, pp. 253-273, 2012/01/01/ 2012.

[137] Y. Zhang, S. Wang, Z. Rao, and J. Xie, "Experiment on heat storage characteristic of microencapsulated phase change material slurry," *Solar Energy Materials and Solar Cells,* vol. 95, no. 10, pp. 2726-2733, 2011/10/01/ 2011.

[138] M. Delgado, A. Lázaro, J. Mazo, J. M. Marín, and B. Zalba, "Experimental analysis of a microencapsulated PCM slurry as thermal storage system and as heat transfer fluid in laminar flow," *Applied Thermal Engineering,* vol. 36, pp. 370-377, 2012/04/01/ 2012.

[139] Y. Yoon *et al.*, "A Strategy for Synthesis of Carbon Nitride Induced Chemically Doped 2D MXene for High-Performance Supercapacitor Electrodes," (in English), *Advanced Energy Materials,* Article vol. 8, no. 15, p. 11, May 2018, Art. no. 1703173.

[140] Z. W. Ma and P. Zhang, "Modeling the heat transfer characteristics of flow melting of phase change material slurries in the circular tubes," *International Journal of Heat and Mass Transfer,* vol. 64, pp. 874-881, 2013/09/01/ 2013.

[141] J. Maxwell, "A treatise on electricity and magnetism. With prefaces by WD Niven and JJ Thomson. Reprint of the third (1891) edition," ed: Dover Publications, Inc., New York, N. Y, 1954.

[142] A. Eucken, "Allgemeine Gesetzmäßigkeiten für das Wärmeleitvermögen verschiedener Stoffarten und Aggregatzustände," *Forschung auf dem Gebiet des Ingenieurwesens A,* vol. 11, no. 1, pp. 6-20, 1940/01/01 1940.

[143] W. Wu, W. Wu, and S. Wang, "Thermal management optimization of a prismatic battery with shape-stabilized phase change material," *International Journal of Heat and Mass Transfer,* vol. 121, pp. 967-977, 2018/06/01/ 2018.

[144] P. Kosky, R. Balmer, W. Keat, and G. Wise, "Chapter 14 - Mechanical Engineering," in *Exploring Engineering (Fifth Edition)*, P. Kosky, R. Balmer, W. Keat, and G. Wise, Eds.: Academic Press, 2021, pp. 317-340.

[145] T. L. Bergman, T. L. Bergman, F. P. Incropera, D. P. DeWitt, and A. S. Lavine, *Fundamentals of Heat and Mass Transfer*. Wiley, 2011.

[146] M. Bahrami, "Forced Convection Heat Transfer. https://www.sfu.ca/~mbahrami/ENSC%20388/Notes/Forced%20Convection.pdf."

[147] D. Bernardi, E. Pawlikowski, and J. Newman, "A General Energy Balance for Battery Systems," *Journal of The Electrochemical Society,* vol. 132, no. 1, pp. 5-12, 1985/01/01 1985.

[148] i. Microtek Laboraories, "Product data sheets of MPCM 32D."

[149] Z. W. Ma, P. Zhang, R. Z. Wang, S. Furui, and G. N. Xi, "Forced flow and convective melting heat transfer of clathrate hydrate slurry in tubes," *International Journal of Heat and Mass Transfer,* vol. 53, no. 19, pp. 3745-3757, 2010/09/01/ 2010.

[150] P. Zhang, Z. W. Ma, Z. Y. Bai, and J. Ye, "Rheological and energy transport characteristics of a phase change material slurry," *Energy,* vol. 106, pp. 63-72, 2016/07/01/ 2016.

[151] A. Lococo, "Nissan Leaf Battery Design and Maintenance."

[152] R. C. Ltd, "RS PRO Datasheet of RS PRO flow meter, 0.05 – 10 L/min."

[153] R. C. Ltd, "RS Datasheet of RS PRO Direct Coupling Centrifugal Water Pump, 1150ml/min."

[154] O. Engineering, "OMEGA Datasheet of Omega pressure transmitter PX2300-2DI."

[155] A. Fluent, "ANSYS FLUENT 14.5 Theory Guide," 2012.

[156] D. M. Weragoda, G. Tian, A. Burkitbayev, K.-H. Lo, and T. Zhang, "A comprehensive review on heat pipe based battery thermal management systems," *Applied Thermal Engineering,* vol. 224, p. 120070, 2023/04/01/ 2023.